Physics-based Modelling, Simulation, Placement and Learning for Musculo-Skeletal Animations

Fabio Turchet

A thesis submitted in partial fulfillment of the requirements of Bournemouth University for the degree of Doctor of Engineering

Supervisors: Dr Oleg Fryazinov,
Dr Sara Schvartzman

January, 2018

Copyright statement

Contents

List of Figures

List of Tables

Abstract

In character production for Visual Effects, the realism of deformations and flesh dynamics is a vital ingredient of the final rendered moving images shown on screen. This work is a collection of projects completed at the hosting company MPC London focused on the main components needed for the animation of musculo-skeletal systems: primitives modeling, physically accurate simulation, interactive placement. Complementary projects are also presented, including the procedural modeling of wrinkles and a machine learning approach for deformable objects based on Deep Neural Networks. Primitives modeling aims at proposing an approach to generating muscle geometry complete with tendons and fibers from superficial patches sketched on the character skin mesh. The method utilizes the physics of inflatable surfaces and produces meshes ready to be tetrahedralized, that is without compenetrations. A framework for the simulation of muscles, fascia and fat tissues based on the Finite Elements Method (FEM) is presented, together with the theoretical foundations of fiber-based materials with activations and their fitting in the Implicit Euler integration. The FEM solver is then simplified in order to achieve interactive rates to show the potential of interactive muscle placement on the skeleton to facilitate the creation of intersection-free primitives using collision detection and resolution. Alongside physics simulation for biological tissues, the thesis explores an approach that extends the Implicit Skinning technique with wrinkles based on convolution surfaces by exploiting the gradients of the combination of bones fields. Finally, this work discusses a possible approach to the learning of physics-based deformable objects based on deep neural networks which makes use of geodesic disks convolutional layers.

Acknowledgements

I would like to express my most sincere gratitude to the CDE and my supervisors: Dr Oleg Fryazinov, Dr Sara Schvartzman and Dr Marco Romeo. Without their encouragement, invaluable support and patience none of this work would have been possible: I know there were moments you wanted to kill me, but I'm glad I'm still alive.
Special thanks to the great people at MPC and Technicolor: the management team, in particular Georg, Rob and Hannes for believing in my brain potential and in the benefits of long-term research; all the talented colleagues in the Software and Rigging departments for the feedback and the many joyful after-work drinking times: some of you are truly good friends; Jamie Portsmouth for his great help with formulas derivations; Vlad for the good laughs, discussions and for forcing me many times to unglue myself from the chair and take some fresh air out.
Very special thanks to NVIDIA corporation for the donation of a Titan Xp card as part of their GPU grant program.
I also wish to express my sincere appreciation to all the great teachers and researchers I met in these four years at conferences around the world: I am grateful for all the passion you put in your work, for being visionaries, for demonstrating that often *impossible* is just a word and for releasing extremely useful open source material for education purposes.
I would like to thank here my dearest friends who enriched so much my life while staying in London: Pedro and Federico for being fantastic humans and for always being there in the good and bad times; the Portuguese crew for all the parties; Lucie, Ania and Nia for reminding me to believe in my dreams and that Life is truly beautiful; my flatmates in London for always giving me a smile when I came back home very late and never made me feel I was just a crazy scientist.
Last but not least, I would like to address my biggest and warmest acknowledgement to my family: my parents for constantly and unconditionally supporting me with their love in every possible way during these roller-coaster years; my aunt Antonietta for the best inspirational quotes and finally my brother Luca just for being the strongest person I know.

Declaration

This report has been created by myself and has not been submitted in any previous application for any degree. The work in this report has been undertaken by myself except where otherwise stated.

Part I

Introduction and Background

Chapter 1

Introduction

Visual Effects (VFX) is a rather unique area of modern audio-visual productions: in the same medium art and technology are blended together to give the audience an emotional experience, ultimately supporting the story that the director wants to tell. This thesis focuses on one of the stages of the movie VFX production and in particular on the methods and techniques used to make digital characters in motion look realistic. In order to achieve this desired level of realism, physics-based animation (PBA) is applied in such a way that the motion created by the animators is enhanced by the physically plausible deformation of anatomical tissues (muscles, fascia, fat and skin). This deformation makes the character look alive through effects such as jiggling, wrinkles and bulging, which, overall, contribute to bridge the gap towards crossing the so-called *uncanny valley*. In this chapter, topics such as the VFX pipeline, physics solvers and anatomy are introduced to provide the necessary background to follow the work and frame it in the global setting of movie production.

1.1 Research Problems overview

There are many reasons why a visual effects company specializing in digital creatures should invest in innovation towards a physically-based character deformation pipeline. First of all, the level of realism that can be achieved is much higher than standard methods: the world is volumetric, objects including bodies and tissues are not hollow (as modelled typically in VFX), but dense and respond to the laws of physics, collisions and contacts. Movies nowadays contain massive amount of computer generated characters and it is important to not disappoint the main customers of this industry: the people and the fans going to the cinemas or paying for streaming services to watch amazing, thrilling moving pictures. Therefore it is crucial to deliver visually stunning, plausible and integrated computer generated content.

Because we are immersed in our 3D world and our brains are so specialized in detecting anomalies in dynamic behaviours that conflict with our internal expectation of physics, producing unrealistic deformations for the body and the face of a character in motion would ruin the sense of immersion of the beholder and these anomalies would be quickly picked up, consciously or unconsciously. Our perception is tuned to the laws of physics since childhood: for instance, in real-time we make inferences and predictions about the trajectory that an object is taking or the jiggling of a body in motion, based on visual clues, structure and prior knowledge about the material properties. This leads us to make predictions that put in words would be for instance: "This character looks fat and with a lot of mass therefore will move slower than a muscular and fit one" , or: "This ball shot by a cannon looks like metal so it will not bounce much when impacting with the ground". Therefore, even though an excessive stress on the physical accuracy of the simulations is not the real goal pursued by Visual Effects artists, a physics-based approach to anatomical simulation provides many benefits. Visual plausibility and being faithful to the director's vision are priority instead and it would be an overkill adopting blindly a medical level accuracy in VFX, considering the computation times and artistic effort required.

In practice, the choice of which character pipeline to adopt boils down to deciding where to put the complexity of the process. Procedural deformers and standard skinning techniques allow achieving quickly visually good results, but require a lot of artistic effort in sculpting blend shape correctives (i.e. deformed shapes with the same topology but different vertex positions that get interpolated); dynamics have to be achieved with simulations on top of the cached geometry or with fast deformers that "fake" secondary movements. Despite giving great level of control, the problem of this approach is that it relies exclusively on the artist's ability to animate, with several constraints such as volume preservation. On the other hand an approach purely physics-driven instead puts the complexity at the beginning of the chain. Even though artists have to spend significant effort setting up the inputs of the system such as skeleton, muscles, fascia, and fat layer geometries, they can benefit at a later stage from the use of realistic materials and accurate, predictable results. Nevertheless, in practice the problems of this approach are at least as many as its benefits: being so dependent on the accuracy of the inputs, when changes have to be made at the beginning of the chain, often the expensive simulations have to be recomputed. In addition, controlling the behaviour of the solver (which has to solve for collisions, material model forces, constraints) and the shape of the resulting anatomical model is not a trivial task, especially in a production environment.

1.2 Aims and Objectives

This work aims to avoid the drawbacks of purely physics-based approaches and is not intended to achieve medical level results. Rather than focusing only on improving the speed of the solver itself by switching from FEM to other alternatives (Projective Dynamics (Bouaziz et al. 2014), PBD (Müller et al. 2007) and more recently XPBD (Macklin et al. 2016)), this work shows how to cope with the problems of complexity arising from the rest of the pipeline, in particular its inputs. We can say, using a mathematics metaphor, that the optimal character pipeline is a weighted average of the costs and benefits of all the aforementioned methods that maximizes the visual realism of the output and minimizes its production cost by considering parameters such as: computation time, difficulty to setup, effort required to correct the output, artistic control, stability.

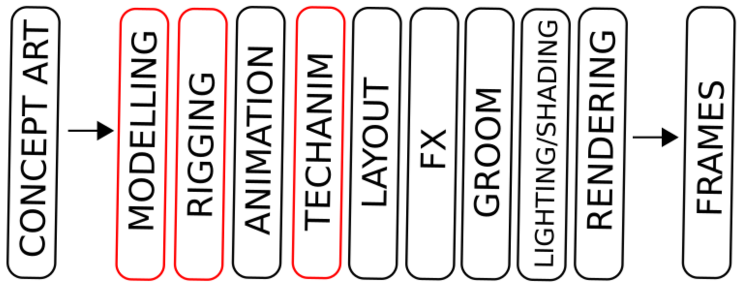

Figure 1.1: *Simplified 3D movie production pipeline.*

The objectives of this work can be summarized as follows:

O1 To research and develop physics-based volumetric simulation methods for characters.

O2 To demonstrate that ad-hoc physics-based methods are a good solution to the problem of the production of realistic deformations in Visual Effects.

O3 To show that new tools and approaches are needed to overcome the drawbacks of physics-based methods such as input primitives creation and anatomy placement.

O4 To present possibilities of applying machine learning to the generation of physically plausible deformations, with the intent of avoiding computationally expensive solver operations.

1.3 Character Effects Pipeline

In this section a typical character production pipeline is briefly described, positioning it in the context of the production of the whole movie.

Creating a movie which combines live action plates with computer-generated imagery (CGI) in a realistic seamless way is an extremely complex, time consuming and challenging task. Hundreds of artists, technical directors, animators, engineers, developers and producers have to work on sometimes thousands of shots, ensuring that the resulting moving images are consistent across the whole movie and that the story is conveyed at its best. Figure 1.1 shows a simplified version of the pipeline of any 3D moving picture production that uses computer generated assets. This is briefly described in the following paragraphs.

Character production is just a part of the pipeline and like everything else in the world of creative industries, it starts with an idea often in the form of a description by words or rough sketches. Taking that initial idea, the art department provides detailed concepts, proportions, exact measurements, comparative scale sheets and scans (when available) in order for the modellers to start creating initial versions of a mesh. The departments of interest for the scope of this work are Rigging and TechAnim. Rigging is responsible for the creation of three kinds of setups: a low resolution puppet rig usable in real time by the animators; a facial setup; a high resolution final quality rig comprising anatomy (skeletal bones, dynamic muscles, fat, dynamic skin effects such as wrinkles). A variety of solvers, deformers and techniques allow the completion of this task for which the goal is to deliver to the next stages of the VFX pipeline a high resolution mesh cache which deforms in a realistic way (a cache is a file containing the encoding of the vertex positions per frame). The rigging department collaborates closely with TechAnim who take care of solving character effects problems that need ad-hoc solutions such as contacts with other characters and objects and extra dynamics on the tissues. This is often done on a shot by shot basis. After TechAnim, the pipeline continues to lighting, shading and rendering. The sets produced by layout, the digital matte paintings by the art department, the digital effects (particles, fluids, destructions,explosions etc) and the curves by the groom department and the animations are combined to produce the final pixels of the images we admire on the screen.

The creation of a 3D character setup is often a long and iterative process. In the case of digital doubles (perfect 3D digital versions of a real actor) the anatomy is known a priori and the rigging process can start from a human-like template. For a fantastic creature the process is similar, but a greater amount of conceptualization work is needed to come up with a plausible inner anatomy for it, often creating a unique set of bones and muscles that never existed before. This task is informed by existing anatomies of natural world species, often combining different parts of them (for example in the case of a dragon-like creature the references could be snakes, lizards, dinosaurs).

1.3.1 Musculo-skeletal Systems

There are areas of the Visual Effects pipeline that have received a lot of attention since the early years of computer graphics research. In particular the simulation of natural phenomena such as water, gase and fracturing of materials. Deformable objects have also been researched for at least thirty years, but their application to anatomical simulation and character effects is relatively recent, pushed and pioneered in particular by companies such as Weta Digital (Clutterbuck & Jacobs 2010), MPC, ILM (Comer et al. 2015) and Framestore, who have to produce photo-realistic CGI. "Muscle systems" as a broad term refers to a set of techniques and workflows intended to reproduce in 3D the internal anatomy shape and physical behaviour of human-like or fictional characters, with the goal of obtaining dynamic deformation of skin, flesh and other biological tissues which is indistinguishable from reality. For a discussion of these tissues from an anatomical point of view, please refer to Chapter 2.

A physics-based system for flesh simulation comprises various iterative stages to be completed. First, based on anatomy atlases and previous knowledge or scan data, modelling artists create the geometry of:

- Skeletal bones
- Muscles and tendons (mainly the superficial ones)
- Internal organs (optional)
- Fat tissue
- Skin (renderable geometry)
- Veins (optional)

- Facial blend shapes

This geometry should be ideally intersection-free, one of the reasons being that intersections would generate unwanted initial spurious contact forces during simulation. For this purpose asset checking tools can be used before sending the meshes down the pipeline. This problem is discussed in more detail along with potential solutions in Chapter 3 in which a workflow for muscle placement that prepares simulation-ready anatomical geometry is presented. Once the geometry is approved, riggers place skeletal joints where articulation is needed, take care of the skinning of the mesh to these transformation points, add deformers to achieve procedural effects for sliding, contact and jiggling and custom setups for props. Riggers also create the set of control gizmos for body and face that animators will keyframe and from which animation curves will be later exported.

One additional advantage of using an anatomy-based approach is connected to the fact that rigging and character effects are just a part of the larger movie VFX pipeline. In fact having the geometry and the deformation of internal organs, veins, muscles, tendons, bones and fat allows the rendering stage to achieve extremely visually realistic results, by assigning different shaders (procedural programs that describe how the light should interact with the geometry to render a desired material look) to each layer and using complex subsurface scattering diffusion algorithms for the outer skin. This, when paired with physically-based rendering of materials, conveys a level of realism that requires less effort than using geometry without internal anatomy. Research on anatomy-based approaches constitutes the core of this work which was carried out in two London based companies.

1.4 The Companies

My Engineering PhD (EngD) experience with the Centre of Digital Entertainment began with the first of two companies in which I completed the 4 years programme. Prime Focus World gave the opportunity to work on a variety of Research and Development (RnD) projects at their London studio. A bit after the end of the first year though, the company underwent a series of structural and business changes which led to lose the researcher job position and forced to search for a new hosting company. After some interviews, I got offered a position at MPC London to continue the EngD. Even though the topics of the research changed after the transition, the main area stayed the same and MPC provided a better research environment. Below is a summary of the two companies and a brief description of the experience in terms of completed projects.

1.4.1 Prime Focus World

Prime Focus World (PFW) is a film-making partner to international studios and film production companies, providing world-class creative services, pioneering technology services and intelligent financial solutions on a global scale. From script to screen, PFW partners with production companies and brands to develop and deliver animated CG content, offering the scale and experience to deal with projects of any size. Animation credits include a number of full-length feature films and over forty episodes of a fully CG animated TV show for a major global toy brand. In 2014, PFW merged its VFX business with Double Negative (Dneg), an Academy Award winning VFX industry leader with facilities in London, Vancouver and Mumbai. PFW was the first company in the world to convert a full Hollywood film from 2D to 3D, and its patented, award-winning stereo conversion process has been used on more blockbuster Hollywood films than any other.

1.4.2 MPC

The Moving Picture Company (MPC) is a London based VFX house. It has been one of the global leaders in VFX for over 25 years and counting, with industry-leading facilities in London, Vancouver, Montreal, Los Angeles, New York, Amsterdam, Bangalore and Mexico City. Some of their most famous projects include blockbuster movies such as Godzilla, the Harry Potter franchise, X-Men, Prometheus, Life of Pi, Guardians of the Galaxy and The Jungle Book. The services they provide include concept design, pre-viz, shoot supervision, 2D compositing, 3D/CG effects, animation, motion design, software development, digital & experiential production, colour grading for advertising and any combination of these services.

1.4.3 Experience at Prime Focus in a nutshell

From October 2013 to early January 2013 I worked at Prime Focus on the development of Nuke plugins for the View-D department. This department is the one that focuses on the technology for the stereo conversion of movies to stereoscopic 3D through proprietary software, in particular custom nodes for Eyeon Fusion. Therefore my initial tasks were to convert some of these nodes to The Foundry's Nuke compositing package. I developed various nodes (plugins) that were tools to analyze single frames and sequences of images in order to visually and numerically detect spurious pixels. These nodes were used for disparity maps and were aimed to help the artist to find anomalies in sequences generated by Ocula. One of these nodes made use of QT drawing tools to integrate a dynamic histogram to facilitate the artist setting thresholds on a UI rather than via float inputs. In that period I had the opportunity to learn Nuke C++ NDK (API) and deepen my knowledge of QT. Starting from mid January 2014, I could concentrate more on actual research and exploration of relevant topics. Therefore I started studying literature about the techniques used in computer graphics for soft body deformation and fracturing. The idea was to find ways to express materials in terms of their microstructures to solve the problem of the lack of detail in the internal parts of fractured objects. From there the interest shifted to the modelling and simulation of heterogeneous materials because of the need to approximate real world materials with more accuracy. Anisotropy is a characteristic of many interesting real world materials and its application to computer graphics is still somewhat limited, therefore worth exploring. Towards the third quarter of the year, so around June 2014 the company proposed 2 topics:

- creation of huge vegetation landscapes and scenarios with optimization both for modelling and rendering in mind. The system had to be extremely efficient and user friendly and support effects like wind and contact from characters, ideally crowds;
- large scale cloud simulation with fluids and control.

Therefore I started researching the simulation of clouds as a fluid and other atmospheric effects. Unfortunately a few months later I lost the position because of the restructuring of the company and the clouds project remained at the level of literature review and very early implementation.

1.4.4 Experience at MPC in a nutshell

At MPC there was the need to prototype a system to prove the potential of the physics-based techniques developed in engineering and academic settings. The first months at the company were spent implementing in Maya and extending the Implicit Skinning framework (Vaillant et al. 2013), a procedural method that makes use of distance fields. This proved to be a really good way to get used to the company tools and practices. Also, it introduced me to the positive collaboration with my Industrial Supervisor and the rest of the RnD team. Procedural methods are in general fast and work well for secondary characters, but hero characters with detailed anatomy require more advanced techniques, especially to achieve good dynamics effects such as skin sliding and fat jiggling. Therefore, the research proceeded towards the extension of an open source Finite Elements library (Sin et al. 2013a) to create a system for tissue simulation, equipped with constraints and fibre activation. It gave the foundations and showed the path to use physics for other parts of the character pipeline which constituted problems in a practical production environment. In particular, even if the system showed good potential, it became clear that the inputs of the systems and the way to create rigs in this new anatomical manner were problematic and needed to be addressed. In fact, in a real production, the solver itself constitutes a necessary but not sufficient condition to achieve the results that riggers and Effects Technical Directors (FX TDs) envision for the human or creature under consideration. What makes the difference is not only the presence of tools and methods to prepare the setup needed by the solver, but also to control the behaviour of the solver (artistic control). This constituted the motivation to carry on research for the primitive modelling tool based on inflation and the interactive placement tool which, as a by-product, led to publication. Another motivation for the shift from the central importance of the solver and simulation method towards side tools and techniques to help artists in the anatomical inputs work was the fact that, concurrently to my experience at MPC, an external player came to the market with a plugin for tissue simulation (Jacobs et al. 2016). The plugin was not adopted by MPC, a fact that confirmed the will of the company to push instead on the existing proprietary internal technology (successfully used for the Oscar-winning movie 'The Jungle Book') and carrying on Research and Development (RnD) on the tools needed to ensure a proper transition to physics-based character animation. In that period towards the end of the third year, my industrial supervisor changed.

In the final period of the EngD, driven both by personal interest and MPC's awareness of its growing potential, I started to focus on machine learning. Encouraged by some very recent existing research on data-driven fluid simulation and other researchers in the mother company Technicolor, I dedicated my time towards a project using the now popular Deep Neural Networks running on powerful Graphics Processing Units (GPUs) with the goal of learning the physics of deformable objects simulation. The outcomes of the project are described in Chapter 7.

Even though the prototypes developed have not been used in production, at the end of this experience some valuable lessons have been learned to improve future systems as discussed in part III.

In addition to the publications listed in appendix A, three software department presentations were given at MPC and one at a conference of a leading company in rendering technology held in Sofia, Bulgaria (Chaos

Group 2015).

1.5 Contributions

Table 1.1 summarizes some of the problems described above; it contains also the outcomes of the work in terms of public engagement and publications. The contributions consist of:

1. The creation of a custom simulation framework using FEM built on top of the VEGA library to help the company in testing a new physically-based approach to character deformation. Formulas were derived to implement muscle activations for a constitutive material enriched with fibres. Constraints and collisions were also added to the framework, contributing to the creation of a usable prototype.
2. The creation of a novel method consisting of an interactive physics-based design of muscle anatomical geometries ready to be simulated.
3. The development of tools and techniques to interactively place muscle geometries on a skeletal bones rig taking into consideration collisions.
4. A procedural method for skinning using implicitly-defined scalar fields was extended to create wrinkle effects.
5. The investigation of the application of Deep Learning to the simulation of deformable objects with the aim of improving the speed of a standard solver.

The list of publications is presented in appendix A.

The five projects listed above are united by the common denominator of the research and development of techniques to improve the realism of character deformations in a movie pipeline. In fact, the muscle primitives obtained with the superficial patch system can provide the input for both the physics engine and the placement tool. The procedural wrinkle effects

Problem	Contribution	Publication/Outcome
Transition to PBA	Tissue framework	FMX 2015 presentation
Input setup	Superficial patches	Eurographics 2017
Artistic Control	Muscle placement	Siggraph 2016
Procedural Deformers	Wrinkles for Implicit Skinning	CVMP 2015 and Siggraph Asia 2015
Speed of the solver	Deep learning	Internal Presentation

Table 1.1: *List of contributions*

could be added as a post process on a coarse simulated geometry and the pilot machine learning approach could be used at the end of the pipeline to speed up the whole deformation system.

Besides this input/output logical connection, exploring procedural approaches as first project (in a chronological sense), also gave the possibility of qualitatively evaluating the results later against physics based approaches obtained with the simulator.

1.6 Thesis Outline

This thesis is structured as follows. In part I this first chapter provides an introduction to the hosting companies, the character effects pipeline adopted in modern movie production and an overview of the projects completed; chapter 2 gives the necessary background on anatomy and a general literature review on physics solvers. Part II describes five projects (chapters 3-7) in a portfolio style: each one contains its own related work and conclusions, explaining the relation and connection with the other projects in an organic way. Part III discusses the results from a global perspective and draws conclusions on the work done, together with all the future work to improve the presented methods. Finally, a list of publications and detailed derivations of formulas are shown in the appendices.

Chapter 2

Background

The problems that this work tackle lie at the intersection of multiple disciplines: anatomy, biomechanics, computer science, art production. Therefore in this chapter some foundational knowledge on these areas and notions will be given. First, the foundations of muscle and tissue anatomy are given. In fact, the observation and the study of how reality looks and works at a micro and macro level, inform the choices of computer graphics techniques and algorithms. After presenting the main anatomical components which are the scope of this research, the chapter gives a broad level overview of what a muscle system is and its use in Visual Effects. The chapter then continues by giving mathematical foundations of the equations governing the dynamics of motion in a physics solver, in particular its standard and variational forms. Finally, an extensive literature review of the existing approaches and methods to deformable objects is given, dividing them in four main categories: offline, interactive, procedural and learned methods.

2.1 Anatomy Background

There are over 650 muscles and 206 bones in the human body, with the addition of various kinds of soft tissues presenting various degrees of elastic material properties. The interaction of all these components during motion increases the complexity of the resulting dynamics because connected tissues are coupled and forces propagate in this intricate biological structure. In this research deep muscles that have negligible effect on the surface appearance are simplified and discarded, bringing the number down to about 110 and 100 relevant muscles and bones, respectively.

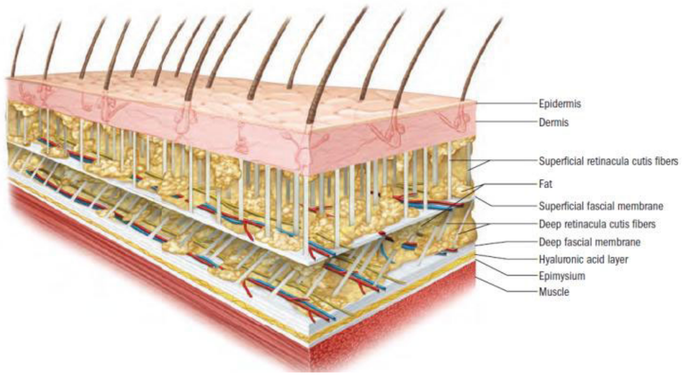
Epidermis
Dermis
Superficial retinacula cutis fibers
Fat
Superficial fascial membrane
Deep retinacula cutis fibers
Deep fascial membrane
Hyaluronic acid layer
Epimysium
Muscle

Figure 2.1: *Skin anatomy. From top to bottom: epidermis (skin), dermis, fat tissue, muscle © (Massage Research 2013).*

Below are described, from inside to outside, the main layers modelled in this work and their function in the body (Figure 2.1).

2.1.1 Bones

Bones are strong but lightweight components of the skeleton. Their material is composite and internally they resemble a matrix structure. Bones are connected at their joints by cartilage tissue and present some elastic characteristics to prevent fractures. At the interacting joints, bone heads present generally irregular shape which often results in a roto-translational movement.

2.1.2 Muscles

Muscles can be considered as an organized set of contractile units called *sarcomeres*. At the micro level, sarcomeres contain two important pro-

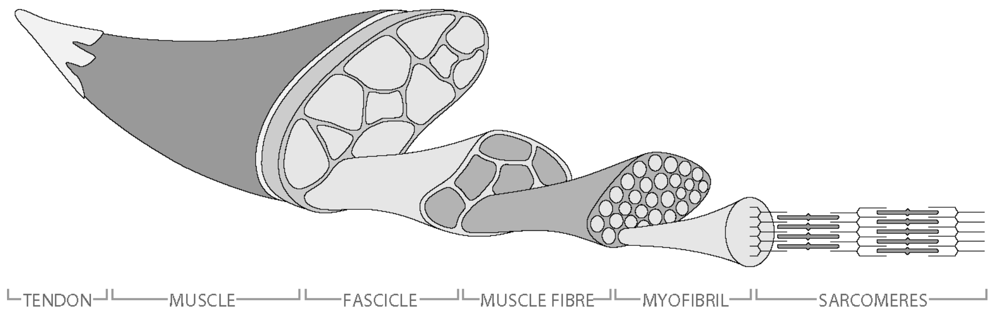

Figure 2.2: *Hierarchical structure of a striated muscle (Lee et al. 2012).*

teins called *actin* and *myosin* which chemically bind and overlap on each other during contraction, thus being ultimately responsible for the bulging look at a macro level, together with the conservation of volume due to the contraction happening in a closed area made of incompressible material (mostly water).
Muscles present a hierarchical structure: sarcomeres are grouped into *myofibrils*, which make muscle fibres; in turn muscle fibres group into fascicles. Fascicles are separated one from each other by the *endomysium*. The *epimysium* is a dense connective tissue that wraps the muscle and protects it from friction with neighbouring components. Figure 2.2 shows a representation of the aforementioned components.

Muscles present various configurations of fibres and internal architectures, based on their shape (Figure 2.3). For example, the gluteus maximum has a pennate architecture while the bicep brachii has a fusiform one. These characteristics must be taken into account in a simulation system.

When activated, muscles bulge and their shape depends on the rest pose configuration (i.e. the initial vertex position prior to any deformation), the fibre density, their internal fibre architecture and the fact that they interact with the surrounding muscles and fascia. Bodybuilders know very well that the range and kind of exercises for specific muscles influence determined fibre areas. For instance, bicep curls that are more or less extended (in terms of arm angle) can shape the bicep brachii differently because different fibre groups are exercised (broken and repaired) (Siegel, Jeffrey 2015). Moreover, it is important to distinguish the bulging due to activation from the one due to the growth caused by physical training.

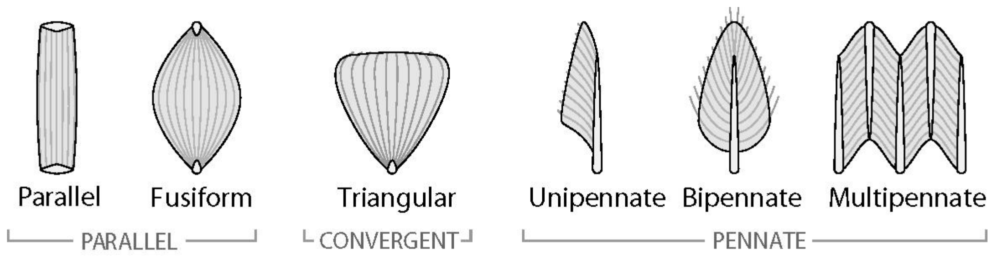

Figure 2.3: *Types of muscles based on their shape and internal fibres architecture (Lee et al. 2012).*

Muscles are complex in structure and physiology and therefore pose interesting challenges in terms of modelling and simulation. In fact "[...]muscle tissue has a highly complex material behaviour - it is a *nonlinear, incompressible, anisotropic, hyperelastic* [and *heterogeneous*] material[...]" (Teran et al. 2003). The meaning of these terms is as follows:

Nonlinear: the stress/strain relationship is not linear like for example the one for rubber.

Incompressible: volume must be preserved to avoid visual artifacts.

Anisotropic and active: the simplest materials are isotropic. This means they respond equally to transversal and longitudinal forces, but since fibres in muscles grow in defined patterns, the deformation they undergo is different for stresses applied in different directions.

Hyperelastic: soft elastic material that undergoes large deformations.

Heterogeneous: a combination of different layered tissues with different material properties that interact with each other in a limited amount of space.

2.1.3 Tendons

Tendons are made of multi-stranded fibrous connective tissue (mainly a protein called *collagen* which "glues" components together) and they constitute the extremities of the muscles in the region where they attach firmly to bones to support contractile tension. Tendons are often modelled as completely inextensible, but they are actually flexible and stiff at the same time. In fact their elastic properties are important not only for transmitting forces to the bones and allowing the muscles to bulge, but in some cases they behave like springs to store and release energy during motion for efficiency (like the Achille's tendon during the stride). The Hill-type model (Zajac 1989a) takes this behaviour into consideration. Tendons are visible on the skin in particular in superficial areas of the hand, wrist and foot where they can be seen sliding and convey overall sense of tension.

2.1.4 Fascia

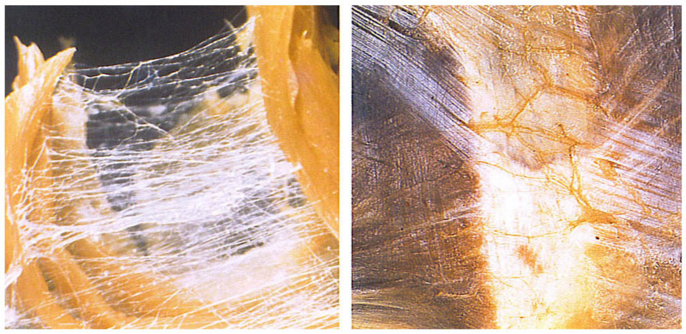

Figure 2.4: *Fascia at work © (Fortier 2013).*

Fascia is an extremely important component of the musculo-skeletal system. In a broad sense it is the soft tissue webbing of the body. It can take the form of sheets, but in general is a 3D network of connective tissue. Its main function is to hold muscles, organs and other components together. Without fascia our body parts would literally fall apart. Fascia connects muscles to other muscles. The fibres constituting the fascia keep forming and breaking all the time, but with lack of movement tend to make the muscles stick together too much (a process called *adhesion*) and create dragging forces one on another, something that reduces the natural sliding and augments friction (Stecco 2012)

Keeping in mind that fascia is a global system, it can be subdivided for simplicity into *superficial* and *deep*. Superficial fascia is the layer of viscoelastic subcutaneus loose connective tissue that mainly determines

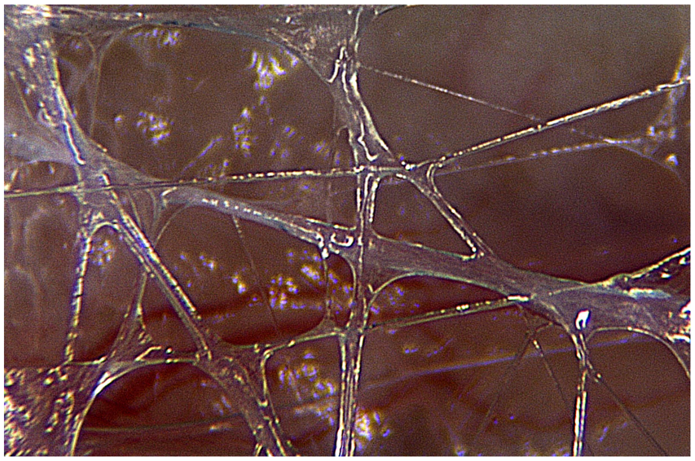

Figure 2.5: © *Fascia fibres (Myotherapies 2013).*

the shape of a body. Deep fascia takes different names based on the location of the connective fibres: *epimysium* when acts as a coat of a single muscle and *endomysium* when continues towards the interior of the muscle holding the fascicles together. Its function is not only to contain and stabilize, but thanks to its fibre connections it can transmit the tensional forces coming from the underlying fibres to the neighbouring components so that parts of a limb at a distance can be organized by one single movement. In addition, some parts of the fascia can slide over the fibres to transmit force to the limbs while other parts are attached to them and are actioned by the fibres. This mechanism allows the creation of synchronizations between muscles.

What really matters in computer graphics is that the superficial fascia can slide freely over the deep one. In reality it is not the skin that is sliding (Clutterbuck & Jacobs 2010), (WETA Digital 2013), but because there are various layers that can shear, the epidermal fat is compressed by the underlying bulging muscles (or moving bone) that slide under this elastic sheet and the effect is a travel of the skin features visible to the naked eye.

2.1.5 Fat

Between the fascia and the *epidermis* (skin) there is a more or less thick layer of adipose tissue. It is present almost everywhere on the body but it accumulates more in certain areas, typically the belly, the arm and the *gluteal* region. While the muscles mainly give the basic deformation and silhouette of a character, it is the fat layer which gives most of the interesting secondary effects such as jiggling, wave propagation due to impact and sense of inertia.

2.1.6 Skin

Skin can be approximated as an elastic sheet that can wrinkle under compression of the underlying tissues. When stretched it tends to return to its original configuration with a nonlinear delay. Skin is of primary importance in computer graphics because, except for particular cases where seeing the underlying anatomical geometry is needed, it is the layer that is visible and renderable.

2.1.7 Veins

Veins form an indispensable network for the circulatory system. In graphics, even if often neglected, they are particularly important to convey realism. In fact veins are always visible and they stand out not only for their blueish colour, but also for their displacement. When muscles contract and undergo a medium-high effort, veins become more pronounced for the larger amount of blood that flows in and out the fibres and the higher pressure. For this reason they should be taken into account for maximum realism.

2.2 Muscle systems background

In the VFX pipeline, at the stage of muscle simulation, rigging starts to blend with character FX: the anatomical tissues have to be combined into layers and be simulated in each shot. For that purpose, muscles are first constrained to the bone geometry at their attachment points (*proximal* and *distal* insertions of the tendons) and to each other with a combination of hard, soft and sliding constraints. A non-volumetric geometry component is then procedurally generated from the outline of the bones and muscles: it wraps them tightly and that functions as the anatomical fascia. The fascia is responsible for holding the deforming muscles together and forming a clear separation from the volumetric outer layer that constitutes the fat directly attached to the renderable skin. All these layers interact with each other and are (ideally) simulated all at once to obtain physics coupling. This is computationally expensive so a common strategy is to simulate the layers separately generating a geometry cache for each to drive the next. Despite being more flexible, the drawback of this approach is that it cannot obtain a physically and visually correct coupling or bidirectional transfer of inertia during animation (Jacobs et al. 2016). By placing constraints and specifying correct material properties (Young's modulus, Poisson ratio, stiffness), the solver of choice will compute forces, stresses, contacts and collisions. The result is an anatomical mesh that follows the animation of the character, but is enriched with fibre activations, muscle and bones sliding under the fat, skin wrinkles and jiggling effects which add that level of realism highly sought after and appreciated in Visual Effects. In real productions, the process described above is highly nonlinear and heavily iterative.

As mentioned earlier this approach is not free from problems that have to be carefully considered. For example given the effort needed to obtain the anatomical muscles for a character, transferring algorithms have to be developed and practical tools given to artist when, for production reasons, the skin and proportions of the character have to be changed. Similarly, when for a shot the muscle and fat simulations result in shapes that are anatomically correct but do not convey the director's creative intention, shapes have to be corrected and coexist with the simulation pipeline. These kind of situations are the "bread and butter" of everyday VFX movie production.

While muscle systems are generally intended for the body, research is advancing their use for facial animation, an area where simulation is being adopted especially for blend shape-based tetrahedral rigs (Kozlov et al. (2017), Ichim et al. (2017)). Facial muscle systems are more challenging than the body ones because detailed facial expressions require extreme amount of detail (i.e. wrinkles), high levels of controllability are difficult to be provided and also because the face contains very thin muscles which pose problems for the solvers.

Specifically at MPC riggers take care of the generation of the muscle geometry, via a custom procedural system that from 2D morphable sheets skinned to the joints generates an approximation of muscle anatomical shapes (Fig. 2.6). After controlling that the character deforms correctly, a mass-spring system adds approximated dynamics to the muscles which are connected to the skin via a custom skin deformer that roughly behaves like a highly controllable quasi-static cloth simulation, producing secondary effects such as wrinkles. Because of the lack of fibre-based mesh contraction, the rig is equipped with "sensors" of compression and extension based on joint angles and impact zones that activate custom sculpted blend shapes (flex-shapes). While this solution is very art-directable, Rigging and Techanim needed a system that produced more physically-based realistic results which constitutes one of the motivations behind the proposed methods and tools described in this work.

2.3 Solvers and Methods for Deformable Objects

Muscle systems are modelled as deformable objects. Here some background and mathematics for deformable objects will be presented.

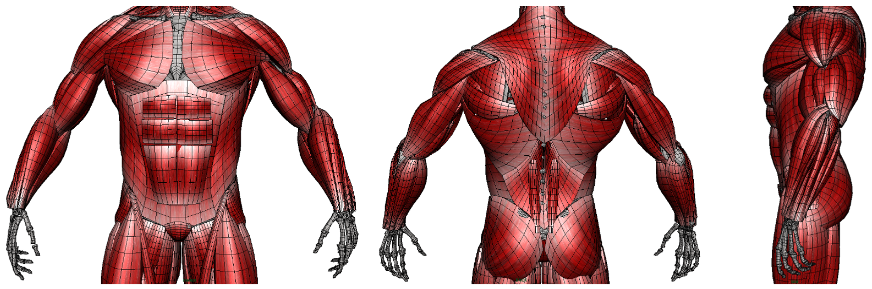

Figure 2.6: *Front, back and side muscles of arm and torso (MPC muscles generated from anatomical sheets).*

To give some initial basic definitions, the deformation of a mesh element (i.e. triangle or tetrahedron) expressed as a vector of vertex positions in rest pose $\mathbf{X}$ to a deformed configuration $\mathbf{x}$ can be defined by a function $\mathbf{\Phi}(\mathbf{x})$. The Jacobian of this function constitutes a basic description of the severity of the deformation (variation with respect to the rest pose) and it is called the deformation gradient, widely indicated in the literature as F.

A physics solver's task is to provide at each timestep a solution to the partial differential equation of motion:

$$\mathbf{Ma} + \nabla_{\mathbf{x}}\mathbf{W}(\mathbf{X}, \mathbf{x}) = \mathbf{f_{ext}} \tag{2.1}$$

where $\mathbf{M}$ is the mass matrix, $\mathbf{a}$ is the acceleration, $\mathbf{f_{ext}}$ are the external forces (gravity, wind, constraints, contact forces) and $\mathbf{W}$ is an elastic potential that typically expresses the kind of material to be simulated. Different materials have different properties: in this work we will focus on hyperelastic materials and in particular the St Venant-Kirchhoff (StVK) invertible model (Bonet & Wood 1997).

There are mainly two ways to solve this equation in time for a deformable object:

1. Using an integration scheme for the PDE and solving the resulting nonlinear system
2. Transforming 1. into an equivalent energy minimization problem

The first approach integrates the discretized differential equations of motion by solving a nonlinear system for which the solution is the velocity at the next state. The most stable and popular way to do this is using Implicit Backward Euler integration. Given the state of the system (q_n, v_n) at time n, Implicit Euler adopts the following update rule:

$$\begin{aligned}\mathbf{q_{n+1}} &= \mathbf{q_n} + \mathbf{h}\mathbf{v_{n+1}}\\ \mathbf{v_{n+1}} &= \mathbf{v_n} + \mathbf{h}\mathbf{M}^{-\mathbf{1}}(\mathbf{f_{int}}(\mathbf{q_{n+1}}) + \mathbf{f_{ext}})\end{aligned}$$

where h is the time step size (discretization of time). The fully implicit nonlinear equation therefore becomes:

$$\mathbf{M}(\mathbf{q_{n+1}} - \mathbf{q_n} - \mathbf{h}\mathbf{v_n}) = \mathbf{h}^{\mathbf{2}}(\mathbf{f_{int}}(\mathbf{q_{n+1}} + \mathbf{f_{ext}}))$$

As will be shown in chapter 4, the solver used in this work instead adopts a semi-implicit integration scheme, that linearizes f_{int} through its gradient with respect to the nodal positions which is called the tangent stiffness matrix K.

The second approach is to express the Implicit Euler integration as a minimization problem and therefore takes advantage of a long tradition of research in the mathematical optimization field:

$$\min_{\mathbf{q_{n+1}}} \frac{\mathbf{1}}{\mathbf{2h^2}} \|\mathbf{M}^{\frac{1}{2}}(\mathbf{q_{n+1}} - \mathbf{q_n} - \mathbf{h}\mathbf{v_n} - \mathbf{h}^{\mathbf{2}}\mathbf{M}^{-\mathbf{1}}\mathbf{f_{ext}})\|_{\mathbf{F}}^{\mathbf{2}} + \sum_{\mathbf{i}} \mathbf{W_i}(\mathbf{q_{n+1}})$$

which expresses the fact that the solution (positions at time $n + 1$) is a compromise between the momentum potential plus external forces (first term) and the total elastic potential (second term). Chapter 7 shows that this potential can become a suitable loss function for a machine learning algorithm.

The resulting nonlinear system of equations is generally solved with one or more iterations of the Newton-Raphson method. The linearization of the equation via the Newton procedure leads to a sparse positive definite linear system that can be solved with a Preconditioned Conjugate Gradient (PCG) solver or direct solvers (Sifakis & Barbic 2012). Existing work on solvers and methods for deformable objects is presented below, divided for convenience into four macro categories: offline, interactive, procedural and machine-learning based methods.

2.3.1 Offline Physics-Based Methods

Deformable models have been studied in computer graphics for nearly 30 years now, starting with seminal works (Terzopoulos et al. (1987), Terzopoulos & Fleischer (1988)) which showed the potential of computational physics to simulate fracture, deformation, viscoelasticity and plasticity using mainly a finite differences discretization. To deal with large deformations, O'Brien & Hodgins (1999) and O'Brien (2002)) used a St.Venant-Kirchhoff (StVK) nonlinear material model based on quadratic Green strain. Müller & Gross (2004) contributed to solve the problem of linear elasticity artifacts for large deformations by introducing in the framework of the Finite Element Method (FEM) (Sifakis & Barbic 2012), (Bonet & Wood 1997) the popular corotational method (warped stiffness) that extracts the rotation of the deformation gradient F via polar decomposition (alternatively, QR decomposition). In fact rotational modes have to be filtered out so that they do not contribute to internal forces. Volume preservation was addressed in (Irving et al. 2007).

The coupling of computer graphics with biomechanics in recent years has led to a more anatomically "conscious" approach to character animation. The underlying assumption of the following methods is that an accurate geometry representation of the internal anatomical components, coupled with physics-based simulation, gives the most realistic results. Teran et al. (2005b) and Teran et al. (2003)) simulate muscles and flesh from the Visible Human data set using a variation of classic FEM, the Finite Volume Method, supporting: active and passive components (tendons), an effective constitutive model based on fibres and degenerate and inverted tetrahedra (via SVD decomposition that diagonalizes F (Irving et al. 2004)). After these works had shown the approach as being very promising, other researchers concentrated on the physics-based simulation of the human hand (Sueda et al. 2008), the upper body (Lee et al. 2009) and human swimming coupled with fluid dynamics using Lattice Deformers (Si et al. 2014), (Patterson et al. 2012).

Forces in elementary muscle units (sarcomers) have been represented classically through the Hill-Zajac model (Zajac 1989b) which is an acceptable 1D simplification of the macroscopic forces. Biomechanics started relatively recently to adopt 3D muscle simulation (Blemker & Delp 2005), to predict shapes during contraction and internal stresses to prevent injuries in a much more accurate way than before (Comas et al. 2008), (Delp et al. 2007). Non-volumetric muscles are also used for control of animation, often in conjunction with quadratic programming techniques to resolve contacts (Tan et al. 2012), (Geijtenbeek et al. 2013)

The price to pay to have accuracy is quite high in computational terms and methods to trade speed for physical correctness are an area of active research. In fact typical full body models can easily reach 1 million tetrahedral elements. Moreover such biomechanical systems are difficult to model, setup and control without dedicated tools which generally are very different from the ones present in traditional Visual Effects rigging pipelines.

Recently, McAdams et al. (2011) created a production-ready system for the deformation with contacts of characters that works both quasi-statically and with dynamics. Using a conforming hexahedral lattice built from the mesh, the method corrects the indefiniteness of the stiffness matrix to fix instabilities of the warped stiffness method and makes use of a fast multigrid solver which achieves near-interactive performance.

A new approach to deformation that is inspired by fluid dynamics methods is Eulerian Solids in which deformable objects are simulated on a grid through material coordinates mapping and advection (Levin et al. 2011). Its advantages are that it handles collisions well, preserves volume in large deformations and does not need remeshing to avoid instabilities (something needed for Lagrangian methods, subject to mesh tangling).

The method has been applied successfully to muscles simulation (Fan et al. 2014) and its extension, called Eulerian-on-Lagrangian method, allows the simulation of skin sliding (Li et al. 2013) and tendon biomechanics (Sachdeva et al. 2015). Some of the drawbacks are that an explicit mesh has to be mapped and there is no current implementation of internal fibres.

Not only the body but also the face has been the object of study in terms of achieving more realistic dynamics. Kozlov et al. (2017) enrich blend shape animations with secondary motion and other physical effects with a FEM simulation based on the minimization framework by Martin et al. (2011). The method utilizes volumetric blend shapes and per-frame rest poses to guarantee fidelity to the artist's animation.
Ichim et al. (2017) embed simple muscle geometries in a tetrahedral mesh of the face dividing the tetrahedra (tets) that are passive from the active ones and attaching the mesh to the skull with pin and sliding constraints controlled by a map. Muscle activations are obtained from the blend shape animation solving an inverse problem and the muscle model is translation and rotation invariant. Simulation is done by minimizing a set of non-linear potential energies using an interior point solver.

In terms of artistic control of these simulations, Martin et al. (2011) propose an example-based approach where an artist can sculpt a set of target shapes which are interpolated during a physical simulation very smoothly. Each example acts as an additional elastic force but without introducing visible spurious violation of energy conservation. This art-directable way of controlling the simulation avoids tedious parameter tweaking and was extended by Schumacher et al. (2012) to support plasticity and application to a bending muscular arm using pose based dynamics. The development of these methods is fundamental in the context of musculo-skeletal simulation.

Even though all these works achieve stunning results, there are still gaps in the literature for papers that perform dynamic simulation of the combination of all the layers and showing realistic results on the renderable skin of tendons, wrinkles, fascia, self collisions etc.

2.3.2 Interactive and Real-Time Methods

Videogames and interactive applications require new methods to simulate deformable objects at real-time and near-real-time rates. For this purpose the simplest approaches use tetrahedral springs (Mollemans et al. 2003). Müller et al. (2005) introduced the shape matching technique, a mesh-free method that is particularly suited for real time applications and produces plausible deformations although its accuracy is limited by not being physically-based. Kim & Pollard (2011) achieve interactive rates for skeleton-driven non-linear deformation of characters through clever optimizations and parallelizations. Careful algorithmic solutions, often aiming at exploiting GPU architectures, lead to sophisticated real-time surgical simulators and efficient muscle simulation (Mitchell et al. 2015). Model reduction techniques (Barbič & James 2005) aim at expressing deformations as combination of displacement fields (modes).

Position Based Dynamics (PBD) (Müller et al. 2007) is a method that operates directly on the positions of the nodes. In a first step positions are guessed using explicit integration and then validated/corrected by applying distance, bending, volume and collision constraints. Upon validation these values are integrated to new positions. Although it comes at the price of reduced accuracy, this has several advantages: it is easy to implement; it is very controllable; vertex positions can be directly manipulated in real time; constraints and collisions are handled quite easily. The limitations of PBD, in particular the constraint stiffness depending on time step and iteration count, have been addressed recently in the work by Macklin et al. (2016). XPBD extends its predecessor by formulating the constraints in a way that has correspondence with elastic energy potentials and by using total Lagrange multipliers. The result is a fast and stable solver that supports arbitrary elastic potentials (materials).

Recently, Projective Dynamics (Bouaziz et al. 2014), extending the work on fast mass springs by Liu et al. (2013), introduced a new solver that combines FEM with PBD. The solver treats elastic potentials as projections of position configurations on a constraint manifold. This results in a particular form of the potential energy that is minimized via local/global alternated solves. It also supports a wide variety of energy-based constraints.

Projective Dynamics limitations have also been overcome in the work by Liu et al. (2017) by considering it as a quasi-Newton method which allows it to simulate any hyperelasic material and be 10 times faster than one iteration of Newton's method.

Saito et al. (2015) propose a method, built on the Projective Dynamics solver, to simulate the biological growth processes of muscles and fat on a volumetric model. They achieve this by initially decomposing the deformation gradient in growth and elastic components and crafting an ad-hoc potential energy. Even if the results achieved are remarkable and the technique interactive, the system does not cover the possibility for the growth process to fit an existing target mesh, something highly desirable in Visual Effects.

2.3.3 Procedural Methods

Skinning refers to a general class of procedural techniques which are very computationally efficient and commonly used to obtain fast deformations of skeleton-based characters. Geometric/Procedural skinning techniques have been developed in computer graphics for a long time. Shape interpolation and example-based approaches (Lewis et al. 2000), (Sloan et al. 2001) are used in the industry on a daily basis (called blend shapes) while Linear Blend skinning (Magnenat-Thalmann et al. 1988) and dual quaternion (Kavan et al. 2008) have well known issues such as loss of volume or excessive bulging at joints. Jacobson et al. (2011) calculate bounded biharmonic weights for 2D and 3D objects by Laplacian energy minimization subject to bound constraints in a shape-aware, localized manner and with the use of quadratic programming.

More recently Vaillant et al. (2013) proposed the Implicit Skinning with contact technique, followed by its improvement to support skin elasticity with convincing results (Vaillant et al. 2014). These methods have the advantage of being fast, but they generally fail in robustly handling self and external collisions, volume preservation and nonlinear deformations, in addition to the fact that dynamics are often faked.

Deformers are important tools used in the visual effects industry on a day to day basis, especially in Rigging. One of such widely used deformers is the Free Form Deformation technique (Sederberg & Parry 1986), which uses a cubic lattice grid of points to intuitively edit the shape of an embedded mesh. Another popular method to edit shapes is the Laplacian deformer (Sorkine et al. 2004), which has the advantage of preserving well geometric details.

Procedurality and automatisms are also important for transferring of shapes from one character to another. Ali-Hamadi et al. (2013) create a system that can transfer volumetric anatomical models across different target shapes using harmonic energy minimization (Laplacian interpolation) and anatomy rules as constraints. Cong et al. (2015) present a morphing algorithm to transfer anatomy including muscles across faces of different characters, based on feature points and feature curves correspondences.

2.3.4 Methods based on acquisition and machine learning

In recent years other ways to deal with deformable object have been developed. In particular the application of techniques from other areas of Computer Science, such as machine learning and other statistical-based approaches from Artificial Intelligence, have started to become increasingly popular.

Sifakis et al. (2005) acquire activation levels for a volumetric muscle based facial system from sparse marker data. SCAPE (Anguelov et al. 2005) learns from several body scans of people and creates a model dependent on both body shape and pose of the articulated skeleton. Bickel et al. (2009) create a deformable model of heterogeneus materials by finding material parameters given force and strain sample measurements as inputs. Neumann et al. (2013) model the statistical variations of fine scale muscle deformations from reconstructed surfaces of a subject's arms. Their model also supports force application which expresses isometric contraction effects. Zhu et al. (2015) learn anthropometric parameters from point cloud data of a subject's arm acquired with depth sensors and matches a deformed anatomical model containing bones and skinning (but no muscles). DYNA (Pons-Moll et al. 2015) in addition to SCAPE predicts soft-tissue deformations by learning a second-order auto-regressive model based on 40000 scans of 10 subjects.

Data-driven models have become very advanced in recent years. However, in general they can suffer from incomplete input data (due to occlusion) or can be not robust when parameters go far beyond the range the system was trained for. In Visual Effects it is common to have characters performing highly risky actions or movements which are not realistic to acquire and can be very dissimilar from the training set. Moreover there are gaps in the research regarding highly controllable deformation models (at the vertex level).

Machine Learning, and in particular Deep Learning, have been applied recently to the learning of physical models and in particular fluid simulation. Tompson et al. (2016) obtain very convincing results for smoke simulations using a tailored Deep Neural Network operating on a volumetric grid. The system, unsupervised, is trained to approximate the solution of the linear system to compute the pressure equation, minimizing the divergence of the velocity field. Ladický et al. (2015) also use a data-driven approach to learn fluid dynamics but adopt regression forests in a supervised manner for the regression of acceleration of particles at a given time step.

Table 2.1 provides a qualitative comparison of most of the main methods in the literature and puts in evidence their advantages and disadvantages.

Table 2.1: *Comparison of deformable objects methods*

METHOD	**PROs**	**CONs**

Physically - based-methods		
Classic linear FEM (Bonet and Wood 1997)	- easy to implement	- no large deformations - loss of volume
Corotational linear FEM (stiffness warping) (Muller et al. 2003 2004)	- supports large deformations - efficient	- some loss of volume (up to 50%) - inexact force differentials instability
Invertible FEM and extensions (polar SVD) (Irving et al 2004 2007)	- recovers degenerate and inverted tetrahedra - Volume preservation	
FEM for muscle biomechanical simulation (Lee et al. 2009, Teran et al. 2005)	- supports anisotropic materials - transversely isotropic muscle constitutive model - several methods together, including inversion handling	- because of embedding not all details are simulated - high complexity
Finite Volume Method (Teran 2003)	- can be used with any constitutive model - easy to implement	

Efficient elasticity (McAdams et al. 2011)	- quasi-static and dynamics - multigrid solver - self collisions - near interactive - parallel on multicore	- speed - implementation - no near-incompressible materials - complex to understand
Eulerian solids (Levin et al. 2011 2014)	- handles well collisions and contacts - preserves volume - stable for inversions and large deformations - no remeshing needed - relatively easy to implement - GPU	- big matrix to invert - no internal fibers architecture - too many grids so need system to make them collide - no explicit mesh (solved)
Position Based Dynamics (Muller et al. 2007)	- easy to implement - very controllable - positions can be directly manipulated in real time - constraints and collisions are handled quite easily	- less accuracy - result dependent on number of iterations (solved by XPBD)

Lattice deformers (Patterson et al. 2012)	- regular structure optimization - no need for a mesh per muscle - accurate volume preservation with general treatment of incompressibility - quasi-static and dynamics	- some voxelization artifacts are noticeable - complex to understand - no collision treatment (yet) - small scale topology - no direct manipulation of mesh
Procedural / Geometric methods		
Linear Blend skinning (Magnenat-Thalmann et al. 1988)	- fast - no collisions	- loss of volume - candy wrap effect
Dual Quaternion skinning (Kavan et al. 2008)	- fast - no collisions	- bulge at joints
Steklov-Poincare skinning (Gao et al. 2014)	- interactive - physically based - supports collisions - pose dependent, no need to correct indefiniteness of stiffness matrix	- quasistatic only (possible extension) - probably not suitable for deep and strong contacts - not implicit time integration (yet)

Elastic Implicit skinning (Vaillant 2013,2014)	- no skin weights painting - automatic free form operators generation - art directable to mimic muscle activation - seems very stable	- still quite slow for large meshes, depends on timestep choice and efficiency of GPU solver
Shape interpolation (blendshapes) (Lewis et al. 2000)	- fast to calculate	- lot of manual work to generate
Bounded Biharmonic Weights (Jacobson et al. 2011)	- shape awareness and locality - support concave boundaries - automatic weights	- no support for contact (yet)
Elasticity-Inspired Deformers for Character Articulation (Kavan and Sorkine 2012)		
Shape Matching (Muller et al. 2005)	- simple to compute - stable - meshless - memory efficient	- less accuracy - not physically motivated

Mass-springs systems (Nealen et al. 2006)	- easy to implement	- difficult to obtain real materials behaviour, lots of tweaking

What emerges from this analysis of the current state of the art is that to build a good character deformation pipeline, compromises and choices about complexity have to be done. In fact no method is free from drawbacks. Moreover, the advantages of a computational method (solver) have to be coupled by tools that assist the artists in their day to day job and necessarily abstract low-level details. The successful production-ready results presented in this review have all in common exactly this attention to the whole pipeline and to the end user, not only to the computational efficiency. Lastly, often the literature presents new efficient methods on a very specific component of a deformation system, but what is needed is their combination in a common framework. The work presented in this thesis tries to unify different techniques in the same pipeline and also presents solutions for the artists in the form of tools. All these approaches have in common the fact of being physically-based at their core.

The following part of this thesis presents five research projects completed during the period spent at MPC London. The projects are not presented in chronological order, but in a logical way that respects the stages of the pipeline from modelling to simulation.

The videos and supplemental material associated to the projects can be accessed at `http://www.fabioturchet.com/supplemental_material.zip`.

Part II

Projects

Chapter 3

Muscle Modelling

3.1 Introduction

In recent years, physics-based muscle simulation has become increasingly popular in the Animation and Visual Effects industry. Examples of excellent Research and Development from companies which was applied to specific movie productions include the FEM Tissue System at Weta Digital (WETA Digital 2013), PhysBam-based Zeno at ILM (Comer et al. 2015), the PhysGrid-based system at Disney (Milne et al. 2016) and the interactive system for skin sliding at Method Studios based on ADMM and Projective Dynamics (Saito & Yuen 2017). This work takes inspiration also from those results.

The muscle system which is used for these purposes usually contains the following components:

- Anatomically correct muscle geometries;
- A fibre field defined on them;
- A constitutive model supporting fibre activation for contraction;
- A skeleton model on which the muscles attach via constraints;
- A physics solver that computes the dynamics of the system.

This chapter focuses on the first component of the list. In fact one of the most time-consuming steps of a character simulation pipeline is the initial setup of the input model.

Muscle geometries can be generated in various ways: sculpted per-character by trained artists, created from MRI and CAT scan data as in Jacobs et al. (2016), or transferred from an existing template. However, the sculpting process is time-consuming because it requires ad-hoc work for each character, the data scans are not always available and the fitting of templates to new characters presents challenges when dealing with non-humanoid or fantastic creatures which have atypical features, body proportions and body mass distribution. Moreover the result is generally not simulation-ready because of the interpenetrations present in the input meshes, i.e. intersections of various mesh objects representing different muscles.

In this work the complexity of the sculpting process is reduced by introducing methods that allow artists to create volumetric muscle shapes complete with tendons from sketches of muscle silhouettes (patches) defined on the external surface of a character (skin) and attachment points corresponding to the insertion and origin of anatomical muscles on the skeleton. By using an artist-led physically-based simulation framework that includes shape inflation in the direction of the skeleton and muscle-to-muscle and muscle-to-bone collision handling, a user can design plausible volumetric reconstructions. As a result the shape of the muscle and the corresponding fibre field are obtained, both ready for further simulations. The key idea of the system is to exploit the information of the sculpted or scanned skin of a character such as detailed areas (patches) that correspond to superficial muscles and use them to generate plausible volumetric reconstructions which are interpenetration-free. The results obtained show how using these patches can reduce the complexity of the sculpting process, while guaranteeing that output meshes are suitable for simulation.

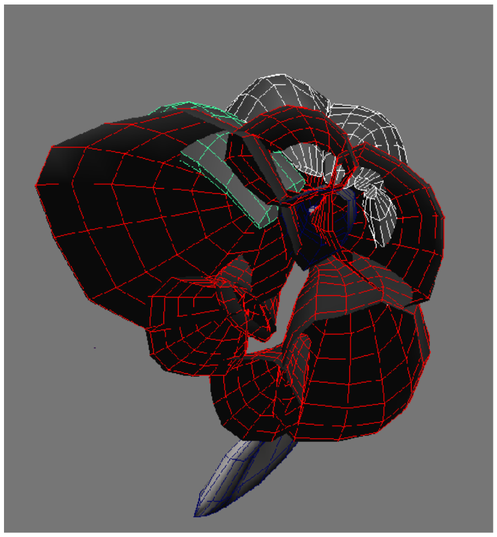

Figure 3.1: *A slice of the arm muscle primitives showing intricate intersections.*

3.1.1 Muscle Primitives fixing

One of the motivations behind research in muscle modelling is that at the beginning of the exploration for solutions at MPC, a very accurate anatomical model was not available. The belief was that fixing the primitives (shown in Figure 2.6) of the existing rigging system would have been enough to create simulation-ready volumes. The intersections severity to be fixed varied from superficial to deep (Figure 3.1).

However, the assumption was not entirely correct as it became very hard or even impossible to fix (i.e. to free from intersections) all the muscles in the general case. The small and medium cases were successfully fixed by converting geometry to signed distance fields and using interactive marching of the vertices in the normal direction, a method similar to implicit skinning described in more detail in chapter 6. An example of successful muscle fixing is shown in Figure 3.2. However for deep intersections, for example when meshes of small muscles were completely inside meshes of other muscles, automatic fixing was not possible.

Another solution to the problem of fixing primitives could be applying physical-based approaches. Geometries could for example be moved apart from each other like in an exploded view and then animated back

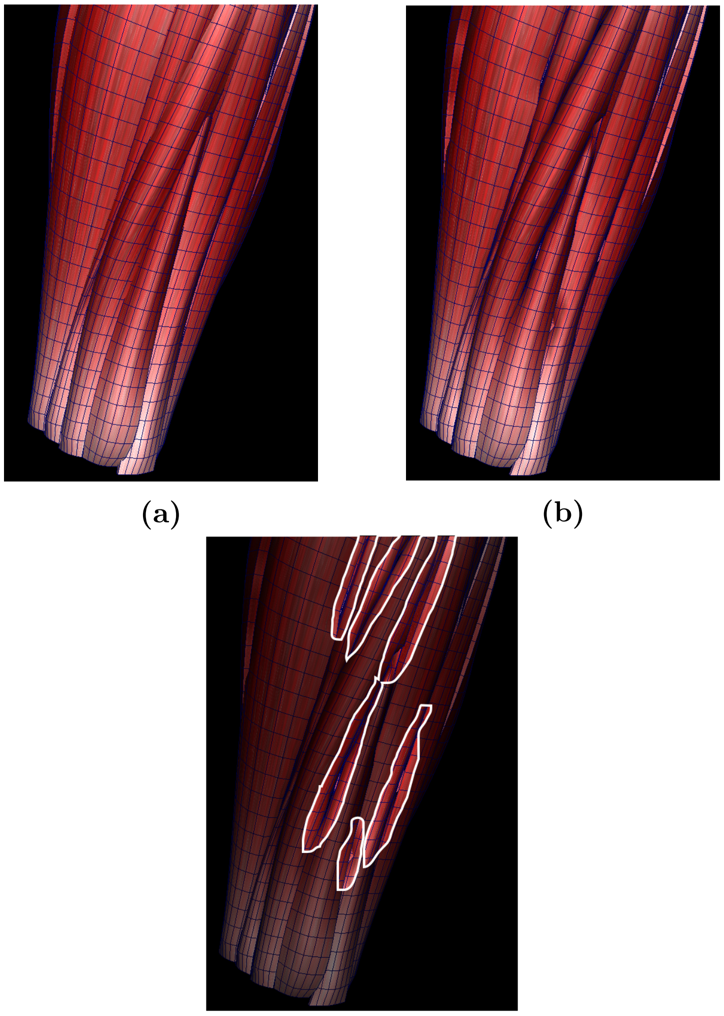
(a) (b) (c)

Figure 3.2: *(a) intersecting geometries of the forearm; (b) solved intersections, (c) highlighted fixed areas.*

to their original positions solving for collisions quasi-statically when they occur. Just like the case of the wrong projections problem in Implicit Skinning solved in Vaillant et al. (2014), the solution would thus emerge by taking advantage of the time variable. It should be noted that the problem of fixing intersecting geometries can be avoided if riggers are provided with tools to model muscles interactively with the help of physics: this chapter explores exactly that direction.

3.2 Related Work

Previous research work containing methods to produce muscle primitives relies mainly on existing anatomical data. Teran et al. (2005a) create tetrahedral meshes from the Visible Human dataset via level sets and are able to reconstruct missing tendon information using Constructive Solid Geometry. More recently, the work by Jacobs et al. (2016) reconstructs very accurate musculature of a full body female subject via segmented cross sectional MRI data for simulation purposes. Saito et al. (2015) instead utilize a commercially available anatomical model and focus on the physics-based modelling of different body shapes by growing or shrinking muscles and fat. In a production setting such as at MPC, because of the complexity of modelling muscles, a popular way to create them is by using either parametric surfaces or procedural primitives controllable with numerous parameters.

The fibre field in Teran et al. (2005a) is obtained with B-spline solids and used to simulate muscle contraction with the Finite Elements Method and a transversely isotropic constitutive model, while the more recent work of Choi & Blemker (2013) focuses on obtaining the fibre field by solving a Laplace equation subject to flux boundary conditions in the tendon regions.
Following the popularity gained by muscle systems in recent years, researchers also started to focus on the problem of transferring anatomical templates between characters. Previous work (Sumner & Popović 2004) focused mainly on registration and deformation transfer of superficial meshes, but not of internal information except for the skeleton. However, the transfer of complex internal anatomical structures require ad-hoc solutions. The works by (Ali-Hamadi et al. 2013) for the body and by (Cong et al. 2015) for the face fill this gap by transferring procedurally complex template models across similar characters, with the possibility of affecting the result with artist input. These solutions speed up character production, but in some cases can produce unwanted deformations when source and target shapes are substantially different. The inspiration for the work in this Chapter came by the field of computational

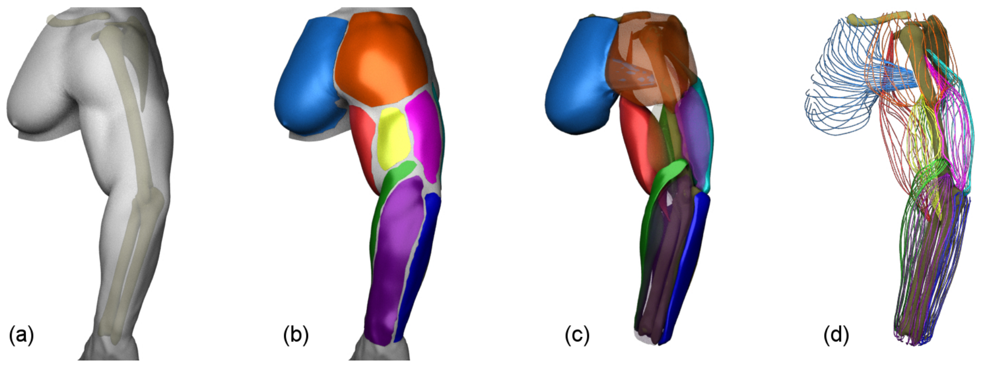

Figure 3.3: *Overview of the pipeline. (a) Input skin mesh and skeleton; (b) sketched patches of superficial muscles; (c) inflated output muscles (opacity used to show underlying structures) ; (d) associated fibres .*

design: the work of Skouras et al. (2012), which computes the rest shape a balloon must have in order to achieve a desired target when inflated, and the work of Skouras et al. (2014), which simulates inflatable structures made of flat panels sketched on a target geometry. These methods are based on physics-based interactive optimization.

3.3 Method

Figure 3.3 illustrates the main steps of the method. The steps are:

1. User sketches patches of superficial muscles
2. Tendons are reconstructed
3. The muscles geometry is created by using fibre curves
4. Patches are extruded and inflated
5. The fibre field is reconstructed

The inputs of the system are a character model, its skeleton geometry, patches to be inflated and tendon attachment points. A patch $\mathcal{P}_i$ is a segmented subset of the input character mesh and follows the silhouette of the visible muscles under the skin. Users can manually segment the outer skin by placing on it nodes of a closed spline curve using their anatomical knowledge and surface details; the enclosed mesh is then cut and extracted (see Fig. 3.3b). For each muscle that a patch represents, attachment points are positions on the input skeleton where its tendons attach (see section 3.3.2). This approach has limitations when the skin of the character doesn't present clear enough anatomical features of the muscles. This happens for example when the adipose tissue (fat) smooths out the details and tends to flatten out the curvature on the skin. In these cases the application of the method is still possible, but does not necessarily produce organic shapes of the muscles. However, the advantage of sketching the input patches from the surface guarantees that there is a clear separation between the muscles at the superficial level, while the internal non-intersection is guaranteed by the tendon creation rules first (collision avoidance), and by the inflating physical simulation later.

3.3.1 Fibre Curves

The initial polygonal patch is dependent on the input skin topology by construction. This means that in general the edges are not following the ideal fibre flow of the patch shape, therefore the simulation can suffer from unaligned and non uniform elements. For this reason the patch is first converted to an intermediate parametric representation for which the topology is controllable. This is achieved by first sketching a series of fibre curves along the desired flow. Specifically, after defining a set of starting points SP and ending points EP on the borders corresponding to where the tendons would attach, a fibre curve fib_j connects a point $sp_j \in SP$ to a corresponding end point $ep_j \in EP$ on the opposite border (see Fig. 3.5 top). This operation can be performed manually (as in this work), or alternatively one can use the method in Choi & Blemker (2013). One of the differences is that in this work the curves are explicitly created, while in their work they need to be traced from a vector field. The advantage of the approach in Choi & Blemker (2013) is that the field is generated automatically. Integrating a similar method to generate the curves fast would be highly beneficial.

The fibre curves, after a resampling step, produce a parametric NURBS

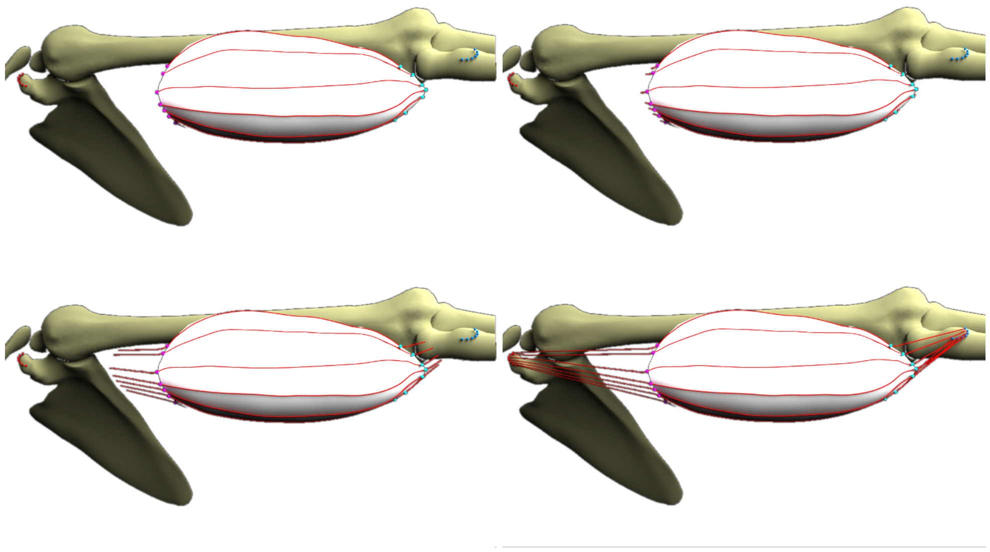

Figure 3.4: *Frames at progressive times of the extension of fibre curves for tendon reconstruction via the use of a flocking system.*

surface through a process of lofting; the result can then be converted back to polygons keeping full control of the resolution. These operations provide a mesh with clean topology and edge flow that follows the fibre directions.

3.3.2 Tendon Reconstruction

The retopologized patches are still missing the tendons that connect the muscle to the bone. This missing geometry is reconstructed by running a sequential flock simulation, using as agents (boids) particles that are positioned at the points of SP/EP and with velocity equal to the tangent of fib_j at those points. Boids have been chosen for their ability to generate smooth curves automatically that follow the edge flow of the mesh and for being able to maintain an offset distance between each other, something important for the following steps of mesh generation. The twisting of the resulting curves depends only on the target positions of the goals, which are editable in case of unwanted twisting.

Boids are subject to the classic rules of cohesion, separation, steering towards target, alignment and collision avoidance as discussed in Reynolds

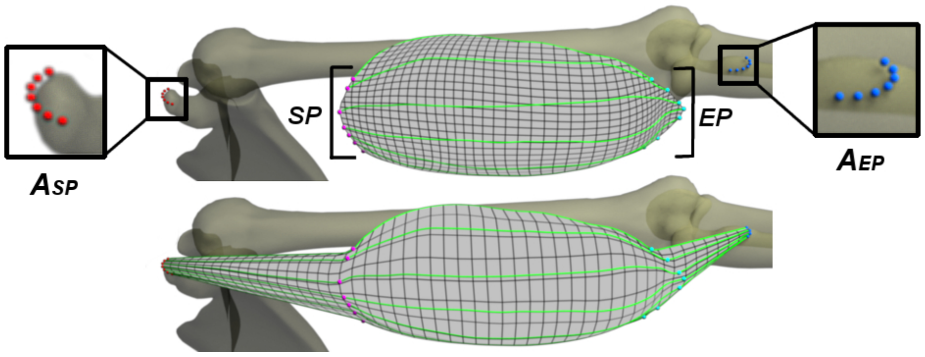

Figure 3.5: *Top: initial bicep patch segmented from the character's skin; initial fibre curves in green; point sets SP and EP in magenta and cyan; target point sets A_{SP} and A_{EP} in red and blue, respectively; bottom: tendon reconstruction via flock simulation.*

(1987). Given target attachment point sets A_{SP} and A_{EP} specified on the skeletal bone geometries as input, the steering rule is responsible for driving the boids starting from sp_j and ep_j towards their corresponding goals (see Fig. 3.4 and 3.5).

These boids define curves that extend the initial input fibre curves in both directions. They can then be lofted and turned into a polygonal surface, as explained in section 3.3.1 to produce the final patch geometry. By varying the weight of the output vectors of the rules, the user has control over the smoothness, curvature and ultimately shape of the geometry connected to the patch. For example, by increasing or decreasing the initial velocity of the boids at the starting points, the attachment to the mesh can be made more or less sharp. The curvature of the tendon is also controlled with the magnitude of the parameter that influences the goal rule: smaller magnitudes produce smoother curves because the boids steer towards the target more slowly in their trajectory. The velocity of the boids can be reduced after entering a minimum distance from the target to produce a better trajectory and therefore shape of the tendon near the bone. Additionally, a collision rule is introduced that prevents tendons from intersecting each other by steering away from other tendons. A boid i checks if its distance from an object is less than a safety

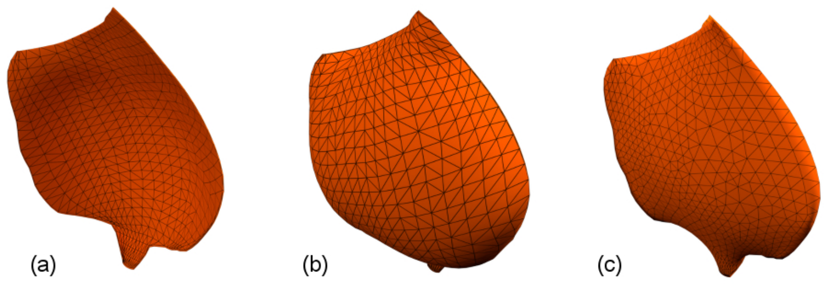

Figure 3.6: *(a) Deltoid extruded patch; (b) inflated muscle; (c) new rest shape after smoothing and relaxation.*

offset d and steers away from it using the vector:

$$\mathbf{steer^i}_{coll} = projTan(\mathbf{n^i}_{closest}, (\mathbf{p}_{bary} - \mathbf{p^i})) - \mathbf{v^i}$$

where $\mathbf{p}_{bary}$ is the barycenter of the rest of the flock, $\mathbf{p^i}$ and $\mathbf{v^i}$ are the current position and velocity of boid i and $projTan$ is a function that returns the tangent component of an input vector given the normal at the closest point on the mesh $\mathbf{n^i_{closest}}$. The magnitude of $\mathbf{steer^i}_{coll}$ is clamped to a maximum allowed value.

3.3.3 Generation of muscles geometry

The initial patches are three-dimensional open manifolds. The next step of the method is to find a way to turn these surfaces into closed meshes obtaining plausible muscle shapes. The patches are, by construction, very close to each other but not intersecting. Therefore the desired rest closed configuration of the patch is forced to be very thin. The approach one can take to create a closed volumetric mesh approximating the shape of a muscle is to use a hole-filling algorithm with fairing (Liepa (2003)), to triangulate the patch hole and then deflate it until it collides with the patch itself. The problem with this approach is that the topology of the filled part is not easily controllable and the triangulation does not respect the desired edge flow.

Instead this method proceeds by extruding the initial patch by a very small controllable offset. By extrusion it is meant that every vertex is moved in the normal direction and the offset controls the distance by which the vertex is moved. Then in a first phase pressure is applied to the extruded vertices and a simulation without collisions is run until full inflation. Using the resulting mesh, a new rest shape is generated by applying alternated Laplacian smoothing iterations and tangential mesh relaxations only on the inflated vertices (see Fig. 3.6). The iterations continue until an initial estimate of the volume is reached. This step is needed so that the resulting mesh is much less likely to create unwanted folds when inflated. In a second phase, the actual simulation with collisions is run in which final muscles are created. At the very start of the simulation, the vertex positions of the initial extruded vertices constitute the initial conditions applied to the rest shape created in the first phase, so there is a non-negative elastic potential.

Inspired by the physics of rubber balloons (Skouras et al. 2012), increasing pressure forces are applied to the nodes of the closed elastic patch, towards the skeleton. During inflation, the vertices of the initial patch with tendons are set fixed as Dirichlet boundary conditions and are not allowed to move in order to obey the user input. In this process deformable meshes collide with other inflating patches and with the rigid skeletal bones (see Fig. 3.7). The inflation continues until a desired volume amount is achieved or until a specified percentage of the total area is in contact.

When inflating, artistic control is important to direct how the shape evolves in time. For this reason artists have full control over the pressure parameters of individual muscles. Even if not implemented, it would be simple to integrate the support for painted spatial pressure weight maps (per vertex) to give even greater control.

3.3.3.1 Elastic Model and Forces

The forces involved in the simulation are the stretching and pressure forces. Inspired by the work of Wang et al. (2011), the rest pose of the inflatable patches is represented in a two dimensional material space computing for each triangle material coordinates of undeformed and de-

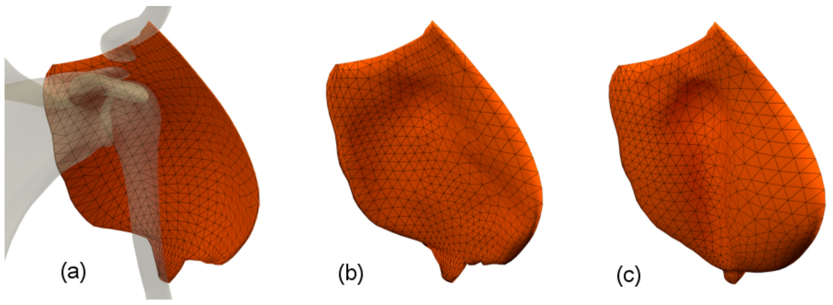

Figure 3.7: *(a) Deltoid extruded patch with collision objects; (b) partial inflation; (c) full inflation.*

formed configurations. In-plane stretching forces are calculated using a simple model for the elastic energy. Given the deformation mapping $\mathbf{x} = \Phi(\overline{\mathbf{x}}) : \Pi \subset \mathbb{R}^2$ describing the deformation of a point $\overline{\mathbf{x}}$ in 2D parametric space with material coordinates (u,v) to a point $\mathbf{x}$ in 3D world space with components (x,y,z), then the deformation gradient is defined as:

$$\frac{\partial \Phi(\overline{x})}{\partial \overline{x}} = \begin{bmatrix} \frac{\partial \Phi_1}{\partial u} & \frac{\partial \Phi_1}{\partial v} \\ \frac{\partial \Phi_2}{\partial u} & \frac{\partial \Phi_2}{\partial v} \\ \frac{\partial \Phi_3}{\partial u} & \frac{\partial \Phi_3}{\partial v} \end{bmatrix}$$

At the initialization stage, 2D material space coordinates are calculated for each element. For a triangle element with nodes in undeformed ($\overline{\mathbf{x}}_1$, $\overline{\mathbf{x}}_2$, $\overline{\mathbf{x}}_3$) and deformed configurations ($\mathbf{x}_1, \mathbf{x}_2, \mathbf{x}_3$) the discretized deformation gradient $\mathbf{F}$ of dimension 3x2 is defined as:

$$\mathbf{F} = \begin{bmatrix} (x_2 - x_1) & (x_3 - x_1) \\ (y_2 - y_1) & (y_3 - y_1) \\ (z_2 - z_1) & (z_3 - z_1) \end{bmatrix} \cdot \begin{bmatrix} (\overline{x}_2 - \overline{x}_1) & (\overline{x}_3 - \overline{x}_1) \\ (\overline{y}_2 - \overline{y}_1) & (\overline{y}_3 - \overline{y}_1) \end{bmatrix}^{-1}$$

From $\mathbf{F}$ the right Cauchy-Green tensor is computed, defined as $\mathbf{C} = \mathbf{F}^T\mathbf{F}$. With it the Green's nonlinear tensor is derived:

$$\mathbf{G} = \frac{1}{2}(\mathbf{C} - \mathbf{I})$$

From Hooke's law, the in-plane stress is calculated using a linear stress-strain relationship:

$$\sigma = \mathbf{B} \cdot \epsilon$$

where $\mathbf{B}$ is a precomputed 3x3 symmetric stiffness tensor that depends on Young's modulus E and Poisson's ratio ν (Müller & Gross 2004) while σ and ϵ are expressed in Voigt form.

Considering that the surface should not present transverse shearing resistance, $\mathbf{B}$ can be simplified from the original 9 parameters to 5 as in Wang et al. (2011).

$$\mathbf{B} = \begin{bmatrix} b_{11} & b_{12} & 0 \\ b_{12} & b_{22} & 0 \\ 0 & 0 & b_{33} \end{bmatrix} = \begin{bmatrix} \frac{E}{1-\nu^2} & \nu\frac{E}{1-\nu^2} & 0 \\ \nu\frac{E}{1-\nu^2} & \frac{E}{1-\nu^2} & 0 \\ 0 & 0 & \frac{E}{1-\nu^2}(\frac{1-\nu}{2}) \end{bmatrix}$$

The elastic potential energy density per triangle can then be defined as:

$$E_e = \int_{V_e} \frac{1}{2}(G : B : G)dv = \frac{1}{2}(G : \sigma) \cdot \overline{A}_e h$$

where $\overline{A}_e$ is the area of the undeformed element, h its thickness and $V_e = h\overline{A}_e$ its volume. The total stretching energy of the deformable patch is obtained by summing up the contributions of all the elements:

$$E_{stretch} = \sum_{i}^{faces} E_e^i$$

Finally, stretching forces and the Hessian (needed for implicit integration) are obtained by analytical derivation solving: $-\nabla_x(E_{stretch})$ and $-\nabla_x(\nabla_x(E_{stretch}))$, respectively.

As described in Skouras et al. (2012), muscles inflate thanks to a discrete nodal pressure force defined as:

$$\mathbf{f}_i = \sum_{j \in \mathbb{N}_i} \frac{1}{3} \cdot p_i \cdot A_j \mathbf{n}_j$$

where $\mathbb{N}_i$ are the neighbouring triangles of vertex i, A_j and $\mathbf{n}_j$ the area and normal of triangle j, and p_i is the base pressure per vertex. In practice, small triangles present in the tendon region result in small pressure forces, which prevent the tendon from fully inflating. Therefore a unit area A_j for all triangles is used. Adapting a topology-independent method such as the one presented in Cong et al. (2015) would be also beneficial. Pressure per-vertex is increased linearly over time. When a node collides, its pressure value is frozen to its last value, in order to improve the solver's stability.

Note that bending forces can be disregarded in the simulation because the progressive pressure increments that define the shape over time cause stretching forces to be very large and the most influential. When inflating, artistic control is important to direct how the shape evolves in time. For this reason artists have full control of the single muscles pressure and material parameters (E and ν) parameters by painting a spatial weight map to create variations in the inflating behaviour.

3.3.4 Fibre Field

Having a volumetric fibre field segmented by muscles is very important for a subsequent physics based simulation of a tetrahedral mesh with an anisotropic constitutive model capable of contraction. Alternatively the muscle geometries themselves can be tetrahedralized and simulated with fibre activations and intercollisions.

One of the advantages of generating the closed patch by extrusion is that the creation of the fibre field of the inflated muscle is greatly simplified. In the method of this work, first the fibre curves are duplicated and translated by the same extrusion offset. Triangle barycentric coordinates are calculated for each control node of the curve so that the inflation deformation can be transferred to the curves. The result is a set of deformed fibre curves that follow the muscle (see Fig. 3.3d). From these curves a three dimensional vector field of fibre directions is generated. It is then stored on a grid that can be interpolated trilinearly inside the volume.

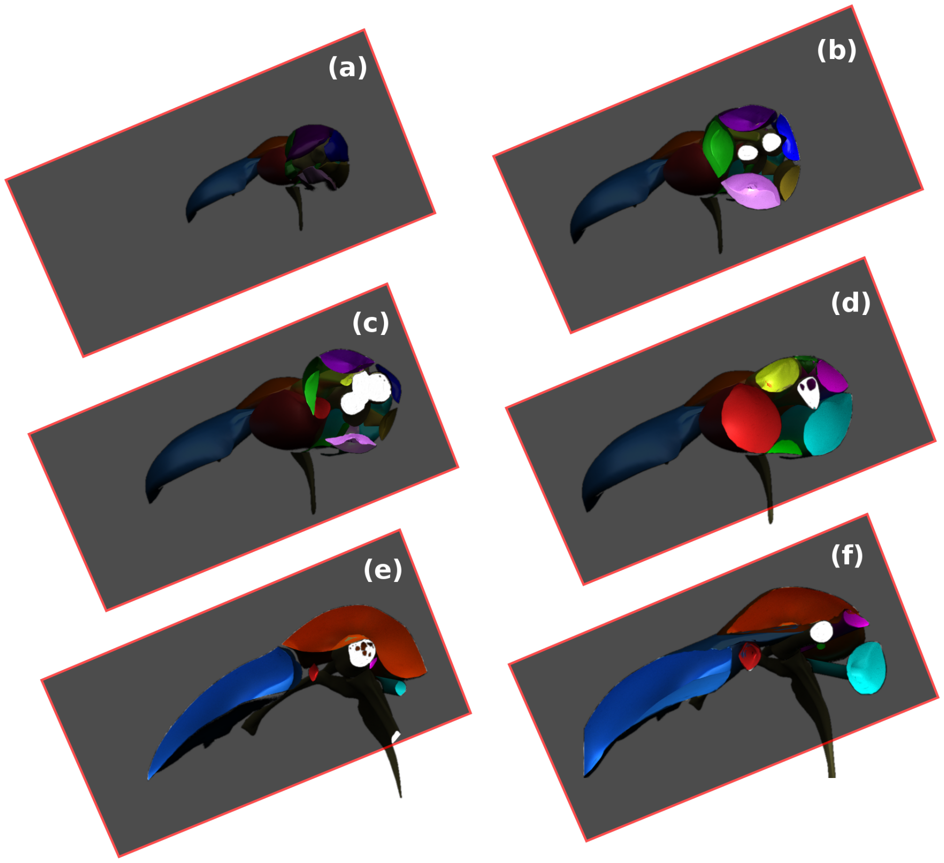

Figure 3.8: *Slices at different depth of the inflated muscles of the arm. Depth of the slicing plane increasing progressively from (a) to (f).*

3.4 Implementation and Results

The physics system is implemented as an Autodesk Maya plugin in C++, while the flocking system is a Python custom tool. The smoothing and relaxation steps of section 3.3.3 utilize standard Maya nodes. All the patches in this paper were generated manually. Experiments have shown that for best results it is useful to maintain a minimum distance between one patch and another so that the subsequent steps do not create intersections in the rest pose. For collision detection and response during inflation the system implements iterative constraint anticipation (Otaduy et al. 2009) with spatial hashing (chapter 4).

As a use case the presented method was tested on a full arm of a muscular human character (see Fig. 3.3). A real arm consists of about 25 muscles; 12 of them were used (including one pectoral muscle) for the simulation as the rest are not superficial or do not contribute substantially to the deformation. Thanks to the constraints represented by the still vertices of the input patches, inflation produces reconstructions that the artist can expect and control. To test performance, for simplicity the arm was split in upper arm (8 muscles) and forearm (7 muscles) and simulated separately (some shared muscles were duplicated for collision purposes). In both cases inflating objects collide with each other and with the 6 rigid bones. Slices of the inflated resulting shapes are shown in Figure 3.8.

The test consists of a 400 frames long simulation computing 1 substep per frame with a small timestep of 0.0005s and additive pressure increase factor of 0.01 per frame. On an Intel Xeon X3470, the non-optimized code runs on a single thread and takes a cumulative time of 904ms and 1222ms per substep for the 12K and 15K elements of forearm and arm respectively. This result can be greatly improved with multi-threading and, if desired, by trading the accuracy provided by a constrained based collision system for a faster approach using penalty forces (see Chapter 4). The validation has been done mainly at the qualitative and visual level, which was found satisfactory for the goals of the project. A more rigorous approach would be to compare the arm mesh simulated under the contraction of the fibres generated from sculpted anatomical muscles from a template, with the mesh simulated thanks to the active fibres obtained with the method in this Chapter. The muscles and associated fibres produced with the method, despite not being fully anatomically correct, present organic shapes that are usable directly for the simulation of the character (for muscle contraction and secondary effects) (see Fig. 3.9 and please refer also to the videos at `http://www.fabioturchet.com/supplemental_material.zip`).

A method has been presented to generate volumetric muscles based on input patches sketched on the surface geometry of a character. The result is the ability to obtain simulation-ready muscle shapes along with fibre fields to be used for further simulations. Having presented a way

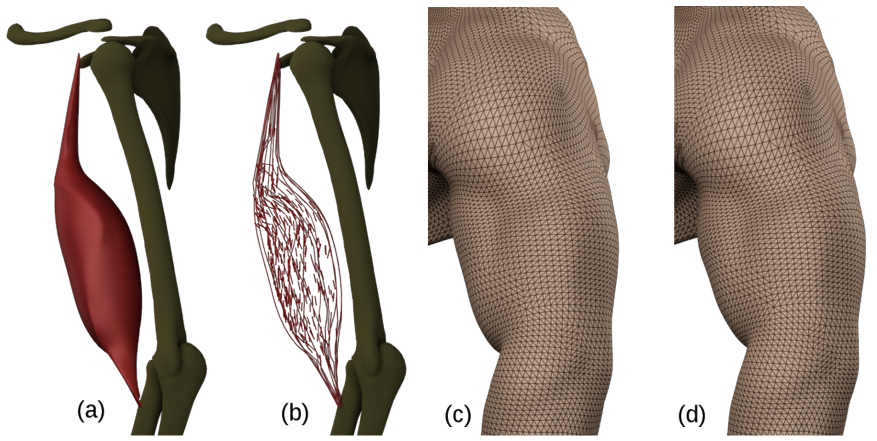

Figure 3.9: *(a) Generated bicep muscle; (b) Fibre curves and interpolated internal fibres; (c) Rest pose mesh; (d) Embedded mesh of deformed pose obtained using a tetrahedral FEM simulation with anisotropic material (isometric contraction).*

to generate anatomical volumetric models, the next chapter describes in detail the structure and theoretical foundations of the solver used to simulate the tetrahedral meshes.

Chapter 4

Musculo-skeletal Simulation

4.1 Introduction

In Visual Effects one of the main requirements for computer-generated creatures and humans is to look realistic, believable and fully integrated in the context and world of the movie. One of the ways to convey this realism is through realistic deformations of muscles, fat and skin.
In this chapter, the methods used to realistically deform anatomical muscle shapes are discussed and, in particular, how fibre-activated materials are integrated in the physics solver. In the first part of the chapter some preliminary exploratory studies with existing technology conducted at MPC will be presented followed by the custom framework that overcomes the limitations encountered will follow.

4.2 Background

This work is based on the idea of applying an engineering approach to character deformation. In an engineering context the Finite Element Method is the most popular choice when simulating complex hyperelastic behaviour of materials. Being in essence a method to find approximate solutions to Partial Differential Equations, its theory has been very well studied for decades.

After considering the various deformable models presented in Chapter 2 and with the desire to obtain plausible and stable results, a Lagrangian representation with standard Finite Elements was chosen. This choice was motivated by:

- The availability of a ready-to-use C++ open-source library for high quality deformable objects called VEGA (Sin et al. (2013a)). Extending it and not coding it from scratch seemed a good idea to speed up the implementation. Containing already classic hyperelastic materials (linear and corotational elasticity, StVk, neo-Hookean, orthotropic), its interface made it quite easy to introduce the anisotropic muscle material presented in section 4.3.3.
- The awareness that at the time of choice, existing interactive / real-time methods were not mature enough, difficult to implement, not accurate or not fully suitable for muscle simulation.
- A wide literature and documentation available on FEM for graphics, including clear mathematical definitions of materials from engineering research.
- The idea of using a top-down approach in the sense of first building a system that is computationally complex but can achieve a desired level of accuracy and progressively simplifying it to get a speed trade-off. In this way it is made available a ground truth which sets the baseline for comparison with later simplifications.

At MPC, FEM was very well known because of the existence of an internal destruction toolkit called Kali for the creation of effects such a disintegration, fracturing and demolitions. Kali is an API built on top of Pixelux's Digital Molecular Matter (DMM) (Parker & O'Brien 2009) and provides the artist with a set of tools and scripts to integrate DMM into the FX pipeline to do mainly shots involving destructions, explosions, fracturing and erosion.

However it soon became apparent, as detailed below, that Kali only matches some of the requirements for muscle simulation and it was therefore discarded for the project. The limitation was not posed by FEM itself, but rather by the lack of an adequate constitutive material model to obtain volume-preserving active contractions of the deformable objects that represent muscles.

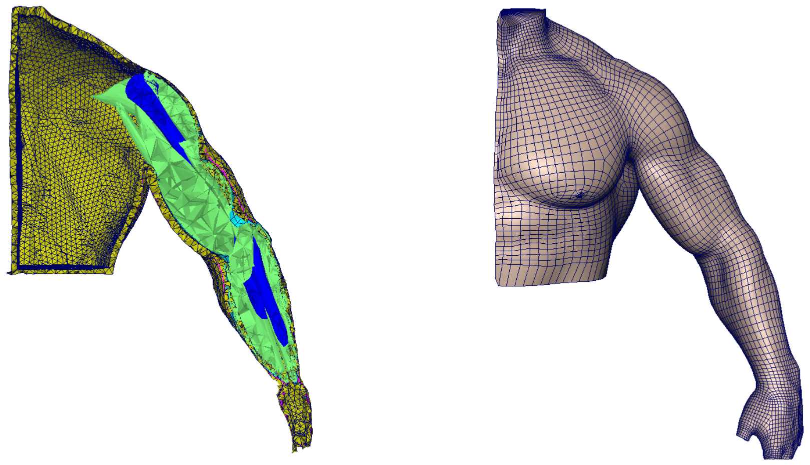
(a) **(b)**

Figure 4.1: *(a) Slice of the full volumetric model; (b) Renderable skin*

The tests described below were performed using existing technology at MPC (i.e. Kali) to expose the necessity of research and development on the flesh material and on the interaction of the different anatomical layers. The goal of the following list of tests was in fact to prove that what is achievable with the current simulation toolset at MPC is not sufficient to achieve the desired quality of deformation. For simplicity the focus has been put only on one part of the body, in particular the left arm of a muscular male such as the one of a bodybuilder (Figure 4.1). At the beginning of this process the muscle primitives of the existing procedural system were fixed from all the intersections both with each other and with the outer skin. Various amendments to the anatomy, which in some cases was lacking accuracy at distal and proximal tendon insertions, also had to be made. These changes were needed because in the rest pose muscles should not have interpenetrations even if they are in tight contact, otherwise the solver would start the simulation by resolving those collisions, thus introducing spurious forces.

4.2.1 Test 1: current MPC's muscle system

In order to have comparable results, a simple animation of an arm lifting followed by a forearm flexion was initially created and used for all the tests. This involved the animation of an existing rig of a muscular body type character which is made of procedural muscle primitives and a fascia geometry shrinked and projected onto the muscles to take their shape (Figure 4.2a). The results were generated with and without dynamics using the existing muscle system without any blend shape activated. In this system, the renderable skin is wrapped barycentrically directly to the muscles.

4.2.2 Test 2: only fat layer

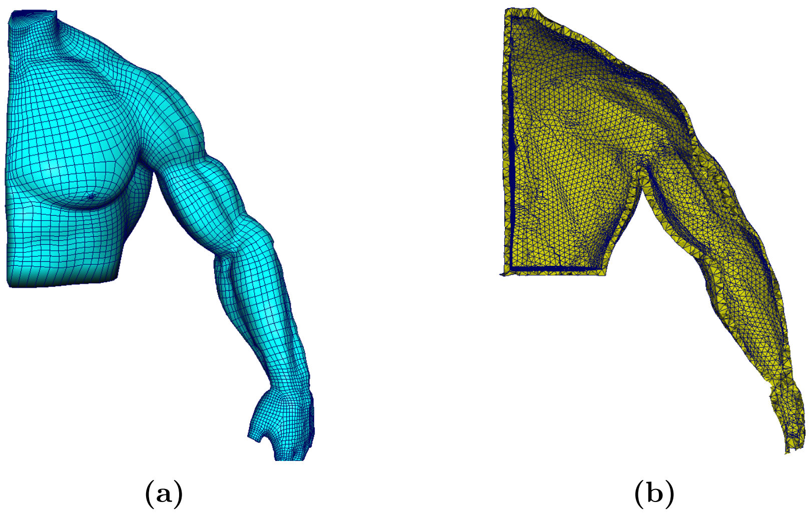

Figure 4.2: *(a) Shrunk fascia; (b) fat volumetric layer*

For the next and following tests the Kali toolkit was used. In the first test with Kali, the attempt was to simulate the fat layer.
The fat is created by tetrahedralization of the offset between the fascia geometry and the skin geometry. The fascia is then deformed with linear blend skinning, cached for efficiency, and acts as a Kali driver for the fat layer. A driver is a polygonal object in Kali that has a falloff radius of influence on nearby tets. The fat layer simulated this way shows self collisions at work and convincing dynamics.

4.2.3 Test 3: simulated passive muscles

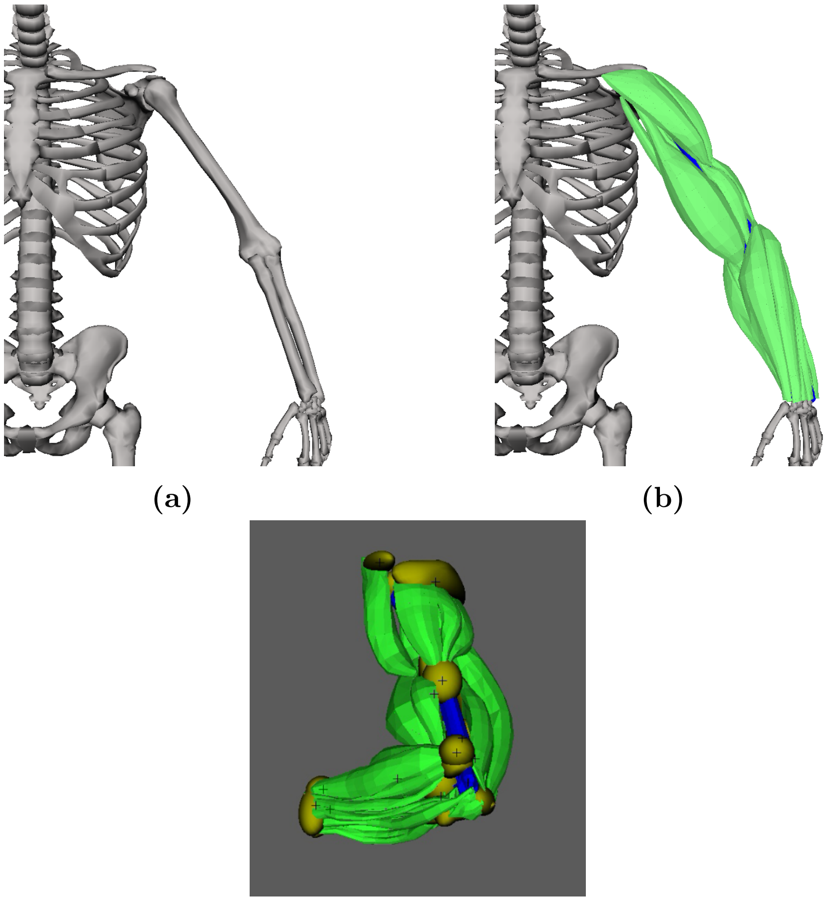
(a) **(b)** **(c)**

Figure 4.3: *(a) Skeleton ; (b) Attached muscles; (c) Muscle deformation*

In this test each muscle primitive was first tetrahedralized, detaching their connections from the procedural system to keep only the geometry. Then these muscles were constrained at their extremities through drivers (the attachment points corresponding to the tendons) and fed into the solver. The result is a set of deformable wobbly objects colliding with each other but not really expressing the characteristics of muscles (Figure 4.3). The simulation was then transferred directly to the outer skin layer with a wrap deformer.

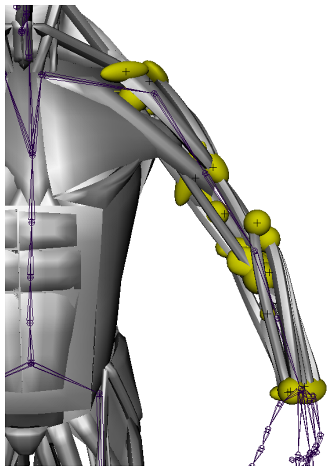

(a)

Figure 4.4: *(a) Line muscles with driving sphere volumes for attachment (in yellow)*

4.2.4 Test 4: simulated “active” muscles

The next test used the same setup as in the previous one, described in 4.2.3. The main difference is that for muscles internal drivers were added which are animated geometries to which the surrounding mesh is attached barycentrically. However, the implementation of a fibre constitutive model was not possible because of Kali being a closed-source product. Therefore an internal activation was attempted by procedurally shrinking the existing muscle primitives to very thin cylinders (Figure 4.4) and using those as drivers with very small falloff. This approach gave promising but not fully satisfying results: the effect of contraction was visible on the flesh, but limited only to the deep vertices in contact with the driver and transferred via inertia to the superficial ones which remained de facto passive.

4.2.5 Test 5: fascia driven by ”active” muscles and fat layer driven by fascia

As final test (Figure 4.5), test 4 was extended with the fat layer, by first simulating the muscles, then wrapping the fascia to them and finally using it as driver for the fat like in test 2. In this and previous tests, the

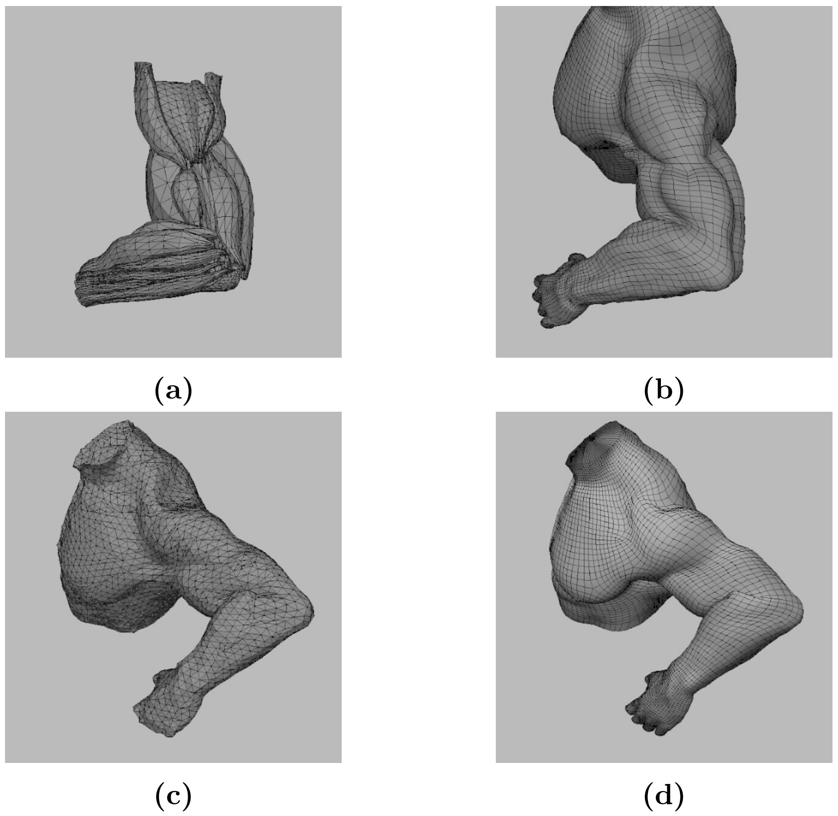

Figure 4.5: *Deformation of (a) Muscles; (b) Fascia; (c) Fat; (d) Renderable skin*

bones are tetrahedralized as well and treated as rigid bodies. This setup produced the most realistic results.

4.2.6 Analysis of the tests

What emerged from all these experiments was in part expected. First of all it is clear that muscles cannot be simulated with just position constraints and an isotropic material. They need a fibre-embedded directional material model to behave realistically. In addition to this basic requirement, the results obtained are convincing in terms of dynamics and shape: separating the jiggle of the muscles from the jiggle of the fat seems to give more realism and also the self collisions seem to add a lot to the flesh look of the arm. The ulna colliding with the skin gives a nice shape to the elbow (Figure 4.5d).

It became apparent that not only is a good anatomical model with properly placed constraints essential, but also that biomechanical requirements should be formalized and implemented carefully. For example, the radius/ulna rotation should be treated carefully to avoid problems during pronation and supination such as artifacts on the final renderable skin. Problems due to the initial rest shape also appeared in the example with the brachialis muscle in which the model was provided as two disjoined mesh objects. As a consequence, during forearm flexion and extension its geometry created a depression on the skin.

One of the limitations of these tests is that a different stiffer material was not assigned to the part of the geometry belonging to tendons. The examples clearly demonstrate the need for a more advanced system that supports features such as: sliding of the components under the fascia and the skin, activations, multiple constraints types, fascia simulation. Tests also show the fact that it is necessary to create the connective tissue constraints between muscles to keep them together during ballistic motion. Muscles in fact should behave as a whole during high-inertia animations such as jumps.

4.3 Solver and Material Models

The approach taken aims at achieving high levels of realism by simulating ordered layers of biological tissues, from the inside to the outside, so that the interesting looking nonlinearities that result from their interaction can be captured. This means that the simulation will be split in different stages, each one outputting an intermediate product of the final result (layers). This makes the system modular and more controllable, but at the same time makes the coupling of the forces more difficult to achieve.

4.3.1 Simulation Model Construction

In order to test the hypothesis that anatomy-based character simulation is a potentially beneficial technique to be adopted by the company, a working prototype is needed. The aim of the prototype is also to find the weaknesses and the possible points of improvement from a practical point of view. This process begins by choosing the musculo-skeletal model to be simulated. Even though there are commercially available solutions such as Zygote (Zygote 2016), for the use case scenario of interest the choice goes to the model of an arm (CGCircuit 2016) obtained by retopologizing scans from a database of real muscles complete with tendons (see Fig. 4.6). The models therefore are very accurate and the mesh clean. Skeleton geometry is obtained in the same way. The model consists of 4 bones and 14 muscles. It is important to have a mesh with regular polygons to facilitate the subsequent generation of regular tetrahedra out of them and improve the collision response accuracy. As shown in the previous section, the option of converting the procedural muscle primitives used in the rigging department was excluded because the shape was is not anatomically accurate enough. For simplicity some of the muscles were merged in bigger groups easier to handle, but still keeping the superficial details. In particular this was done for some of the many thin adjacent muscles of the forearm such as extensors and flexors which are approximated to be working together (see section 4.4.2). Fewer muscles also mean fewer computations for a collision system and fewer constraints between them. Therefore the decision taken is to trade-off the accuracy of interaction of muscles for speedup. These triangle meshes are then converted into a volumetric tetrahedral representation using internal tools available from the Kali toolset which allow the control of various aspects of the tetrahedralization: number of elements, conformity, custom density via weight maps.

4.3.2 Solver

The solver is the core part of any simulation system. On it directly depend desirable qualities such as speed, accuracy of the output, stability of the simulation. In the context of this thesis it has to integrate a partial differential equation (PDE) expression of Newton's second law, commonly known in continuum mechanics as the Cauchy momentum

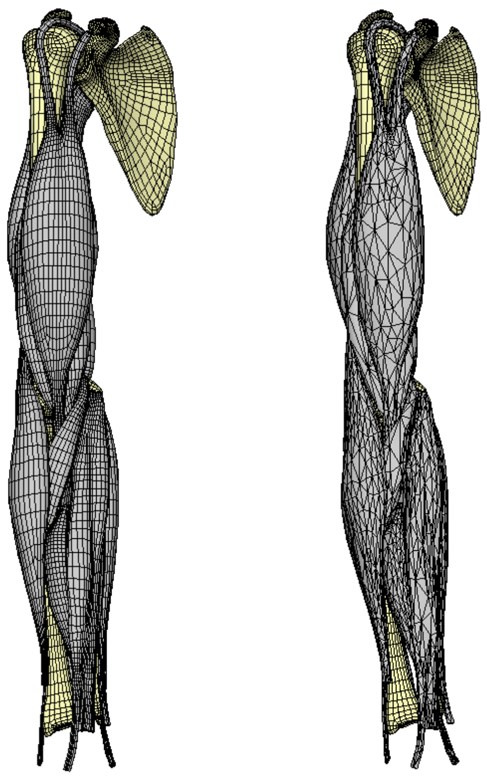

Figure 4.6: *Anatomical geometry for prototype testing. On the left the renderable/embedded mesh from which its conforming volumetric counterpart is generated (right).*

equation which relates the acceleration of a point in a medium with the forces it receives from the surrounding material:

$$\rho \frac{dv(\mathbf{X})}{dt} = \nabla \cdot \sigma + \rho \mathbf{b}$$

where ρ represents the density of the material, $v(X)$ the velocity of a material particle in the object, σ the Cauchy stress distribution (force associated with the deformation of the object) and $\mathbf{b}$ the body forces (gravity, collision response etc).

When testing a solver, it is common in the literature (McAdams et al. 2011) to first study the physics of deformable objects in a quasistatic setting, meaning finding the configuration that brings in equilibrium the forces of the system excluding gravity and inertial effects. By equilibrium it is implied that the sum of all the forces equals zero. This is the approach also followed in this work for the deformation of muscles, while dynamics are introduced in a second stage.

In this work objects (meshes) are intended to be defined as a connected collection of nodes and elements. The nodes are the points for which positions and velocities need to be calculated given the current inertial motion of the object, its material and the presence of external forces. In the Finite Element Method and elasticity theory, objects are first discretized into surface (triangles) or volumetric (tetrahedra) elements on which physical properties such as forces are defined and calculated. In a second stage the method takes the contributions of each element and assembles them in a global system matrix that expresses the accumulation of the elastic forces on each node, shared by multiple elements. A deformation can be formalized at each material point of an object as a function that maps a point in material space $\mathbf{x} \in R^3$ to a point in world space $\mathbf{X} \in R^3$:

$$\begin{aligned}&\mathbf{\Phi} : \mathbf{\Omega} \rightarrow \mathbf{R^3}\\&\mathbf{x} = \mathbf{\Phi}(\mathbf{X})\end{aligned}$$

As mentioned before, a deformation metric has to be chosen. The basic deformation quantifier is the deformation gradient $\mathbf{F}$, a 3x3 matrix defined as the Jacobian of the deformation function:

$$\mathbf{F_{ij}} = \partial \mathbf{\Phi_i} / \partial \mathbf{X_j} \tag{4.1}$$

In practice other metrics dependent on F are used such as Green's strain E (used in this work) which, despite being more computational expensive, is independent of the rotation of the element:

$$\mathbf{E} = \frac{\mathbf{1}}{\mathbf{2}}(\mathbf{F^T F} - \mathbf{I}) \tag{4.2}$$

Knowing the severity of deformation is just one of the ingredients needed to define the physics of deformable objects.

Using $\mathbf{E}$ it is in fact possible to define a material model that expresses the relationship between stress and strain and captures the elastic energy accumulated in a deformed state at a certain time. At a mathematical level a material is an energy density function $\boldsymbol{\Psi}$ that represents the elastic energy of an element. The total elastic energy in a continuous setting is just the integral over the elements of this density function:

$$\mathbf{W_{tot}} = \int_{\omega} \boldsymbol{\Psi}(\mathbf{X}, \mathbf{F}(\mathbf{X}))\mathbf{dX}$$

A real world example of such a function is the one for St. Venant-Kirchoff materials:

$$\boldsymbol{\Psi}(\mathbf{F}) = \mu\mathbf{E} : \mathbf{E} + \lambda\mathbf{tr^2}(\mathbf{E}) \tag{4.3}$$

where μ and λ are the Lame' coefficients which are related to standard material properties used in continuum mechanics such as Young's Modulus Y (measure of stretch resistance) and Poisson ratio ν (measure of incompressibility):

$$\mu = \frac{Y}{2(1+\nu)}$$
$$\lambda = \frac{Y\nu}{(1+\nu)(1-2\nu)}$$

The strain tensor is a quantity that measures the amount of normalized displacement with respect to a rest configuration. It can also be seen as expressing how much the deformation gradient F differs from the identity:

$$\epsilon = \frac{\partial(\mathbf{x} - \mathbf{X})}{\partial\mathbf{X}} = \mathbf{F} - \mathbf{I}$$

The (Cauchy) stress tensor instead is a quantity that expresses how much force f acts on a cross sectional surface area of a solid and depends on the direction of the surface:

$$\sigma \cdot \tilde{\mathbf{n}} = \tilde{\mathbf{f}}$$

It can also be thought as the sum of two components: a mean (or dilational) tensor (responsible for volume changes) and a deviatoric tensor which is actually responsible for distortion and deformation.

In material science literature the properties of a material subject to increasing loading are often visualized through a strain/stress plot that describes the relation of deformation to accumulated stress for a material constitutive model.

After applying FEM theory to the equation of motion (Eq. 2.1), expressing it in terms of positions (displacements) and adding a velocity damping term it becomes:

$$\mathbf{M\ddot{q}} + \mathbf{D\dot{q}} + \mathbf{f_{int}}(\mathbf{q}) = \mathbf{f_{ext}}$$

where $q \in \mathbb{R}^{3m}$ are the displacements of the m mesh vertices from the rest configuration, $\mathbf{D} = \alpha\mathbf{M} + \beta\mathbf{K}(\mathbf{q}) + \bar{\mathbf{D}}$ is the damping matrix, $\mathbf{f_{int}}$ represents the internal elastic forces (gradient of the elastic energy) and its gradient with respect to $\mathbf{u}$, $\mathbf{K}$, is the tangent stiffness matrix.

In order to timestep this equation, in VEGA the Implicit Backward Euler integration scheme is adopted, in its semi-implicit form (Baraff & Witkin 1998):

$$\begin{aligned} \mathbf{q_{n+1}} &= \mathbf{q_n} + \mathbf{hv_{n+1}} \\ \mathbf{v_{n+1}} &= \mathbf{v_n} + \mathbf{hM^{-1}}(\mathbf{f_{ext}} - \mathbf{f_{int}}(\mathbf{q_{n+1}}) - \mathbf{Dv_{n+1}}) \end{aligned} \tag{4.4}$$

By linearizing the nonlinear f_{int} via Taylor expansion:

$$\mathbf{f_{int}}(\mathbf{q_{n+1}}) = \mathbf{f_{int}}(\mathbf{q_n}) + \mathbf{K}(\mathbf{q_{n+1}} - \mathbf{q_n})$$

The equation becomes linear:

$$(\mathbf{M} + \mathbf{hD} = \mathbf{h^2K})(\mathbf{v_{n+1}} - \mathbf{v_n}) = \mathbf{h}(\mathbf{f_{ext}} - \mathbf{f_{int}}(\mathbf{q_n}) - \mathbf{Dv_n} - \mathbf{hKv_n})$$

By knowing the stress that an element undergoes, it is possible to compute the internal forces acting on it. In VEGA this is done by using the first Piola-Kirchoff stress tensor $\mathbf{P}$ defined as:

$$\mathbf{P}(\mathbf{F}) = \partial\mathbf{\Psi}(\mathbf{F})/\partial\mathbf{F}$$

Once $\mathbf{P}(\mathbf{F})$ is computed, the force on a vertex of a tetrahedron is obtained by multiplying $\mathbf{P}(\mathbf{F})$ with its area-weighted normal:

$$\mathbf{G} = \mathbf{P}\mathbf{B_m} \tag{4.5}$$

where $\mathbf{G}$ is the matrix having the forces acting on each vertex of a tetrahedron and $\mathbf{B_m}$ is the matrix having as vectors the area-weighted normals (Irving et al. 2004).

Therefore, in order for the method to work, for each element the stiffness matrix $\mathbf{K}$ has to be computed. $\mathbf{K}$ is defined as the gradient of the internal forces, but in practice its implementation makes use of $\mathbf{P}$ (Sin et al. 2011):

$$\mathbf{K} = \frac{\partial\mathbf{G}}{\partial\mathbf{q}} = \frac{\partial\mathbf{G}}{\partial\mathbf{F}}\frac{\partial\mathbf{F}}{\partial\mathbf{q}} = (\frac{\partial\mathbf{P}}{\partial\mathbf{F}}\mathbf{B_m})\frac{\partial\mathbf{F}}{\partial\mathbf{q}}$$

Details on the derivations can be found in Sifakis & Barbic (2012).

In production, it is highly desirable to give technical artists a fast initial approximation of the results they will get so that they can do more iterations of creative work. To this purpose the solver should support mechanisms to trade-off speed for accuracy and be consistent in relation to sub-frames and resolution variation.

One of the standard techniques adopted in this work to achieve this and to reduce the computation time is called mesh embedding, in which the momentum equation is not solved on all the nodes of a high-resolution mesh, but on a coarse version of the same. The final, renderable mesh is then deformed from this low-res version using barycentric coordinates. Moreover, it is possible to reduce the number of elements (tetrahedra) of the volume by allowing one tetrahedron to share different materials. This approach, not implemented in this work, is used in (Saito et al. 2015) where the quantities of each material are calculated with Monte-

Carlo integration. Another practical solution would be to integrate into the rig blend shapes obtained with simulation.

4.3.3 Constitutive Material Model

Given their structure and specific properties typical of most biological tissue, muscles have been described by an incompressible, transversely isotropic, hyperelastic material. Transversely isotropic means that its physical properties are symmetric with respect to an axis which is perpendicular to an isotropy plane (see Figure 4.7): the properties are the same on the same plane in all directions.

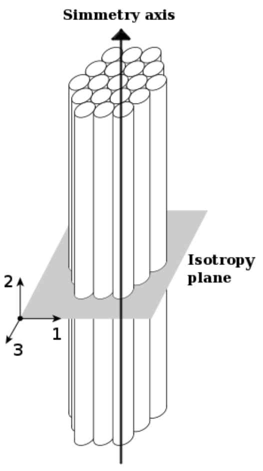

Figure 4.7: *Transverse isotropy*

One of the materials for muscles found in the literature (Teran et al. 2003) and implemented in this work has an uncoupled energy form, separating the material response due to isotropic passive connective tissue and to active components:

$$\mathbf{W}(\mathbf{I_1}, \mathbf{I_2}, \lambda, \mathbf{a_0}, \alpha) = \mathbf{F_1}(\mathbf{I_1}, \mathbf{I_2}) + \mathbf{U}(\mathbf{J}) + \mathbf{F_2}(\lambda, \alpha) \tag{4.6}$$

where:

- $\mathbf{C} = \mathbf{J}^{-\frac{2}{3}}\mathbf{F}^{\mathbf{T}}\mathbf{F}$ is the right Cauchy-Green deformation tensor

- $\mathbf{I_1} = tr(\mathbf{C})$ is the deviatoric (non-volumetric) invariant of the strain
- $\mathbf{I_2} = \frac{1}{2}((tr(\mathbf{C}))^2 - tr((\mathbf{C^2})))$ is the isotropic invariant of the strain (does not vary in magnitude when measured in different directions). An invariant is the same for different orientations of the coordinate system chosen)
- $\lambda =\sqrt{\mathbf{a_0} \cdot \mathbf{C}\mathbf{a_0}}$: a strain invariant associated with transverse isotropy. Transverse isotropy indicates that physical properties are approximately the same along a plane (it equals the deviatoric stretch along the fibre direction)
- $\mathbf{a_0}$ is the fibre direction vector that doesn't depend on F
- α represents the level of activation in the tissue
- $\mathbf{F_1}$ is a Mooney-Rivlin rubber-like model that encapsulates the behaviour of the isotropic tissues in muscle that embed the fascicles and fibres. In this work the StVk model is used instead
- $\mathbf{J} = det(\mathbf{F})$ is the measure of relative volumetric deformation of the element.
- $\mathbf{U}(\mathbf{J})$ is a term expressing incompressibility
- $\mathbf{F_2}$ is the active and passive muscle fibre response. It depends on a_0, the deviatoric stretch in the along-fibre direction λ, the nonlinear stress-stretch relationship in muscle and α.

This material is popular in muscle simulation literature and is intended to capture the force-length nonlinear relationship obtained experimentally from the study of individual fibre response (Teran et al. 2003) (Figure 4.8)

In this work, it is assumed that the stress P and the stiffness matrix K are composed of isotropic and anisotropic summable parts:

$$\mathbf{P} = \mathbf{P_{iso}} + \mathbf{P_{aniso}}$$
$$\mathbf{K} = \mathbf{K_{iso}} + \mathbf{K_{aniso}}$$

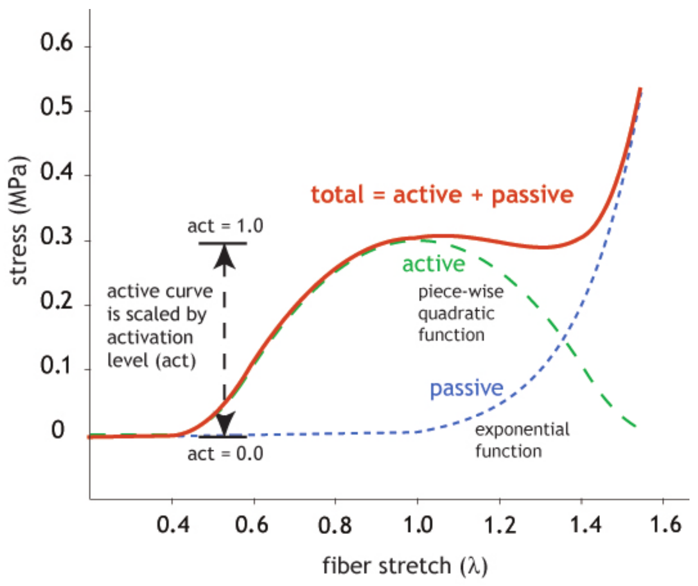

Figure 4.8: *Material response of muscle fibre (active), tendons (passive) and their combination. (Teran et al. 2003)*

In order to compute the first Piola-Kirchoff stress, the energy in equation 4.6 must be derived with respect to $\mathbf{F}$ once to get $\mathbf{P}$ and a second time to get $\frac{\partial P}{\partial F}$. Below some of the steps of the derivation are presented (for the full derivation please refer to appendix D).

Derivation of the anisotropic part $\mathbf{F_2}(\lambda, \alpha)$ is done applying the chain rule and considering the λ variable as just another independent variable to derive:

$$\frac{\partial \mathbf{F_2}(\lambda, \alpha)}{\partial \mathbf{F}} = \frac{\partial \mathbf{F_2}(\lambda, \alpha)}{\partial \lambda} \frac{\partial \lambda}{\partial \mathbf{F}} \tag{4.7}$$

The rightmost term can be developed as:

$$\frac{\partial \lambda}{\partial \mathbf{F}} = \frac{\partial \sqrt{\mathbf{a_0} \cdot \mathbf{C} \mathbf{a_0}}}{\partial \mathbf{F}} = \frac{\partial \sqrt{\mathbf{a_0} \cdot \mathbf{J}^{\frac{-2}{3}} \mathbf{F^T} \mathbf{F} \mathbf{a_0}}}{\partial \mathbf{F}} =$$
$$= \frac{1}{2\lambda}[\frac{-2}{3} det(\mathbf{F})^{\frac{-2}{3}} (\mathbf{F^{-T}}) tr((\mathbf{Fa})(\mathbf{Fa})^{\mathbf{T}}) + 2 det(\mathbf{F})^{\frac{-2}{3}} \mathbf{F}(\mathbf{aa^T})]$$
$$= \frac{\mathbf{J}^{\frac{-2}{3}}}{2\lambda}[\frac{-2}{3}(\mathbf{F^{-T}}) tr((\mathbf{Fa})(\mathbf{Fa})^{\mathbf{T}}) + 2\mathbf{F}(\mathbf{aa^T})] =$$

$$= \frac{\mathbf{J}^{\frac{-2}{3}}}{\lambda}[\frac{-1}{3}(\mathbf{F}^{-\mathbf{T}})tr((\mathbf{Fa})(\mathbf{Fa})^{\mathbf{T}}) + \mathbf{F}(\mathbf{aa}^{\mathbf{T}})] \tag{4.8}$$

The anisotropic term $\mathbf{F_2}$ is defined in Blemker et al. (2005) as

$$\mathbf{F_2}(\lambda, \alpha) = \alpha \mathbf{F_{active}}(\lambda) + \mathbf{F_{passive}}(\lambda)$$

where $\mathbf{F_{active}}$ and $\mathbf{F_{passive}}$ are defined as a piecewise combination of simple linear and exponential functions, therefore it's enough to take their analytical derivatives.

In order to support invertible elements recovery (Irving et al. 2004), the diagonalized version of $\mathbf{F}$ is $\mathbf{F} = \mathbf{U}\hat{\mathbf{F}}\mathbf{V}^{\mathbf{T}}$ which allows carrying out substitutions in the formula:

$$\begin{aligned} &\mathbf{F} \Rightarrow \hat{\mathbf{F}} \\ &\hat{\mathbf{F}}^{\mathbf{T}} = \hat{\mathbf{F}} \\ &\mathbf{a_0} = \mathbf{V}^{\mathbf{T}}\mathbf{a_0} \end{aligned}$$

The last line is needed to rotate the anisotropic terms using $\mathbf{V}$, as suggested in Irving et al. (2004), so that the final formula becomes:

$$\mathbf{P_{aniso}} = \frac{\partial \mathbf{F_2}(\lambda, \alpha)}{\partial \mathbf{F}} = \frac{\partial \mathbf{F_2}(\lambda, \alpha)}{\partial \lambda}\left(\frac{1}{2\lambda}\mathbf{V}^{\mathbf{T}}\mathbf{a_0} \cdot 2(-\frac{1}{3}\mathbf{J}^2\hat{\mathbf{F}} + \mathbf{J}^{-\frac{2}{3}}\hat{\mathbf{F}}\mathbf{Ones})\mathbf{V}^{\mathbf{T}}\mathbf{a_0}\right) \tag{4.9}$$

with

$$\begin{aligned} \lambda &= \sqrt{\mathbf{V}^{\mathbf{T}}\mathbf{a_0} \cdot \mathbf{J}^{\frac{-2}{3}}\hat{\mathbf{F}}^{\mathbf{2}}\mathbf{V}^{\mathbf{T}}\mathbf{a_0}} \\ J &= det(\hat{\mathbf{F}}) \end{aligned}$$

In order to compute the anisotropic part of the stiffness matrix, P has to be derived a second time yielding the formula (using Einstein's notation):

$$
\begin{aligned}
\frac{\partial \mathbf{P_{aniso}}}{\partial \mathbf{F}} = &-\frac{2}{9}J^{\frac{-2}{3}}(\mathbf{F^{-T}})_{ij}(\mathbf{a_0}\cdot \mathbf{J}^{\frac{-2}{3}}\mathbf{F^TFa_0})_{lm}^{\frac{-1}{2}}(\mathbf{F^{-T}})_{ij}(\mathbf{Fa})_k(\mathbf{Fa})_k \\
&-\frac{2}{3}\mathbf{J}^{\frac{-2}{3}}(\mathbf{F^{-T}})_{ij}(\mathbf{a_0}\cdot \mathbf{J}^{\frac{-2}{3}}\mathbf{F^TFa_0})_{lm}^{\frac{-1}{2}}(\mathbf{Fa})_i\mathbf{a}_j
\end{aligned}
\tag{4.10}
$$

The incompressibility term of the energy is defined in Teran et al. (2003) as:

$$\mathbf{U}(\mathbf{J}) = K\ln(\mathbf{J})^2$$

and its derivative becomes:

$$\frac{\partial \mathbf{U}(\mathbf{J})}{\partial \hat{\mathbf{F}}} = \frac{\partial \mathbf{U}(\mathbf{J})}{\partial \mathbf{J}}\frac{\partial \mathbf{J}}{\partial \hat{\mathbf{F}}} = \frac{2K\ln(\mathbf{J})}{\mathbf{J}}det(\hat{\mathbf{F}})\hat{\mathbf{F}}^{-\mathbf{T}} = 2K\ln(det(\hat{\mathbf{F}}))\hat{\mathbf{F}}^{-\mathbf{1}}$$

However, in this work the incompressibility term $\mathbf{U}(\mathbf{J})$ is already incorporated in term $\mathbf{F_1}$ which is in fact represented by an isotropic StVK material. Expressions for $\partial\mathbf{P_{iso}}/\partial\mathbf{F}$ are implemented in VEGA, but not in their analytical efficient form. Therefore the formulation was derived by hand (shown below). Full derivation is given in appendix C.

$$\mathbf{P_{iso}} = \mathbf{P}(\mathbf{F}) = \mathbf{F}[2\mu\mathbf{E} + \lambda tr(\mathbf{E})\mathbf{I}] \tag{4.11}$$

$$
\begin{aligned}
\frac{\partial \mathbf{P_{iso}}(\mathbf{F})}{\partial \mathbf{F}} =& \frac{\partial(\mathbf{F}[2\mu\mathbf{E} + \lambda tr(\mathbf{E})\mathbf{I}])}{\partial \mathbf{F}} = \\
&= \mu(\delta_{ip}\mathbf{F^TF})_{qj} + (\mathbf{F^TF})_{pi}\delta_{jq} + \mathbf{F^T}_{qi}\mathbf{F}_{pj} - \delta_{ip}\delta_{jq}) + \\
&+ \frac{1}{2}\lambda(2\mathbf{F}_{pq}\mathbf{F}_{ij} + \delta_{ip}\delta_{jq}tr(\mathbf{F^TF}) - 3\delta_{ip}\delta_{jq})
\end{aligned}
\tag{4.12}
$$

which is a 4th order tensor with indices (i, j, p, q).

Once $\mathbf{P_{iso}}$ and $\mathbf{P_{aniso}}$ are computed, using equation 4.5 the forces can be calculated and also the final combined stiffness matrix, sum of $\mathbf{K_{iso}}$ and $\mathbf{K_{aniso}}$, for Implicit Euler integration.

4.3.4 Boundary Conditions (Constraints)

In practical applications a deformable body does not serve any particular purpose if it is just free moving. Most of the interesting behaviour of physical objects derives from their interaction with other objects, user manipulation and fixed or moving constraints of some of their parts. Formally this translates into adding initial and boundary conditions and constraints to be taken into account when solving the PDE of motion. For instance vertices of the mesh could be required to keep a fixed position in space or to follow a position at an offset relative to another object (like muscles relative to bones), or they could be required to slide over another object, or again to not compenetrate other meshes. In addition to the uses described above, constraints are really important in the context of this work because they allow the composition and interconnection of anatomical layers, coupling them between each other to transfer across inertia.

In terms of collision/self-collision resolution and response, typical cases arise when muscles of different groups or fat get in contact: during an arm flexion for example the lateral bulging is due to the pushing of soft tissues against each other and to the physiological muscle bulging due to contraction. Moreover, when two or more characters are interacting (during a fight for example), the effect of collision forces is very evident and the result on the skin contributes the level of drama in the action, especially in slow-motion shots where contacts cause wave propagation of the stress on the tissues. More details about the implementation and the data structures used for the collision system are given in chapter 3.

The framework developed for musculo-skeletal simulation is based on VEGA with custom implementations of constraints and collision response. The first version of this framework models constraints and collisions using elastic spring potentials. At a later stage this version was successively improved using a constraint-based dynamics approach (the framework which was used in Chapter 3). The results on muscle simulation presented in this chapter were obtained using the first version of the framework. Below details on the two methods are given.

4.3.4.1 Springs view

Spring constraints consist of two mass points connected by a virtual spring characterized by parameters such as rest length and stiffness constant (Nealen et al. 2006). When the vector $\mathbf{q}$ connecting start and end of the spring is different in magnitude than the rest length r, an elastic response force dependent on the elastic coefficient k_s is generated.

$$\mathbf{W}(\mathbf{q}) = k_s || |\mathbf{q}| - r ||^2 \tag{4.13}$$

Position and sliding constraints can be hard or soft. Hard constraints can be thought as infinitely stiff springs, keeping the end points always at the same initial distance. Soft constraints instead are springs with a stiffness constant low enough to produce "bouncy" behaviour. At each frame the new positions of the end points are read from the mesh data structure, and their distance is used to compute the Jacobian of the energy:

$$\mathbf{f}(\mathbf{q}) = k_s(|\mathbf{q}| - r)\frac{\mathbf{q}}{|\mathbf{q}|} \tag{4.14}$$

Indicating with $\mathbf{I}$ the identity matrix, the Hessian of the spring potential (Choi & Ko 2002) becomes:

$$\frac{\partial \mathbf{f}}{\partial \mathbf{q}} = k_s \Big[\Big(1 - \frac{r}{|\mathbf{q}|} \Big) \mathbf{I} + \frac{r}{(|\mathbf{q}|)} \mathbf{q}\mathbf{q}^{\mathbf{T}} \Big] \tag{4.15}$$

The constraints force contributions are accumulated in the external forces vector and the Hessians are added to the global stiffness matrix. Sliding constraints differ from the position ones for the fact that the x, y, z coordinates of one of the end points is determined using a closest point query from one object to the other.

The offending vertices on which collision forces are computed are the ones of the high resolution embedded mesh, but the solver deals internally with simulation of the tetrahedral mesh only. Therefore using barycentric coordinates the forces are distributed to the tetrahedral nodes.

Collision/self-collision constraints implemented as springs are based on the penalty method. After a collision is detected, to prevent mesh compenetrations in the next timestep a response has to be generated in the form of repulsion force. The penalty method tries to prevent a vertex of a mesh entering another mesh by checking if the point lies within a threshold distance from the object and if so, instantiating a zero-length spring that applies a penalty force proportional to the penetration depth d. This method is not fully free of self-penetrations. In order to have more responsive collisions, in this work the penalty force is an exponential function of d.

4.3.4.2 Constrained Dynamics view

The other way to treat collision responses is by incorporating mathematically defined constraints of the form $\mathbf{C}(\mathbf{x}) = \mathbf{0}$ into the dynamics system matrix and solve the resulting Linear Complementarity Problem (LCP). With this system it is in theory impossible that the constraints are violated and the output is velocities of the deformable object's vertices that are guaranteed to not intersect.

For **position and sliding constraints** the mathematical form is:

$$C(p_A, p_B) = n^T \dot{(} p_A - p_B) \geq 0$$

where the normal for the position type is:

$$n = \frac{p_A - p_B}{|p_A - p_B|}$$

for the sliding type is $n = n_{objectB}$ and for the **collision/self-collision** type n is the collision normal.

A constrained dynamics system was implemented at MPC after the work produced in this Chapter by an intern student (Haapaoja 2016) and successively improved by me and used in Chapter 3. Please refer to Haapaoja (2016) for in-depth details on the collision system used. More details on constrained dynamics can be found in Otaduy et al. (2009) and Tournier et al. (2015).

4.4 Implementation and Results

In this section the details of the setup and simulation of the prototype anatomical arm example are presented, in particular the layered approach inspired by previous work (Lee et al. (2009), Comer et al. (2015) and Clutterbuck & Jacobs (2010)).

The formulation presented in the previous sections was ported to code following the interfaces provided by the library VEGA and extending classes *IsotropicMaterial*, *isotropicHyperelasticFEM*, *isotropicHyperelasticFEMForceModel*. In particular, the simulation loop algorithm can be summarized as follows:

```
1: for each element do
2:     Compute $F$ from its vertex positions (eq. 4.1);
3:     Compute $dP/dF$ (eq. 4.12 and eq. 4.10);
4:     Compute $K_{iso}$ and $K_{aniso}$ (eq. 4.3.2);
5:     Accumulate result to global stiffness matrix;
6: end for
7: for each spring constraint (if any) do
8:     Compute its $K$ and accumulate to global stiffness matrix;
9: end for
10: Prepare multibody system matrix $A$ using Implicit Euler;
11: Solve for velocities $\Delta v$;
12: for each constraint expressed as $C(x) = 0$ (if any) do
13:     Add its contribution to Jacobian matrix;
14: end for
15: Solve LCP and add $\Delta v$ to unconstrained velocities;
16: Use new velocities to compute new positions;
```

Algorithm 1: *Pseudo code for the simulation loop*

In terms of contact detection, the method in McAdams et al. (2011) could also be implemented. In it the high-resolution mesh is sampled (proxy points x_p). For each sample, first its barycentric coordinates with respect to the closest deformed tetrahedra containing it are calculated. The iso-value of the material point obtained is then calculated for a level set in the undeformed configuration and the closest point on the undeformed surface selected. This point x_s is then queried back in the deformed configuration so that the penetration depth and normal are $|x_s - x_p|$ and $\frac{(x_s - x_p)}{|x_s - x_p|}$ respectively. When a collision is detected, zero length anisotropic springs are created between x_s and x_p so that there is a sliding effect on the plane perpendicular to the penetration direction.

4.4.1 Bones

Bones are treated as articulated rigid bodies, inheriting exactly the same transformation as the corresponding Maya bone in the driving rig. The shape of bones at their extremities is generally irregular and the corresponding joints are simplified using models common in robotics. For example the elbow is represented with hinge joints, assuming the rotation happens on one constant axis; the humerus is a ball-socket joint. The underlying rig implements rotation of the radius over the ulna during *pronation* and *supination* of the forearm. In the examples of this section the skeletal bones used are: scapula, humerus, radius, ulna of the right arm/forearm.

4.4.2 Muscles and Tendons

The 3D muscles in the prototype are represented as a set of volumetric elements with embedded fibre directions that follow the transformation of the bones they are attached to. The 14 muscles simulated in the examples below are:

- Biceps Brachii, Lateral Triceps Brachii, Medial-long Triceps Brachii, Brachialis, Anconeus
- Superficial extensors (combo of brachioradialis, Extensor Carpi Radialis Longus, Extensor Carpi Radialis Brevis), Extensor Digitorum, Extensor Digitorum, Pronator Teres, Flexor Carpi Ulnaris,
- Flexors (combo of Flexor Carpi Radialis, Palmaris Longus, Flexor Carpi Ulnaris), Extensor Carpi Ulnaris, Flexor Digitorum Superficialis, Flexor Carpi Ulnaris, Abductor Pollicis Longus.

In this setup, muscles are attached to the bones geometry typically at two points, proximal (origin) and distal (insertion) following anatomical references found in medical literature and online (Zygote Body 2016). To this aim, vertices of the tetrahedral mesh are pinned to the bone mesh via position (hard) constraints. Some muscles like the deltoid, biceps brachii, triceps or the gastrocnemius (calf) have two or three heads with which they attach to two or more bones they span: these muscles are a unique mesh but often they are modelled as separate geometries because splitting them enhances modularity and finer control of deformation over specific parts. On the other hand, given the vast number of superficial muscles on the forearm, it is also beneficial for the purpose of faster simulation times to group adjacent muscles together. These simplifications are generally decided beforehand and in general they do not affect the visual result: muscles are tightly packed together and for many movements they move in sync.

Once the models are created, tetrahedralized and attached to the bones using anatomically-based constraints, the next step is to continue the preprocessing by defining the per-element fibre directions. The anisotropic material defined in section 4.3.3 has to express the state of the fibres that can be active or passive. The peculiar characteristic of the muscle tissue is its ability to contract and assume different shapes as a consequence. The visual appearance of muscles bulging is determined at the micro level by the activation of a huge number of fibres that slide over each other due to biochemical firing processes. Muscles bulge in fact because these fibres overlap one on each other during contraction, shortening the muscle belly and stretching the tendons. Moreover, blood permeates the tissues therefore, being a fluid, volume has to conserve.

In practice these requirements translate into an extension of the passive volumetric model with an embedded 3D fibre field that can be thought of as a flow from tendon origin(s) to tendon end(s) and which makes the material stiffer in their direction when activated (anisotropy). Initially the fibres were intended to be modelled semi-automatically as explained in (Saito et al. 2015): solving a Laplace flow equation from the origin to the insertion positions on the tendon with mixed boundary conditions

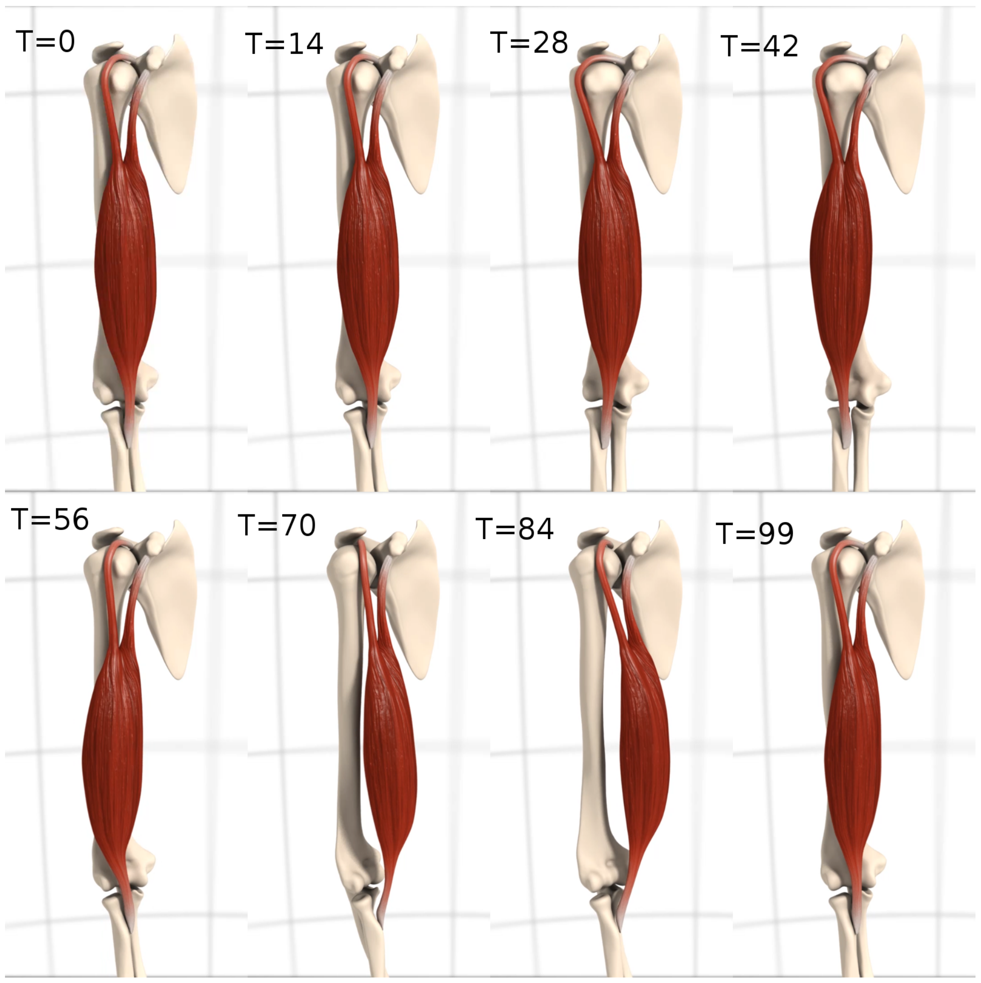

Figure 4.9: *Temporal frames extracted from an animation of the humerus rotating with biceps brachii having non activated fibres.*

(i.e. the flow through the epimysium set to null). Even though this solution would be highly effective, in the case of the arm the muscles involved are generally fusiform therefore for each muscle the vector connecting insertion and origin points is calculated and its direction assigned to each tet of the associated muscle. This method would not work for muscles such as the trapezius.

The importance of the fibre-activated material is not only limited to the shape. During an animation in fact some muscles will be fully contracted, while others will stay passive and others will be partially activated. The activation level determines the stiffness of the material and it is in general not uniform across all the fibres. In visual terms this means that a

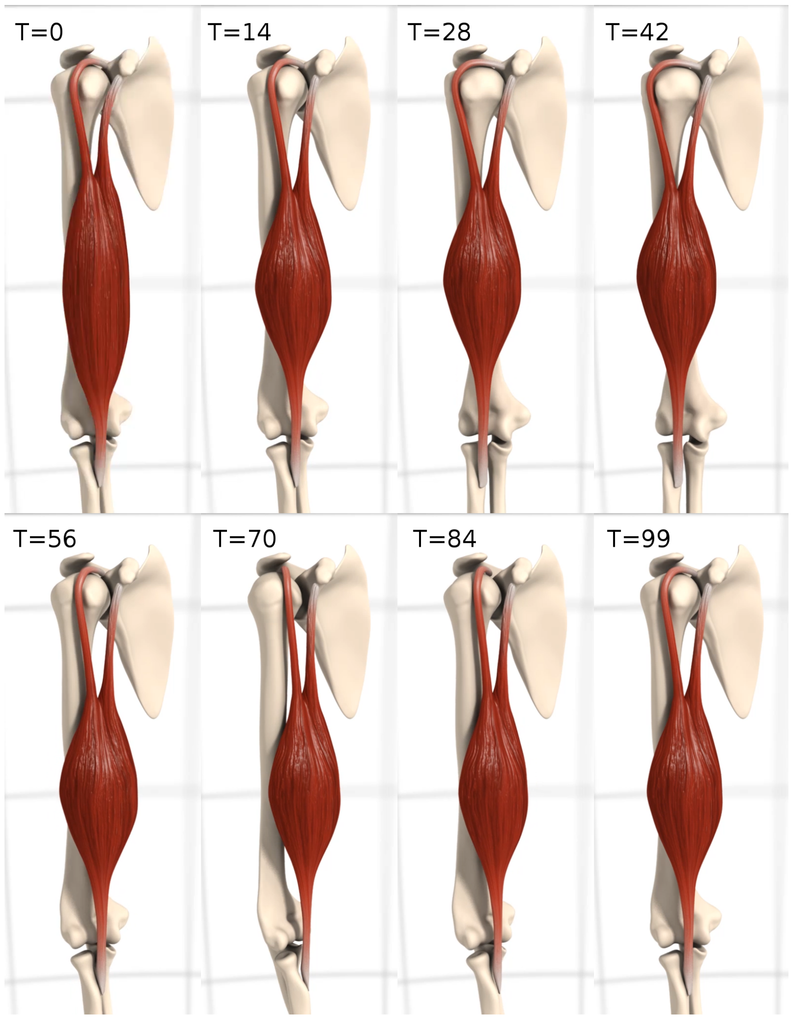

Figure 4.10: *Temporal frames extracted from an animation of the humerus rotating with biceps brachii having activated fibres.*

contracted muscle appears to jiggle much less than a relaxed one. In the example of a male athlete running, his pectorals appear very dynamic because of the momentum of the soft tissue due to gravity and also due to the balancing forces applied back in response to stepping on the ground; but if he keeps them voluntarily contracted they appear much stiffer and the noticeable jiggle is due mainly to the superficial adipose tissue. Figures 4.9 and 4.10 illustrate this behaviour: the same animation of a muscle constrained to rotating bones looks different if the fibres are not firing (passive material) or are activated (material becomes stiffer and so is less governed by inertial motion).

Muscle activations are a fundamental parameter of the anisotropic material. Their value is time-varying and in these examples this was controlled by manually created animation curves. An automatic approach instead would be the one in (Teran et al. 2003) or analogue method that outputs a real number between 0 and 1 based on the angles and poses of the skeleton. MPC rigs already have such a system to control flex shapes therefore it would be technically easy to plug that in. Activation levels can additionally be tweaked by technical animators in actions that involve for instance heavy lifting, pushing of heavy objects and in general isometric contractions, where the muscles bulge but the pose does not change in time.

The Young's modulus material parameters for the simulation were inspired by the literature but in practice tweaked to achieve visually pleasant results. This is common in every day Visual Effects dynamics production in which the goal is to achieve good looking results and stay physically plausible even and often at the cost of using non physical parameters. As a general principle, flesh (muscles), tendons and fat should have all different Young's modulus. For the same tet mesh therefore it is common to have an heterogeneus combination of different material properties. Tendons for example are not separated from the main muscle body mesh and have a much stiffer material on the tetrahedra belonging to them. The parameter values used in the solver presented in this chapter are:

- Muscle: density 1000 Kg/m^3, Young's modulus $9 * 10^6$, Poisson ratio 0.45
- Tendon: density 1000 Kg/m^3, Young's modulus $15 * 10^6$, Poisson ratio 0.45
- Fat: density 1000 Kg/m^3, Young's modulus $1 * 10^6$, Poisson ratio 0.45

Tendons of the hand are not modelled in these examples even though they are very important visually. They are generally modelled in biomechanics using the strand model (Sachdeva et al. (2015)). Recently, they have been modelled accurately in the Eulerian-on-Lagrangian framework (Pai et al. 2014), even though their effect on the skin due to collision and sliding was not modelled.

In Teran et al. (2005a) the connections between different muscles are expressed through links (line segments). In the rest pose some points of a source geometry are sampled ($\vec{x}_{samp}$) and for each one its closest point $\vec{x}_{anch}$ (anchor) on all the neighbouring muscle surfaces is associated. During simulation the link with the closest anchor point becomes active and determines the collision response force (with springs for example). At each time step, the positions and the normal velocity components of a sample are set to match the ones of its anchor:

$$\vec{x}^{'}_{samp} = \vec{x}_{samp} + \alpha[(\vec{x}_{anch} - \vec{x}_{samp}) \cdot \vec{N}]\vec{N}$$
$$\vec{v}^{'}_{samp} = \vec{v}_{samp} + \beta[(\vec{v}_{anch} - \vec{v}_{samp}) \cdot \vec{N}]\vec{N}$$

where $\vec{N}$ indicates the normal at the surface point and α, β are control coefficients. After having tried a similar approach for sliding, i.e. setting explicitly the normal velocity of the sliding nodes (Warburton 2014), for this work it was decided to use general spring sliding constraints which served the purpose. Even though the framework supports collisions, these were used at a minimum in the examples. Not only do they considerably increase the computations, but in practice they revealed to be not necessary for contact of adjacent muscles in the same groups. It is enough in fact to use just sliding constraints between them. Collision handling was necessary though for contact between muscles in different groups such as the biceps brachii and the brachioradialis to obtain the compression of the tissues when the forearm flexes.

Figures 4.11, 4.13 and 4.15 show the simulation results of an animation of the right arm performing a flexion of 130 degrees followed by a pronation and a supination (twisting of the forearm left and right). No gravity was used. Muscles slide over each other, an effect particularly evident for the biceps brachii on the brachialis. Muscles also slide and collide with the rigid bones as shown by the tendons wrapping around them during twisting. Very thin muscles such as the anconeus presented particular challenges especially for the collision system because it is constantly in contact with multiple bones and it undergoes large amount of stress in the elbow region. This required making its material softer (Young's modulus $5 * 10^6$) and the increasing the spring stiffness constants for that area.

4.4.3 Fascia, Fat and Skin

The deep fascia holds single muscles together and keeps them closer the underlying skeleton during motion. In the approach by (Teran et al. 2005a) an extra term is added to the energy distribution to encourage resistance to stretching only on the surface; in practice this is done by injecting a linearly elastic stress in the diagonalized form of the constitutive model during elongation. In the work by (Comer et al. 2015), which considers it as an adaptive tangential tensegrity model (Myers,T. 2013), the tensive and compressional material of the deep fascia are modelled with biphasic springs (i.e. having different constants in extension and compression). The concept of tensegrity is essential in biomechanics and means that every part of the body is subject to either pushing or pulling. In this work the deep fascia that wraps single muscles was not explicitly modelled as it was not considered very influential in the visual look of the simulation.

As far as the superficial fascia is concerned, it is represented geometrically as a mesh wrapping the union of all the muscles geometries. This mesh can be generated by a cloth simulation with negative pressure as in CGCircuit (2016) or can be obtained by projecting the renderable skin on the muscles in the normal direction. With this method it could be necessary to fix artifacts such as vertex crossings in the armpit region, non homogeneous distribution of vertices (large versus small polygons) or mesh crumpling in region with highly discontinuous surface curvature. During simulation, a custom MPC wrap-deformer makes the triangular fascia geometry follow the muscles by binding it smoothly to the closest detected points. This layer is essential, as noted in Saito et al. (2015), to create separation with the next layer: the fat.

The tetrahedral fat layer is obtained using MPC's Kali toolset as the volumetric offset space between the fascia and the skin. It is driven by the fascia and attached to it via soft sliding constraints (zero-length springs) distributed regularly. Its typical jiggly behaviour is modelled using a passive isotropic material (StVK in the examples).

Figures 4.17 and 4.19 show the interaction of all the 3 layers together (please refer also to the videos at `http://www.fabioturchet.com/supplemental_material.zip`). In red colour are the simulated muscles, in yellow the wrapped fascia and in blue the fat/skin layer. The fascia was cached and serves as driving geometry: there is no coupling because the 3 layers were simulated separately. As can be seen (and especially in the videos), the desired sliding effect of the muscles and the bones under the adipose tissue was obtained, while self-collisions contribute to the lateral bulging in the folding region of the elbow joint. It is exactly these subtleties and nuances that make the skin look "alive". At this point, an optional last pass for the triangular geometry of the skin on top of the fat layer can be performed to generate the final renderable mesh with high-resolution and higher frequency wrinkles (Li & Kry 2014).

This chapter has presented the approach that was taken to the musculoskeletal physical simulation of the layered tissues present in a human arm. Even if this work takes inspiration from the techniques presented in Teran et al. (2003) and Teran et al. (2005b), there are some differences. First of all they don't use a fascia layer to drive the fat, but directly connect the muscles to the fat geometry which doesn't highlight effects such as sliding of the skin over the bones and the muscles. Secondly they do not integrate dynamics in the muscle simulation, which is kept quasi-static. In this work instead the framework supports inertial effects at the solver level and their effect is controllable with material, activation and damping parameters. Moreover, muscle-to-muscle collisions are not explicitly computed in this work and their effect replaced by the use of sliding spring constraints. On the fat layer instead self-collisions are computed explicitly with a point/tetrahedron collision test. At the material level, the material model used in Teran et al. (2003) adopts

Mooney-Rivlin equations for the isotropic part, while here STVK is implemented. Lastly, an explicit analytical formulation has been derived in this work for the fiber-activated constitutive model so that it can be integrated in modern FEM solvers such as VEGA.

In the next chapter, the creation of a customized version of the same solver and tools for artists are presented such that the task of placing anatomical meshes from a template library is made more efficient and interactive.

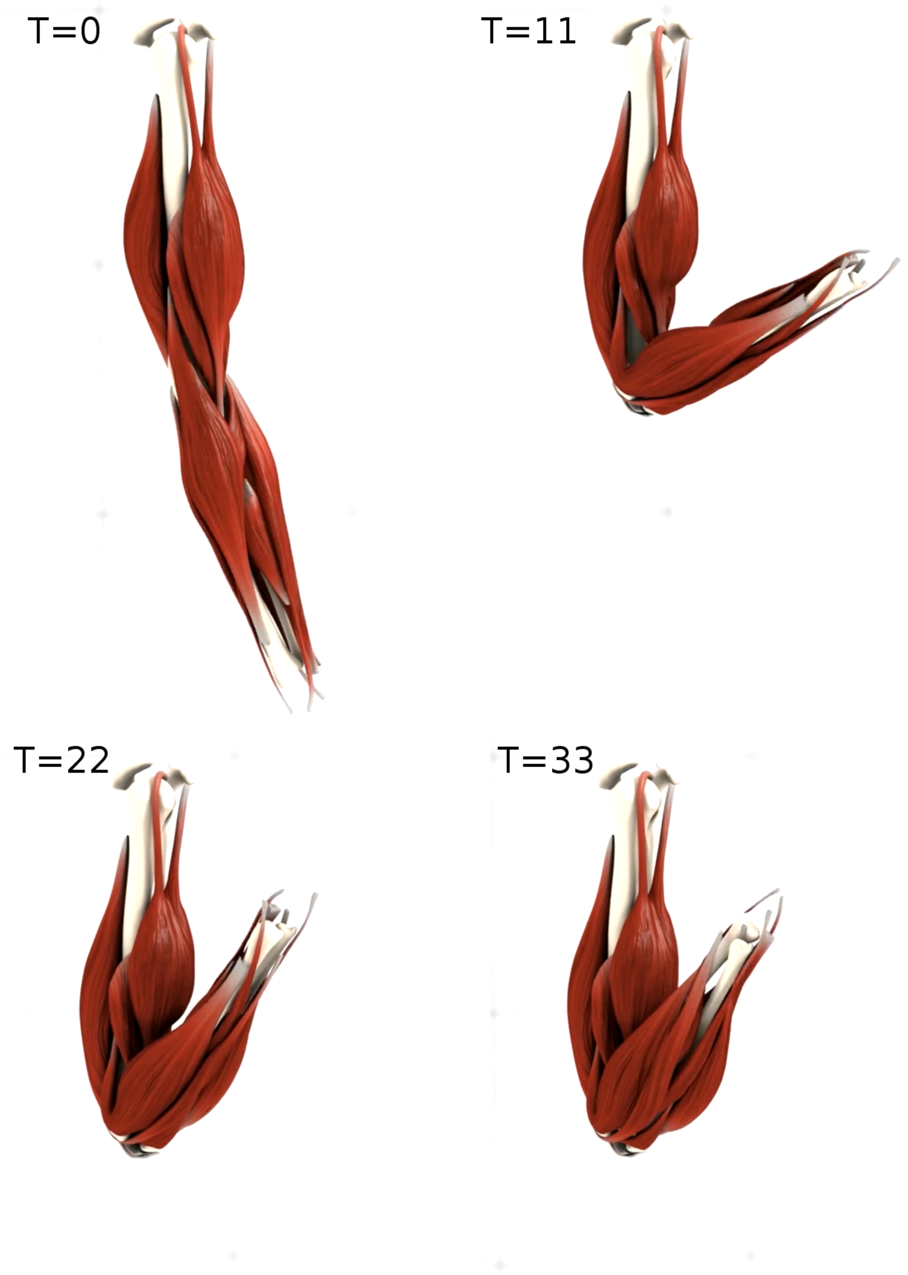

Figure 4.11: *Full arm simulation. View 1.*

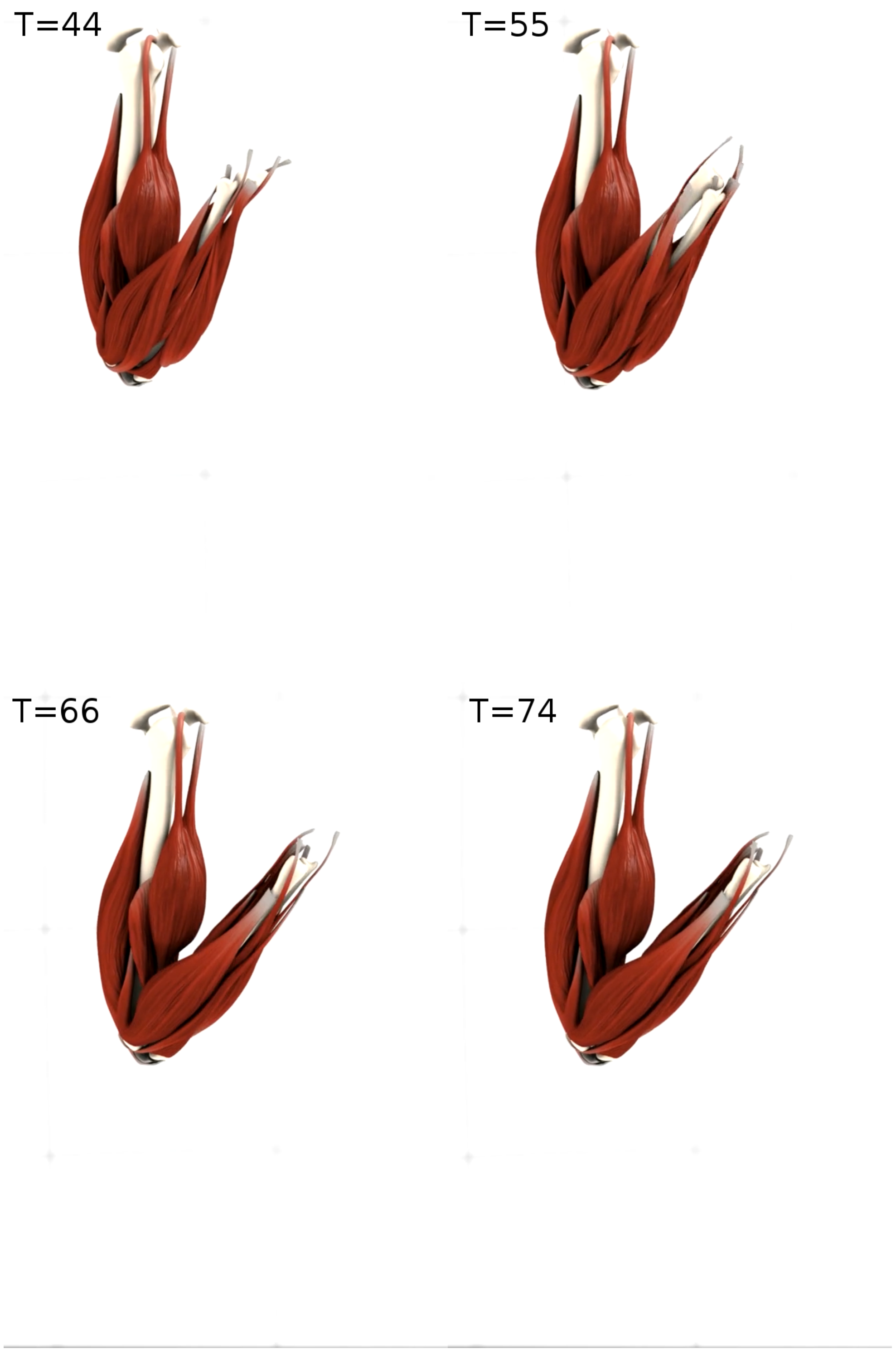

Figure 4.12: *Full arm simulation. View 1. (cont.)*

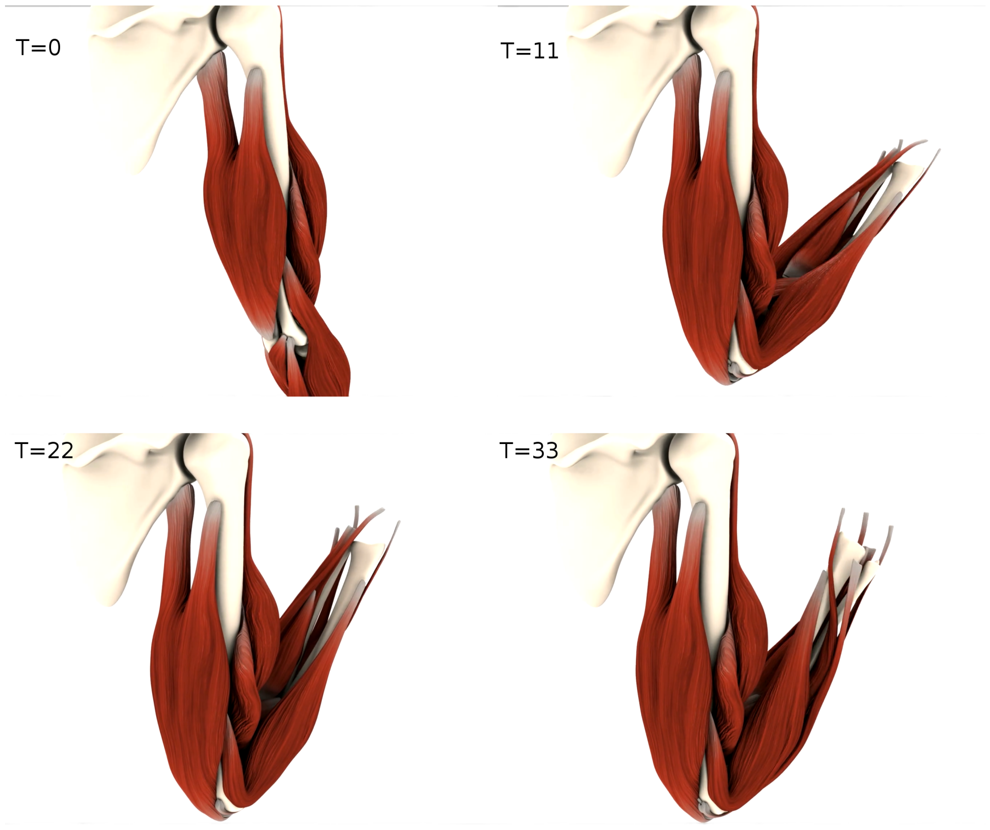

Figure 4.13: *Full arm simulation. View 2.*

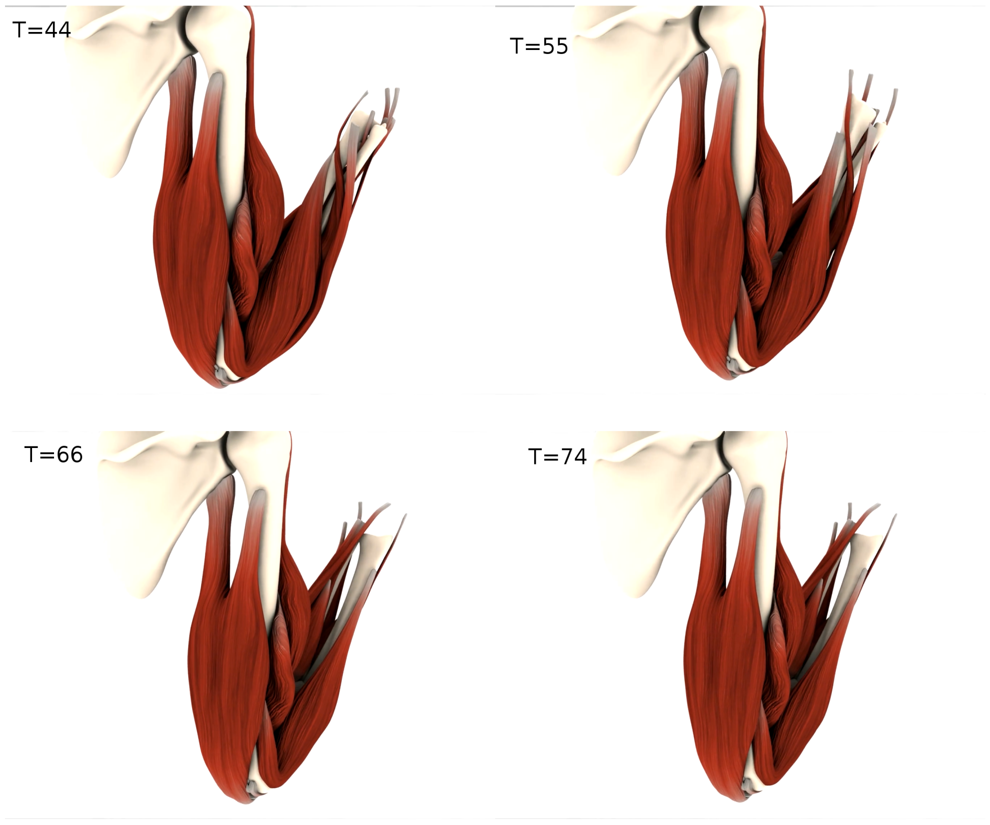

Figure 4.14: *Full arm simulation. View 2. (cont.)*

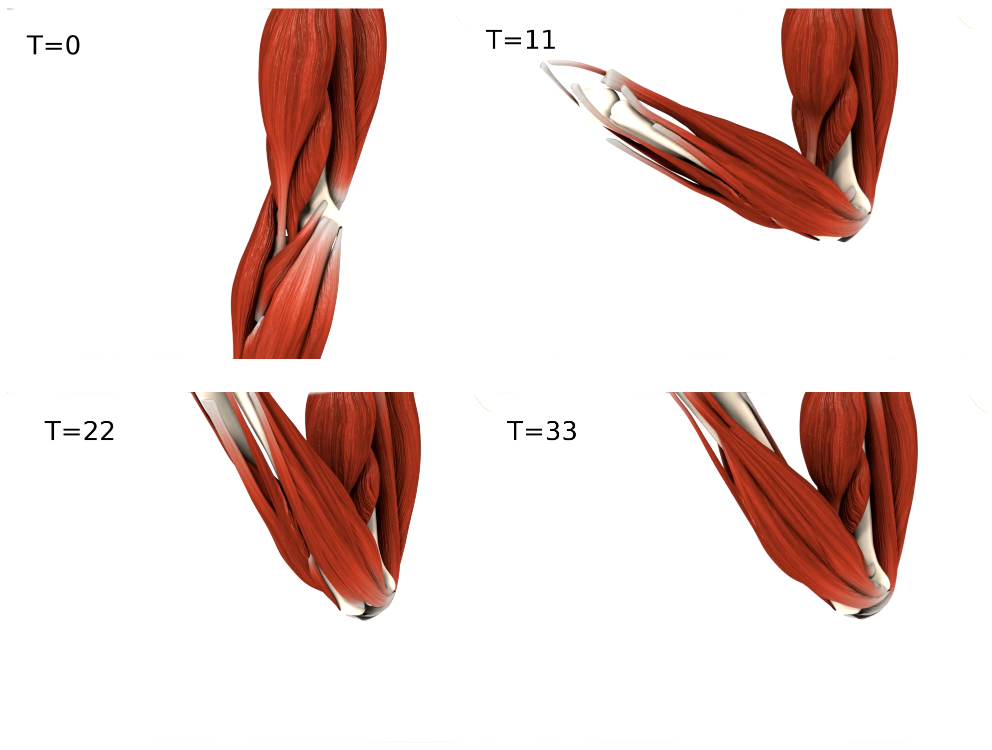

Figure 4.15: *Full arm simulation. View 3.*

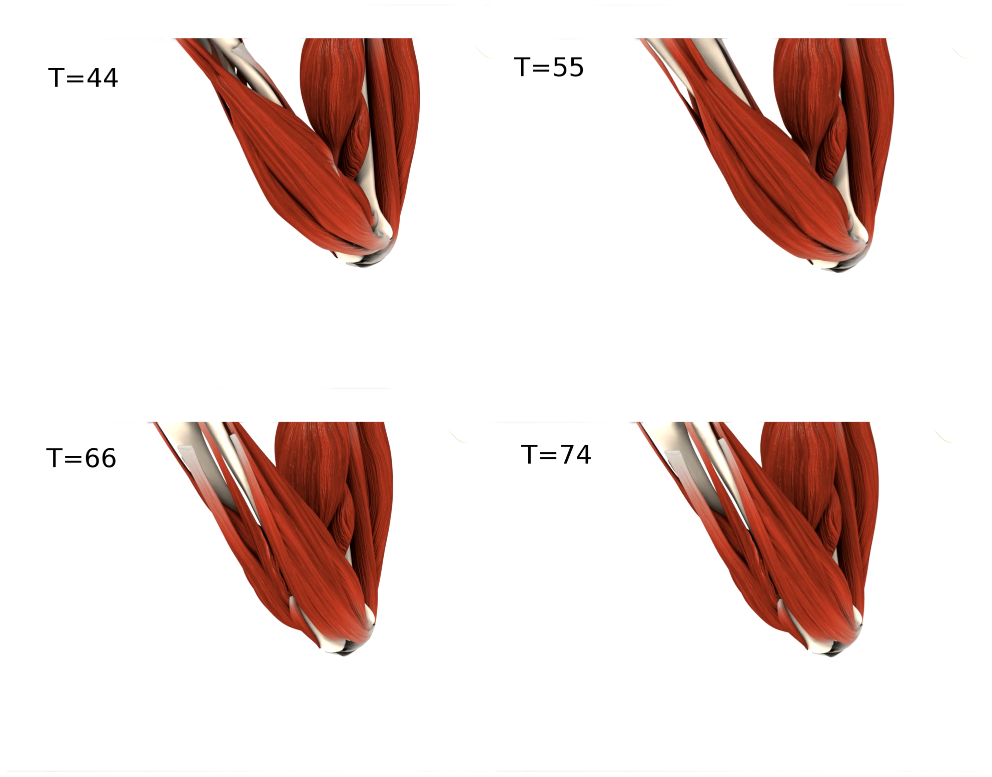

Figure 4.16: *Full arm simulation. View 3. (cont.)*

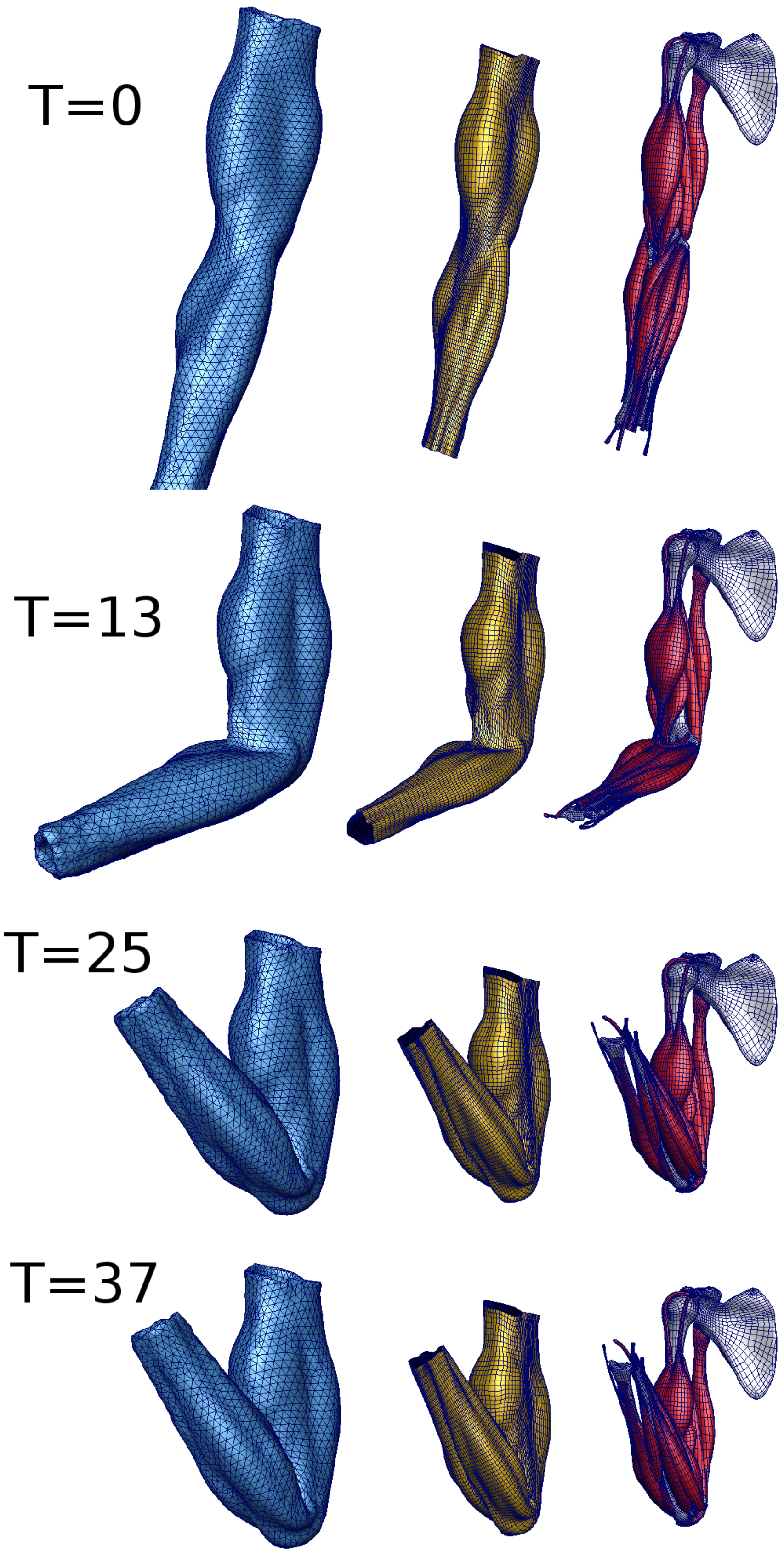

Figure 4.17: *Full arm simulation layers. View 1. Muscles in red, fascia in yellow and fat/skin in blue.*

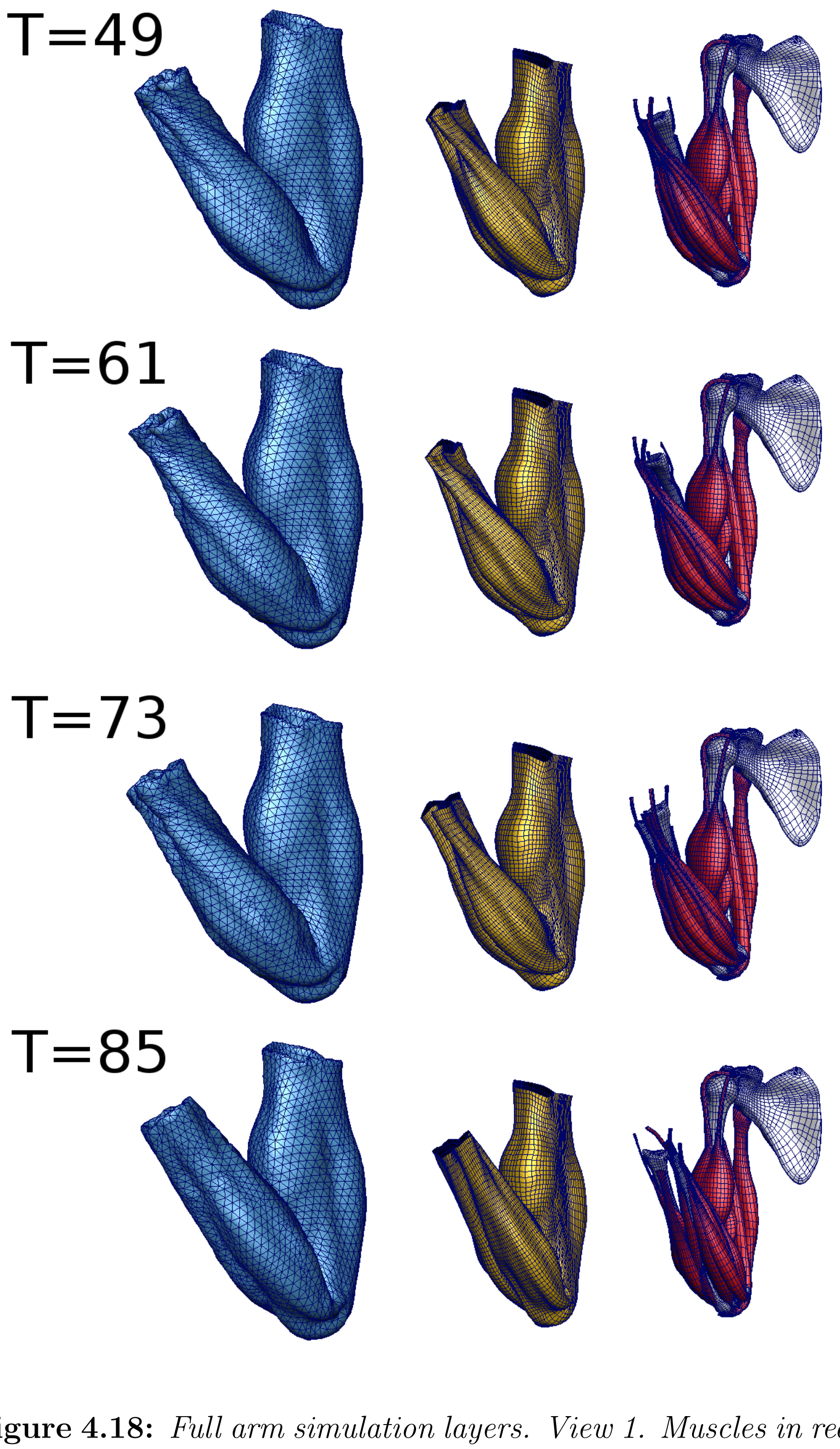

Figure 4.18: *Full arm simulation layers. View 1. Muscles in red, fascia in yellow and fat/skin in blue. (cont.)*

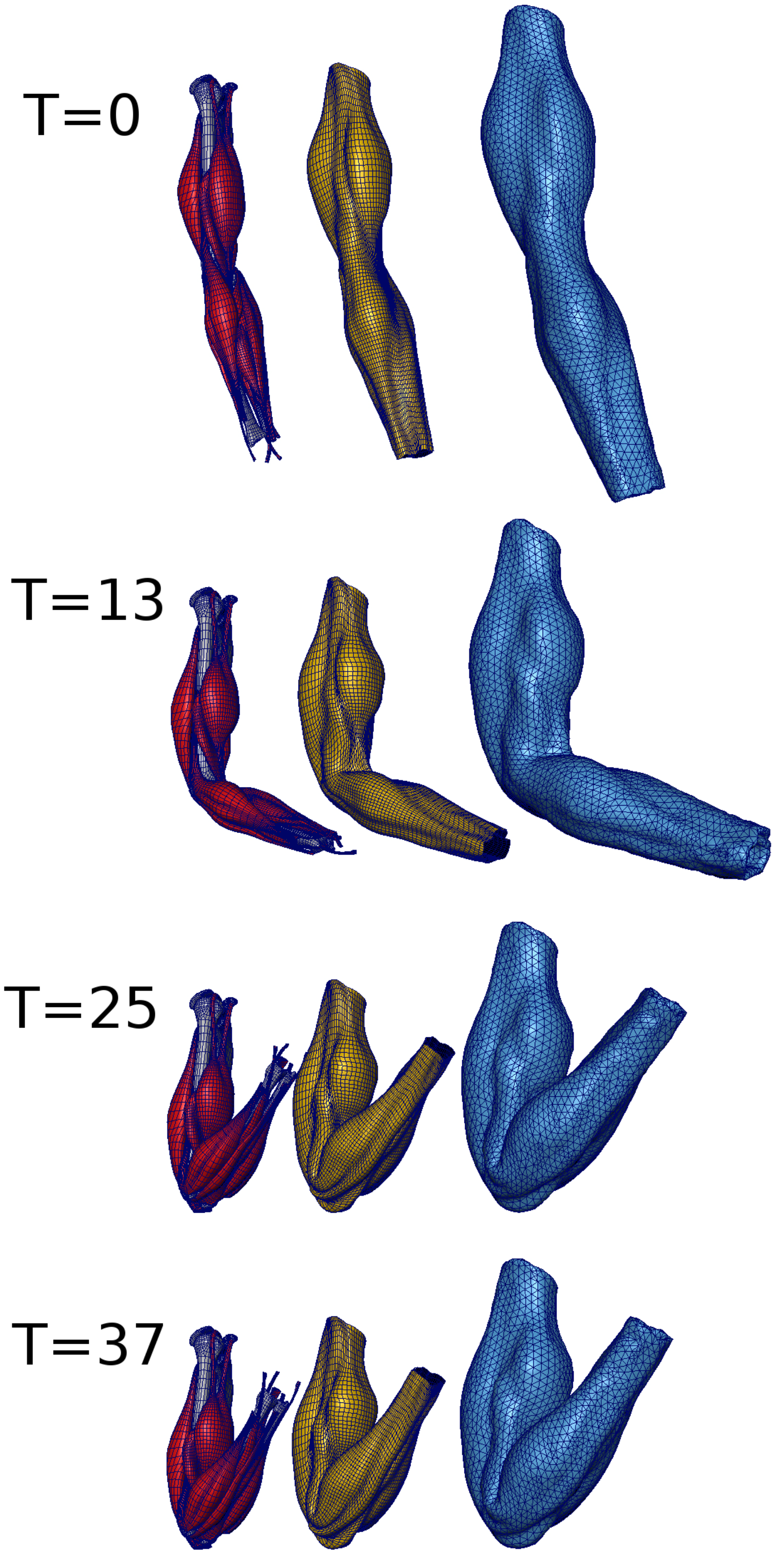

Figure 4.19: *Full arm simulation layers. View 2. Muscles in red, fascia in yellow and fat/skin in blue.*

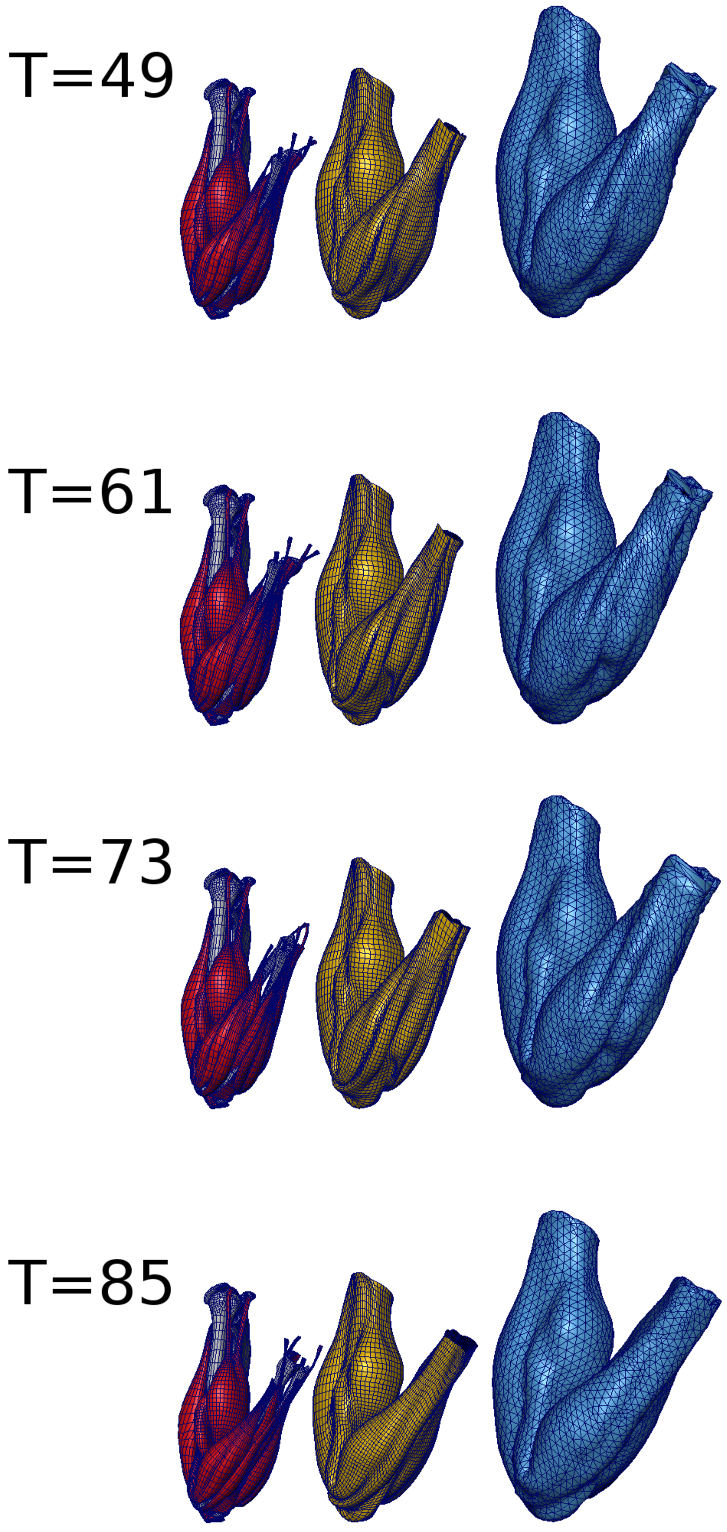

Figure 4.20: *Full arm simulation layers. View 2. Muscles in red, fascia in yellow and fat/skin in blue. (cont.)*

Chapter 5

Muscle Placement

5.1 Introduction

As shown in Chapter 4, one of the main techniques adopted nowadays in the industry to simulate deformable objects is the Finite Element Method (FEM). Despite the life-like results, the setup cost to generate and tweak volumetric anatomical models for a FEM solver is not only very high, but it cannot easily guarantee the quality of the models either, in terms of simulation requirements. Unless a system such as the one presented in Chapter 3 is used, in a production environment in fact models often require additional processing in order to be ready for FEM simulations (see section 3.1.1). For example, self-intersections or interpenetrations in the rest pose may result in unwanted forces from the collision detection and response algorithms that negatively affect the simulation at its start.

In this chapter a prototype framework and toolset are presented, implemented as a Maya plugin and based on the 3D deformable object FEM library VEGA (Sin et al. 2013b). The goal is to assist artists and technical directors (TDs) in the creation of simulation-ready muscle models in a production environment. Current 3D authoring applications (such as Autodesk Maya or SideFX Houdini) do not explicitly provide efficient solutions for this task. Therefore a way to minimise the number of iterations between geometry modelling and production of simulation-ready meshes is proposed, which allows the artist to see the simulated result of contracting muscles interactively. As a result the efficiency of modelling targeted to simulation is increased.

5.2 Related Work

Interactivity is a crucial part of any design system that aims to speed up the artistic process. Existing literature focuses on the application of fast deformation algorithms to the authoring of deformable objects with specific desired properties, fast prototyping, design of organic objects such as vegetation and user control. For example Barbič et al. (2012) propose an animation editing tool leveraging on the power of model reduction and the computational efficiency of linearized elasticity that allows the direct manipulation of vertices of a simulated geometry at any frame with instant adjustment of the full animation in response. Constraints and physics are respected via a space-time optimization.

One of the main advantages of interactive methods is that they amplify the creative possibilities of the artists by allowing the exploration of a vast space of designs in a short time and provide instant feedback on the constraint choices. One example of this characteristic is represented in the work by Xu et al. (2015b) in which the user can design nonlinear isotropic and anisotropic materials for soft-body simulation intuitively and interactively by editing spline curves in an interface. The system works by expressing internal forces and a stiffness matrix in the space of principal stresses (the singular values of the deformation gradient $\mathbf{F}$) and using separable strain elastic energies. As a result this gives much freedom in the definition of material properties because the user directly edits the stress/strain curve. Xu et al. (2015a) instead use model reduction to greatly increase optimization speed while calculating heterogeneous material properties for deformable objects. The user specifies desired displacements and internal forces which allows the calculation for example of accurate contact forces in fabrication (inverse) design. This means that the user is freed from the tedious work of setting material parameters and can instead follow a goal-oriented approach 'starting from the end': the optimization will take care of finding the physical parameters that during simulation lead to the desired result. Similarly, Xu & Barbič (2017) describes a method to design example-based linear or nonlinear damping properties for a simulation, by controlling a spline curve.

An interesting complex application of interactive design is represented by vegetation. Similar in spirit to this work's goal to produce simulation-ready meshes, Zhao & Barbič (2013) propose a method that applies domain decomposition to the processing of a polygonal "soup" representing a tree and outputs separated geometries ordered in hierarchy for fast simulation with minimal user input. From a user selection of triangles into basic classes, the system automatically builds a domain graph and uses model reduction for a fast authoring of simulated plants, including predecided fracturing. Hädrich et al. (2017) produce stunning results for climbing plants authoring using a meshless based representation, specifically anisotropic oriented particles. In this way the system is not only very fast because of its parallelism, but also supports a multitude of operation such as bending, breaking, physically and biologically based growth. Using a similar method, Pirk et al. (2017) propose a system for the interactive simulation and artistic control of wood combustion for botanical tree models.

Recently, neural networks and, specifically, conditional generative adversarial networks have also been applied to help artists accelerate the design process (Guérin et al. 2017), opening a promising new direction for the application of machine learning in Visual Effects.

5.3 Method

A typical workflow in the system presented in this chapter consists of the following macro steps (illustrated in Figure 5.1):

- Import of an existing muscle template from a library of meshes or existing muscle rigs;

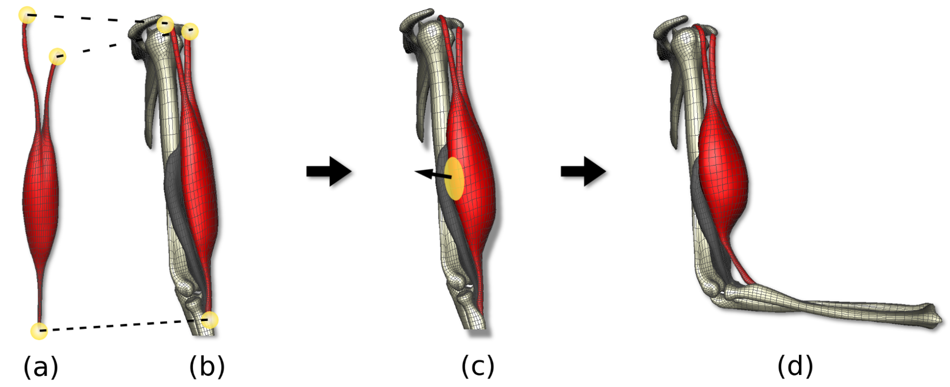

Figure 5.1: *Main steps of the system for a scene with biceps brachii and brachialis muscles. From left to right: (a) rest shape of a muscle; (b) dynamic placement; (c) context-aware sculpting of intersection-free geometry with tetrahedral cage deformation; (d) simulation with contraction of the newly created muscle.*

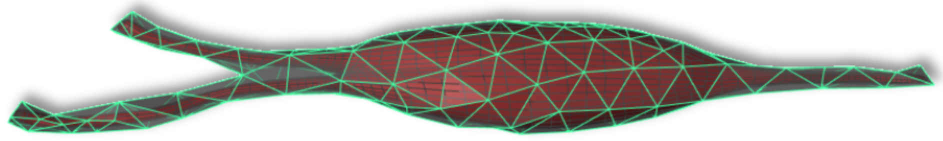

Figure 5.2: *Input tetrahedral and embedded meshes for the biceps brachii. Highlighted in green and with a semi-transparent shader is the low resolution tetrahedral cage. In dark gray the underlying high resolution embedded mesh.*

- Interactive physics-based placement of the muscle geometry through manipulation handles;
- Sculpting of the muscle automatically avoiding interpenetration with surrounding objects;
- Simulation and contraction preview of the newly generated shape.

5.3.1 Initial muscle data preparation

A typical muscle simulation such as the one presented in Chapter 4 requires a tetrahedral mesh, a high resolution triangular mesh for rendering, collision objects and constraints (boundary conditions). As discussed before in Chapter 4, a mesh for rendering is embedded by using barycentric coordinates or similar methods and collision objects can be either rigid, for example, geometry for bones, or deformable, i.e. other muscle geometry. In addition, the tetrahedral mesh contains volumetric vector attributes such as a fibre field, continuum mechanics materials and activation levels used during contraction.

The system assumes the existence of a template library of pre-sculpted anatomical models of bones, muscles and skin (Figure 5.2). The source models for the library can be taken from commercially available collections, as well as reconstructed from freely available medical MRI/CAT scans and muscles from existing characters. This work makes use of an adapted 3D model from (CGCircuit 2016) which in turn builds on the scans of real subjects.

5.3.2 Muscle placement

Once the model is selected from the library, the muscle placement stage begins. The goal here is to place muscle attachments of the template model near the bones via an interactive user-controlled simulation. Muscle attachments are sets of vertices (typically of the tendon geometry) hard-constrained to a driving handle mesh (such as a simple sphere). One of the main features of this system is that it solves for collisions with nearby muscles and bones during the placement process, elastically adapting the muscle to preserve its volume. In this way the framework differs from standard 3D modelling tools which do not provide these features and which result in plastic deformations that can hardly produce a simulation-ready mesh.

To control the placement, the user can add hard constraints on specified nodes of the mesh which serve as 6-DOFs manipulators. In the integrator, which implements Implicit Backward Euler (Eq. 4.4), the constrained nodes inherit position and velocity of these manipulators, rather than being directly solved. This produces a change of the deformation gradient that triggers elastic deformation. Rayleigh stiffness damping

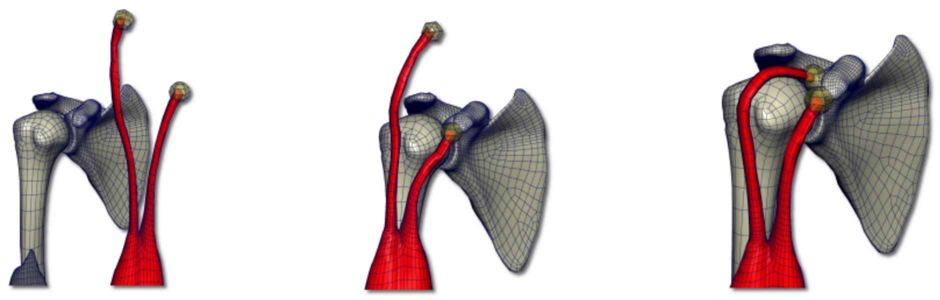

Figure 5.3: *Placement of the tendon handles in place over the humerus bone.*

(Sin et al. 2013a) and zero gravity are used to limit the effects of secondary motion; a quasistatic version of the solver could be alternatively used, that is a version without inertial effects and where the solution positions satisfy the equilibrium of all forces, i.e. their sum is equal to zero. In placement mode all surrounding objects remain rigid (Figure 5.3). For fast intersection and response tests with static objects such as bones Signed Distance Fields (SDF) are used (Sanchez et al. 2012). For collision detection and response queries with dynamic objects, such as other muscles present in the scene, SDFs would be too slow because of the re-building of the field. Therefore a fast distance approximation with a BVH spatial data structure is used instead. Collision detection is based on the method described in Teran et al. (2003).

As mentioned in Chapter 4, collision response is performed using a simple penalty-based method in which objects have a small collision offset hull around them. For each colliding vertex of the embedded mesh, a virtual spring is instantiated in the penetration direction and its dampened force is implicitly applied at each substep to the closest corresponding node on the cage. In the executed tests an isotropic nonlinear St Venant-Kirchhoff constitutive model was used (Equation 4.3), however a faster yet less accurate linear corotational material could also be used at this stage.

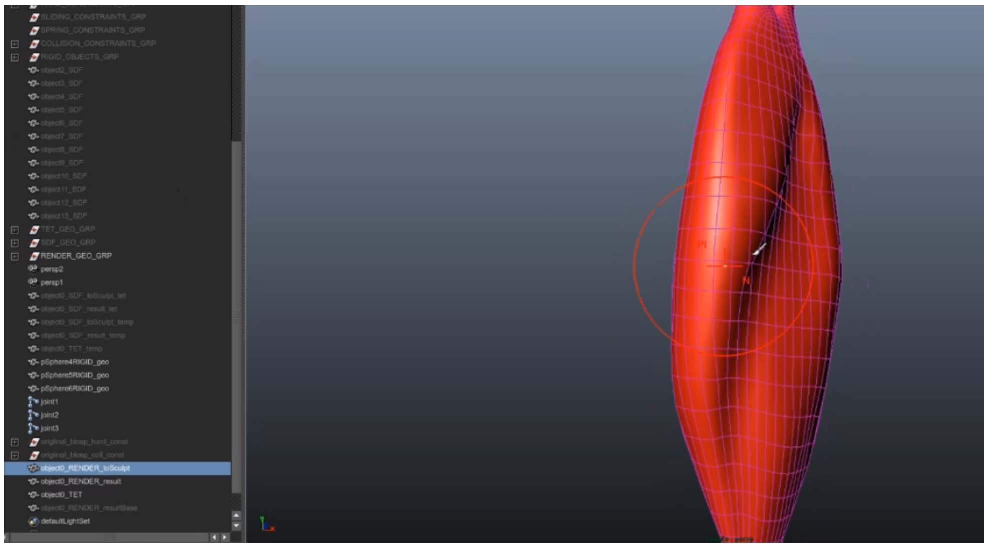

Figure 5.4: *Sculpting tool interface in Maya.*

5.3.3 Sculpting

Once the placement process is complete, the artist might still require further adjustments of the muscle shapes to fulfill creative and functional requirements. For this purpose the toolset builds on top of standard Maya sculpting tools by providing a specialized intersection resolution node, acting on the high-resolution embedded shape (see Figure 5.4 and please refer also to the videos at `http://www.fabioturchet.com/supplemental_material.zip`).

After two consecutive sculpting operations s_1 and s_2, the vertices of the new deformed mesh V_{s_2} are compared against the vertices of V_{s_1} to detect which ones have changed. After a broad-phase collision detection based on bounding boxes that finds surrounding objects, the vectors between the old V_{s_1} and new vertex positions V_{s_2} define the directions for ray-triangle intersection tests. The intersection tests can be accelerated if a static BVH is used. As intersections are solved at each operation, this ensures that in the next operation the first hit point is where the vertex is stopped. In addition, the sculpting tool can optionally apply to the point the same collision offset parameter used during simulation (Figure 5.5). The plastic deformation performed by the sculpting process is not used to generate a blend shape (i.e. a new deformed mesh with the

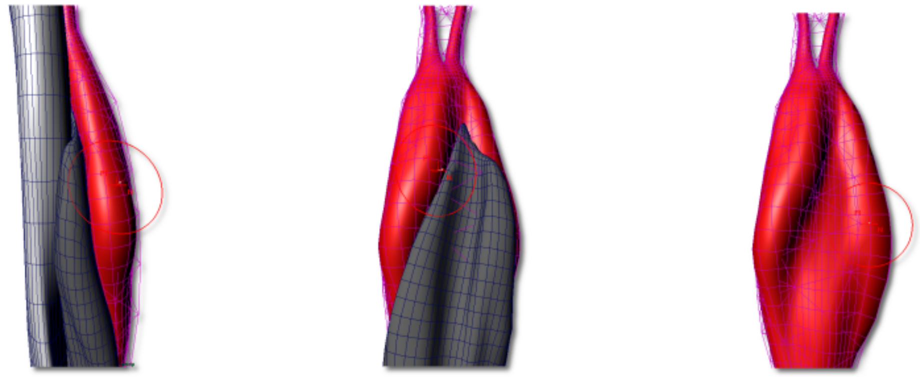

Figure 5.5: *Some steps of the sculpting process in which the mesh is pushed out but collides with an existing adjacent muscle (in gray). The red circle represents the Maya brush gizmo. The wrap deformer acts in real-time at each brush stroke, in this figure from the embedded mesh in red onto the cage in pink.*

same topology but different vertices positions that gets interpolated) for a pose, but results in a mesh that becomes a new rest pose (i.e. a new initial undeformed pose) used by the solver to compute elasticity and perform further simulations.

Note that the artist sculpts the embedded mesh, but the solver needs the volumetric cage for simulation (i.e. the tetrahedral mesh). In order to avoid additional expensive tetrahedralizations, the framework uses a custom wrap deformer based on closest point distances and adjustable falloff (action radius). The wrap deformer's job is to deform a mesh with another mesh having different topologies. This deformer is used to deform the internal nodes of the cage mesh and the associated fibre field. As a normal approach in FEM to save computation time, the tetrahedral volume has fewer degrees of freedom compared to the embedded mesh. Therefore the wrapping process cannot guarantee that the cage perfectly contains the new geometry as before the sculpting stage. This has not been a problem for the embedding process because the embedding works with barycentric coordinates (Vince 2006).

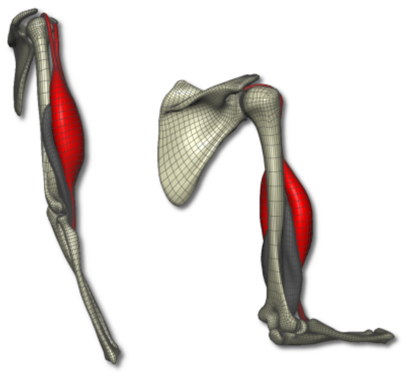
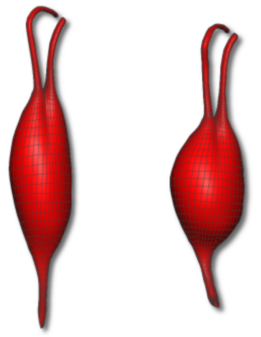

Figure 5.6: *Some steps of the simulation process, in which the bending of the elbow joint activates the contraction of the biceps brachii.*

5.3.4 Simulation

Once the new sculpted muscle is completed, the barycentric coordinates have to be recomputed and the solver is re-initialized with the new tetrahedral mesh rest shape to preview the contraction of the muscle in an animation. In the simulation step the same solver as in the muscle placement stage is used, which allows the integration of the same data structures seamlessly as a part of the same framework.

The muscle material can be changed from a pure isotropic material to a transversely isotropic material that makes use of the fibre directions field. In particular, as discussed in Chapter 4 the constitutive model presented in Teran et al. (2003) was implemented, with active and passive stress response, with different Young modulus for tendons and muscle body materials. In the simulation stage the system supports not only hard constraints, but also soft and sliding constraints. This allows the creation of the interconnected network of connective tissue known as fascia which keeps the muscles packed together during motion.

5.4 Implementation and Results

The solver and the sculpting tool are implemented as C++ multi-threaded Maya plugins. The solver extends the Maya class *MPxNode*. Its input connections are a time node, the tetrahedral and embedded meshes and various parameters such as gravity vector, iterations number, self-collisions flag which are editable from Maya's Attribute Editor. Its output is the tetrahedral mesh. Every time one of the inputs changes, the node graph is recomputed and the *compute* function of the solver is called, executing a timestep. Other solver parameters such as the material model are contained in an input file specific to each deformable object which follows VEGA's configuration file format. The sculpting tool also extends *MPxNode* and executes at any mesh editing operation performed by the user for instance using the Artisan sculpting toolbox and brushes. The wrap deformer node mentioned in this chapter is the standard one available in Maya. The initial tetrahedralization is performed using TetGen and is stored in *.veg* files, while the SDFs are stored using OpenVDB. The code can be greatly optimized performance-wise.

For simplicity, the prototype was tested on a basic two-muscles setup in which a user places biceps brachii over brachialis by moving constraint handles attached to each tendon end. In a real use case the scene could contain many muscles that would be placed in layers from the internal to the most external ones. This would not considerably affect the performance because the existing placed muscles would be kept as static rigid objects and only the data structure for collisions would grow in size. Performance would drop if multiple muscles would be moved at once.

For the placement part the material used is the isotropic StVk, while for the contraction preview it switches to anisotropic. After the bicep is placed by translating and rotating its handles in a position which resembles its real anatomical position on the character, the user sculpts its central body by making it much bigger and finally previews its new shape in an animation that activates the contraction (5.6).

In terms of performance, one muscle made of 400 tetrahedra, subject to 15 hard constraints and 100 collision constraints, interacting with one bone and one other muscle, can be placed interactively at $\sim$15 fps using a timestep of 0.01s. Because the accuracy in this kind of design applications is secondary over performance, the parameter or the maximum number of iterations performed by the PCG solver was kept low (10-20).

The next chapter presents a procedural technique based on continuous scalar fields that doesn't use physics, but allows the addition of wrinkles as a post-process effect.

Chapter 6

Implicit Skinning Extension

6.1 Introduction

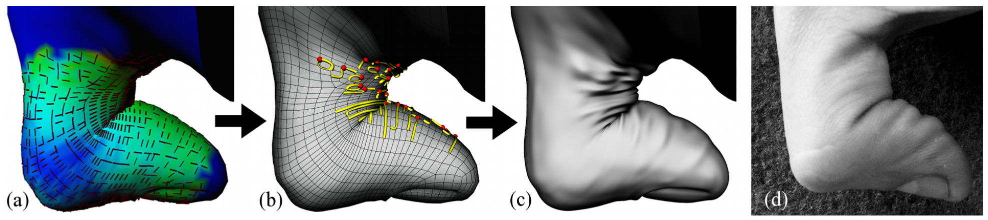

Figure 6.1: *Overview of the workflow of the system. (a) Angle field gradients; (b) Seeds and curves; (c) Final result (meshes are subdivided); (d) Real example of a left thumb.*

Skinning is one of the most important areas in the field of computer animation and visual effects, where character realism and believability are essential. A large number of methods exist and are implemented in modern animation systems (Gain & Bechmann 2008). One of the recent advancements in the area which produces believable results is the Implicit Skinning technique (Vaillant et al. 2013). Unlike other methods which only use surface (vertices and triangles) data, Implicit Skinning makes use of implicitly-defined continuous scalar fields, in particular Hermite Radial Basis Functions (HRBF). This helps in solving the drawbacks that linear blend skinning and dual quaternion skinning exhibit: loss of volume, lack of collisions and unwanted bulging.

During animation, the fields associated with each skeleton bone are rigidly transformed and the mesh vertices march in the direction of the gradient of the combined field until they reach the isovalue they had in the rest pose. This allows better preservation of the initial shape and better deals with self collisions in the folding region, either by stopping the marching at gradient discontinuities or by using a contact operator (Vaillant et al. 2014). The framework also allows the creation of interesting effects through the use of gradient-based operators, for example the bulge in contact which approximates volume preservation. Nevertheless, to the author's knowledge, important secondary effects such as wrinkling have not been previously investigated for this technique.

In this chapter it is described the extension of implicit skinning to generate plausible and temporally-coherent wrinkles for skeleton-driven 3D animated characters. The technique benefits from the available transformed scalar fields: from their interaction a vector field that resembles plausible wrinkle directions is generated, hence creating a hybrid polygon-implicit approach.

The main contributions of this work are:

1. A technique for the creation of wrinkle curves based on the implicit skinning method.
2. A large set of parameters to allow users to procedurally tune the behaviour of the wrinkles and thus obtain the desired result.

6.2 Related work

Despite being considered a secondary effect in skin simulation systems (Clutterbuck & Jacobs 2010), wrinkling has been attracting the attention of both academia and industry as an important detail to add realism to Computer Generated (CG) characters. Elastic thin sheets like cloth or skin create wrinkles when compression forces are applied, to preserve material and isometry (the property of being inextensible) of the rest-pose object.

Current approaches can be categorized as artist-driven, in which drawn wrinkles maps are blended (Jimenez et al. 2011), procedural, based on textures (Kimmerle et al. 2004), and physics based, often using a bending energy formulation in a specialized cloth solver (Bridson et al. 2003). An accurate way to measure stretching and compression is via the stretch tensor as presented in Rohmer et al. (2010). Their work is focused on augmenting coarse mesh cloth simulations with fine details such as wrinkles and refining the tessellation in localized areas through adaptivity. The rest mesh is parametrized to a plane in order for the triangles to have a common frame of reference and the stretch tensor is calculated as defined in (Talpaert 2010). This is then diagonalized and its eigenvalues and eigenvectors give the magnitude and direction of the wrinkle vector field, respectively. Wrinkles are then generated as convolution surfaces from this field's streamlines by growing curves from seeds with the highest vector magnitude. The technique presented in this chapter follows the same procedural approach for curve generation but substitutes the stress field by the gradient of a scalar angle field, without using planar parametrization. In this way the properties of the fields are exploited instead of calculating the stress tensor.

Recent works on skin in particular make use of physics-based simulation. Rémillard & Kry (2013) presents an approach in which thin shells are embedded in coarser finite element meshes to simulate the wrinkling effects of hard skin surrounding soft objects. The key idea is the use of frequency based position constraints, modelled as discretized continuous functions, that allow wrinkle formation only at wavelengths matching physical material properties. The work by Li & Kry (2014) extends this technique by adding multi-layer support for heterogeneous materials and creating extremely fine and realistic skin details trough the use of adaptive meshes, for which normal or displacement maps can be exported. Warburton (2014) in his work successfully applies a variation of the Finite Element method to the simulation of realistic forehead wrinkles on the GPU. Wrinkles as part of a larger simulation framework were presented in Weta's proprietary Tissue system (WETA Digital 2013) that uses finite elements to simulate fascia/fat/skin layers and constraints to solve wrinkling problems.

Biomechanics and bioengineering studied in depth the phenomenon of wrinkling on human skin. Joodaki & Panzer (2018) review its general properties such as nonlinearity, viscoelasticity, anisotropy and loading history dependency, in addition to specific constitutive material models. Lejeune et al. (2016) derive an accurate analytical solution for the prediction and control of multi-layer wrinkling initiation. Yin et al. (2010) study the behaviour of wrinkling due to water immersion and in particular wrinkle-to-wrinkle distance (wavelength), wrinkle depth (amplitude) and critical wrinkling stress/strain. They compare an analytical and a FEM method to evaluate predictions. The consequence of aging on the skin was studied by Flynn & Mccormack (2009), who use a multi-layer FEM model to simulate the effect of changes in physical properties such as moisture content and dermal collagen fibre density. Paes et al. (2009) investigate the reasons for the differences of wrinkling in the mouth region between men and women, at the histological (tissue) level.

6.3 Method

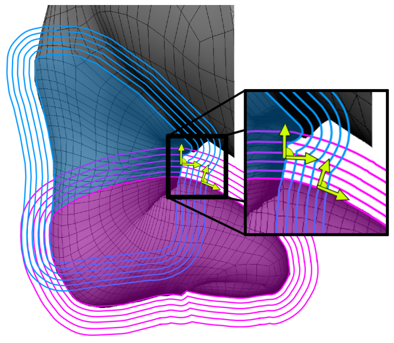

Figure 6.2: *In pink f_1 and blue f_2, two HRBF fields; angles between their gradients are shown in yellow.*

The method presented here works in the Implicit Skinning framework (Vaillant et al. 2013), as a post-process following the projection step that moves the vertices to reach their rest-pose isovalue. The following subsections detail the steps to generate plausible wrinkles for a mesh deformed with the implicit skinning algorithm. The required inputs are therefore the continuous scalar fields of the segmented mesh of which value and gradient are used.

The method is based on the post-processing technique presented by (Rohmer et al. 2010). The difference with their approach is that here the stretch tensor is replaced with a discrete scalar field calculated from the single fields associated with each bone. Its value at each vertex is defined as the angle between the gradients of two adjacent fields. This avoids the parametrization of the mesh in planar space while taking full advantage of the implicitly-defined scalar field. The key observation is that the gradient of this angle field resembles the direction in which human skin wrinkles in bending fingers or arms.

6.3.1 Angle Fields Preparation

The vector field representing wrinkle directions, constrained on the surface, is a gradient field of the discrete scalar angle field and it is calculated by taking the finite differences in the local frame of each vertex. In practice, for production-ready meshes, it can be approximated by taking the finite differences on the one-ring neighbours of the vertex, as described below.

The generation of a discrete scalar field for each pair of adjacent joints in the skeleton hierarchy will now be defined formally. Let f_1 and f_2 be two consecutive fields with compact support. During animation of a bending joint chain f_1 and f_2 will rotate rigidly towards each other. For each vertex in $f_1 \cap f_2$ the angle between the gradients of f_1 and f_2 can be calculate straightforwardly as (see Figure 6.2):

$$angle(f_1, f_2) = \arccos\big(\nabla f_1 \cdot \nabla f_2\big)$$

where gradient vectors are assumed to be normalised.

Once an angle field f_A is defined, its gradient is approximated with finite differences by searching in the one-ring neighbours the position with minimum value p_{min}. For a source vertex p the gradient is then:

$$\nabla f_A = p_{min} - p$$

In practice, the user can choose to use a version of this field in which the gradients are biased towards one of the connected edge vectors. Based on the quality of the deformed topology, in this way more regular anisotropic patterns can be achieved if desired (Figure 6.3. To generate fields less dependent on the mesh resolution the search can be done in ring neighbours of levels greater than one, which are pre-stored for efficiency. Considering three hierarchical fields f_1, f_2 and f_3 in which f_2 is child of f_1 and f_3 child of f_2, they can interoperate in such a way that f_1 can create wrinkles with field f_2, but not with f_3.

6.3.2 Curve Creation

The wrinkle curves are grown from the potential seeds selected from the vertices satisfying the user-controlled parameters and which are processed in a priority queue based on their associated angle. For each new seed a curve is grown in both the directions determined by the maximum gradients of its surrounding neighbours. Temporal coherence is achieved by keeping curves from the previous frame and deleting them if their corresponding seeds do not satisfy specific criteria for the current frame.

Depending on the extension of the local support of the implicit skinning fields, wrinkles could also appear both in the rest pose and on undesired regions of the mesh. This problem is solved by creating a seed only if the corresponding joint is bent more than a specified threshold. In addition, a subset of the initial vertices is precomputed by excluding those not in the folding region. This is obtained by thresholding based on the dot product between the vertex normal and the up vector of the associated bone's local rotation frame. Finally, the vertices forming a curve are displaced in their normal direction by a controllable amount. This approach works for both static frames and animations.

At each frame every vertex is processed and inserted in a priority queue based on its angle value. The curve generation algorithm begins by selecting a seed from the top of the queue (red dots in Figure 6.6(d)); starting from it, vertices are added to the curve by iteratively choosing the next candidate in the one-ring neighbourhood N that has edge vector most similar to the gradient of the field at the source point. This process is repeated for the newly added point.

As in (Rohmer et al. 2010) the curve is grown in both directions, with the addition that for each seed we invert the gradient at that point to grow the second half of the curve. By indicating with q a candidate neighbour and by $\mathbf{e} = q - p$ the edge vector, the next vertex to add to the curve is calculated as:

$$p_{next} = \min_{q \in N}(\arccos\big(\mathbf{e} \cdot \nabla f_A))$$

after normalizing vectors in arccos. The generated angle field has gradients pointing in plausible wrinkles directions because the angles decrease moving further away from the folding region, where their values are similar to the joint bending angle.
Every time a new point is added, its Euclidean distance is checked against all the current curves to enforce the constraint that all of them must stay at a minimum user-defined distance. The curve points loop terminates when a point's angle is under a user-set threshold or when it ends up outside of the allowed internal region of the mesh. Due to the fact that for dense meshes the number of curve points can be high and would negatively influence performance, a resampling of the curve can be performed which in practice corresponds to a simple pruning.

In order to maintain temporal coherence between consecutive frames, the active curve list is kept from one frame to another and a curve removed from it if its corresponding seed ends up outside one of the associated fields, which can be defined by checking the isovalue against the threshold. Therefore the curves are not grown again from their associated seed after they are generated. This is in line with the observation that for human skin in particular, wrinkles tend to form at the same position for multiple repetitions of the same movement (fingers are a typical example), a feature exploited for instance by Cao et al. (2015) for their wrinkle likelihood map generation.

During animation, fields rigidly rotate and interpenetrate one another which causes configurations for which a field (the one associated to a finger phalanx for example) happens to be "immersed" into another field. This becomes problematic because seeds will be selected from the whole mesh segment and wrinkles would appear in unwanted regions, like the nail. Therefore, as a precomputation step, only the vertices on the same side of the joint bending direction are selected for wrinkle generation. This is done easily by thresholding based on the dot product between the vertex normal and the up vector of the associated bone's local rotation frame.

6.3.3 Wrinkle Field

The curves created as described in section 6.3.2 are a set of line segments connecting vertices of the mesh. These segments are transformed into convolution surfaces w_i and the sum of their field contributions gets thresholded:

$$v_{wrinkles} = \sum_i (w_i) - T$$

In this method the convolution surfaces used are with line segments as skeletons and Cauchy kernel as a potential function. This surface for line segment with position vector $\mathbf{a}_i$, normalized direction $\mathbf{d}_i$ and length l has the following closed-form formulation (McCormack & Sherstyuk 1998):

$$w_i(\mathbf{x}) = \frac{n}{2p^2(p^2+s^2n^2)} + \frac{l-n}{2p^2q^2} + \frac{1}{2sp^3}(atan[\frac{sn}{p}] + atan[\frac{s(l-n)}{p}])$$

where $n = (\mathbf{x} - \mathbf{a}_i) \cdot \mathbf{d}_i$, $p^2 = 1 + s^2(|\mathbf{x} - \mathbf{a}_i|^2 - n^2)$ and $q^2 = 1 + s^2(|\mathbf{x} - \mathbf{a}_i|^2 + l^2 - 2ln)$
The following default parameters (empirically chosen) are used for the convolution surface: $T = 0.5$ and $s = 0.85$.

The advantage of using convolution surfaces is that the segments smoothly blend-in and they can be integrated straightforwardly with the existing HRBF fields. Because there is no stretch information per face in this method, the radius of each segment gets modulated by a factor that depends on the angle magnitude at each curve point. This in general makes the wrinkle thicker at the center of the field and smoothly narrower at the edges. For fast value query each segment's bounding box is also inserted in a KD-tree.

6.3.4 Projection

After obtaining vertex positions from the last step of implicit skinning and wrinkle fields $v_{wrinkles}$, the HRBF field and wrinkles field are combined. Thus, the value v_{comb} at an arbitrary point p_w is:

$$v_{comb}(p_w) = \max(v_{HRBF}(p_w) - 0.5, \;\; v_{wrinkles}(p_w))$$

It can be seen that here a simple set-theoretic operation is used, yet more complex blend operators can be adopted as well. Vertices get projected to this combined field by using Newton's iterations (Figure 6.4). During projection collisions are not calculated using gradient discontinuities. Instead, to avoid evident mesh interpenetrations, the smoothing coefficients generated in the main implicit skinning step are reused to exclude from the displacement the vertices in the colliding folding region.

Unfortunately the equivalence between the decomposed stretch tensor's eigenvalues and the angles magnitude cannot be used to activate the wrinkles because already in the rest-pose the angle values are not zero and during animation noisy fluctuations in the angle field are experienced. Therefore, in order to produce a smooth appearance for the wrinkles, the depth of the curve is modulated by the offset between the current and the rest-pose's joint activation angles, in a fashion similar to how a pose-based deformation works. The gradual appearance is achieved by placing the curve vertices initially under the surface at a distance R corresponding to the radius of the segment and smoothly moving them upwards in the normal direction.

For fast preview purposes, a simplified procedure can be applied. Instead of projecting the vertices to the wrinkles field, a simple displacement of the vertices corresponding to the curve points can be executed. However in this case the wrinkles radius is not controllable and wrinkles appear to be too sharp and uniform.

6.3.5 Parameters

The presented system is procedural and allows the user to control the appearance of the wrinkles by tweaking basic parameters (see Figure 6.5), some of which are described below (please refer also to the videos at `http://www.fabioturchet.com/supplemental_material.zip`).

Wrinkle Radius: the base radius for the convolution surfaces

Direction Threshold: the minimum angle that the gradients at two consecutive points of a curve must form. This parameter helps to achieve a more organic look and longer wrinkles as it allows the curves to be approximately straight.

Seed Angle Threshold: the minimum angle that a seed point must have to be selected. This allows wrinkles to also start forming at the edges.

Field Threshold: minimum isovalue that a seed vertex must have to be selected

Angle Threshold: the minimum angle that any curve point must have; this controls the termination of the curve growth process

Seed Distance: keeps the seeds at a minimum Euclidean distance

Displace Strength: controls how deep the convolution surfaces stay under the mesh so as to modulate bigger or smaller displacements

Ramp Control: a smooth spline that controls how fast and linear the wrinkle appearance is

Appearance Time: activation time, expressed in frames or joint angle degrees

Topology Bias: this parameter forces the angle field calculation to examine only the connected vertices.

6.4 Implementation and Results

The method is implemented as a C++ Maya 2015 plugin. Both value and gradient of the rest-pose HRBF fields are stored as OpenVDB textures because their evaluation is computationally too expensive as it requires solving a linear system per frame. This means that at each frame the HRBF field is not recomputed but the inverse matrix of the joint transformations is used instead to read the value in the rest-pose.

As the angle calculation is independent per vertex, this step can be parallelized. The angle field computation and the vertex projection are in fact multi-threaded, but could also be implemented on the GPU, for example using the Fabric Engine framework (Fabric Engine 2015). The code could be further optimized, but performance highly depends on the number of iterations in the projection steps which in turn determines the number of accesses to the textures. On a quad-core Intel Xeon X3470 machine, for the thumb mesh with 15K vertices, 15 curves and 4 joints the framerate is $\sim 10fps$ (including implicit skinning projection and smoothing).

Tests of the technique were conducted mainly on cylindrical objects such as fingers, arms and legs and achieved believable results. Figure 6.6 shows the detail of a thumb which is particularly interesting due to the various wrinkle patterns of different sizes. This example uses constant radius and the field used is the non biased one: note how the curves develop independently of the mesh connectivity because of the higher degree of freedom in terms of possible neighbour directions.

Even though the technique does not always produce full wrinkle curves from one edge of the finger to the other (due to discontinuities or noise in the field), it still creates an organic and believable look. Note the use of the smoothing coefficients to avoid wrinkle displacement where vertices collide (Figure 6.6 (e)). The patterns are comparable to a real example (Figure 6.6 (f)). Moreover, close wrinkles are blending in quite naturally because of the convolution surfaces formulation. Figure 6.7 shows comparative results between biased and non biased fields for the mesh of an arm: the topology-biased field produces more believable wrinkles.

In some cases unwanted bulges can appear: this is due to curves which are too short or whose curvature is too high in some of their segments. This could be addressed by filtering out these cases from the final used set. In addition, it was noticed that the 3D texture resolution can strongly condition the quality of the angle fields due to interpolation approximations. In general better results were achieved using 4 or more ring-neighbour levels, especially for high resolution meshes; even though this improves the accuracy of the vector field, it also consequently slows down the system because more vertices have to be processed.

During animation the technique behaves as expected in terms of temporal coherence, with wrinkle curves that do not pop between frames and slide thanks to the underlying deformation. If the curves were retraced at each frame from the seeds, the result would be unstable and non coherent, mainly because of the differences in two temporally consecutive fields.

Nevertheless, the behaviour of the technique during animation could be further improved. Dynamic appearance is still not convincing enough, in fact the wrinkles appear too suddenly: this could be improved by tweaking the activation curve manually or deriving it from experiments. Self collisions between the convolution surfaces (using a bulge-in-contact operator) would also prove beneficial to the overall fleshy look and dynamism of the deformation. The reproduction of properties of the skin, such as the ones due to aging, have not been considered yet and constitute interesting direction for future work.

The validation and evaluation of the technique has been done at the visual quality level and not through rigorous objective comparisons with physical based models as some of the work presented in section 6.2. Accurate measurements of visual quality such as local wrinkle density and height from previous work and from images of real skin would help to evaluate the model more objectively. To validate the system further at a more general level, it would be ideal to survey artists feedback in the testing and reproduction of different wrinkle patterns. The variation could come from photographs of subjects in different poses and facial expressions of varying gender and age.

In this chapter a technique that allows wrinkles creation within the Implicit Skinning framework has been presented. The technique creates convenient and plausible results visually similar to the ones obtained with physically accurate stretch-based methods. The results show the potential of the technique for applications within a production pipeline. The next chapter presents the last project of this thesis. Its goal is to apply machine learning to the simulations of deformable objects in order to save computation time and substitute the solver in controlled constrained scenes with a GPU-based Deep Neural Network.

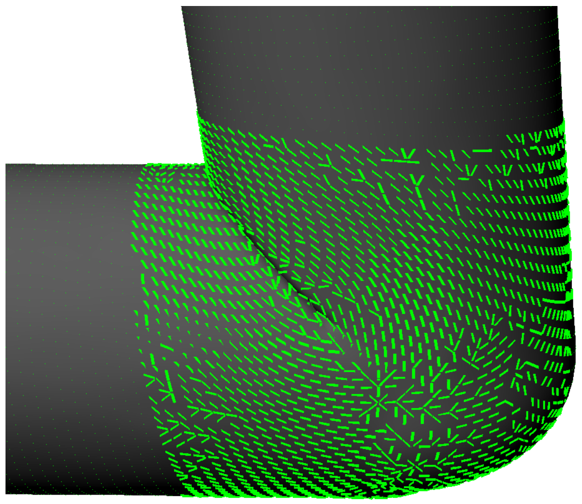
(a) *Original angle gradient field*

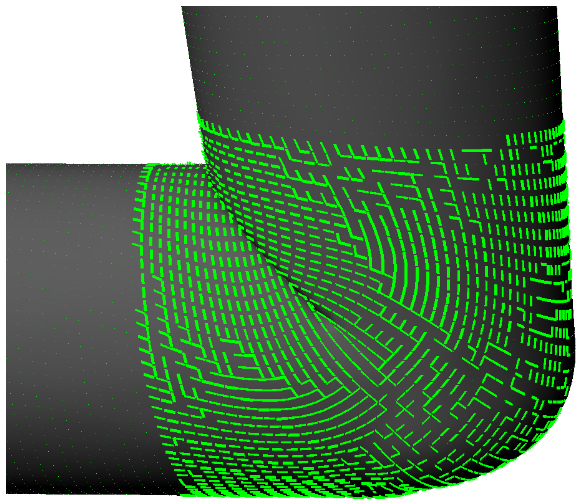
(b) *Topology-biased gradient field*

Figure 6.3: *Angle field generation using one-ring neighbours (a) and connected vertices (b).*

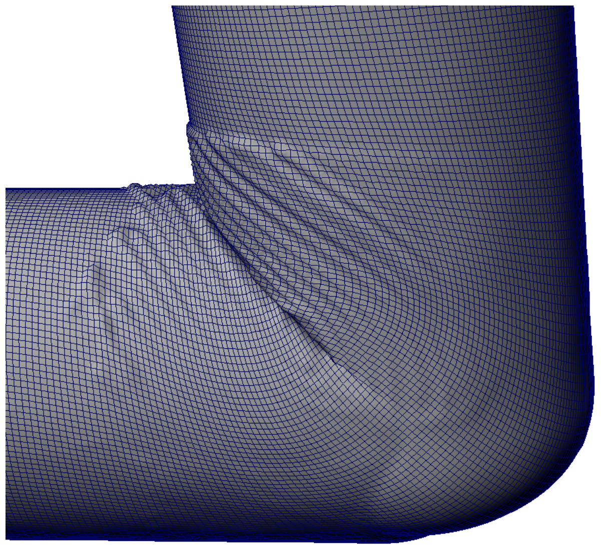

(a) *Original field's wrinkles*

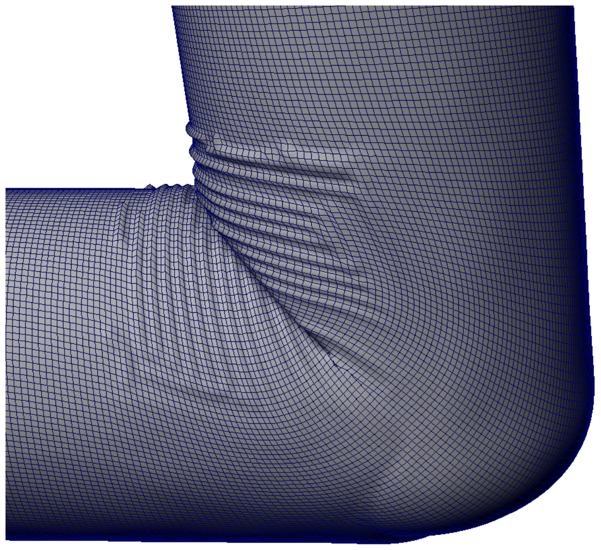

(b) *Topology-biased field's wrinkles*

Figure 6.4: *Wrinkles generated from the fields in Figure 6.3.*

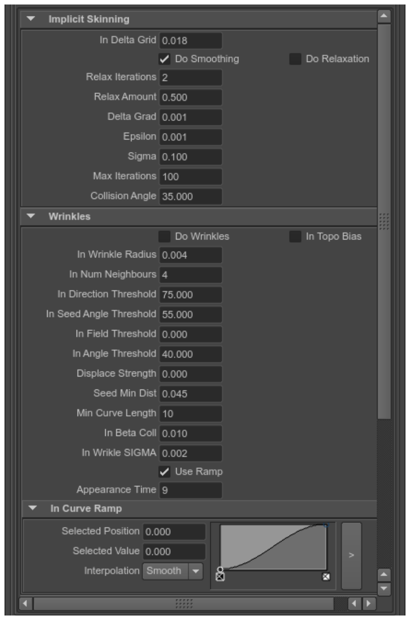

Implicit Skinning

In Delta Grid 0.018
✓ Do Smoothing
Do Relaxation
Relax Iterations 2
Relax Amount 0.500
Delta Grad 0.001
Epsilon 0.001
Sigma 0.100
Max Iterations 100
Collision Angle 35.000

Wrinkles

Do Wrinkles
In Topo Bias
In Wrinkle Radius 0.004
In Num Neighbours 4
In Direction Threshold 75.000
In Seed Angle Threshold 55.000
In Field Threshold 0.000
In Angle Threshold 40.000
Displace Strength 0.000
Seed Min Dist 0.045
Min Curve Length 10
In Beta Coll 0.010
In Wrikle SIGMA 0.002
✓ Use Ramp
Appearance Time 9

In Curve Ramp

Selected Position 0.000
Selected Value 0.000
Interpolation Smooth

Figure 6.5: *Plugin Parameters.*

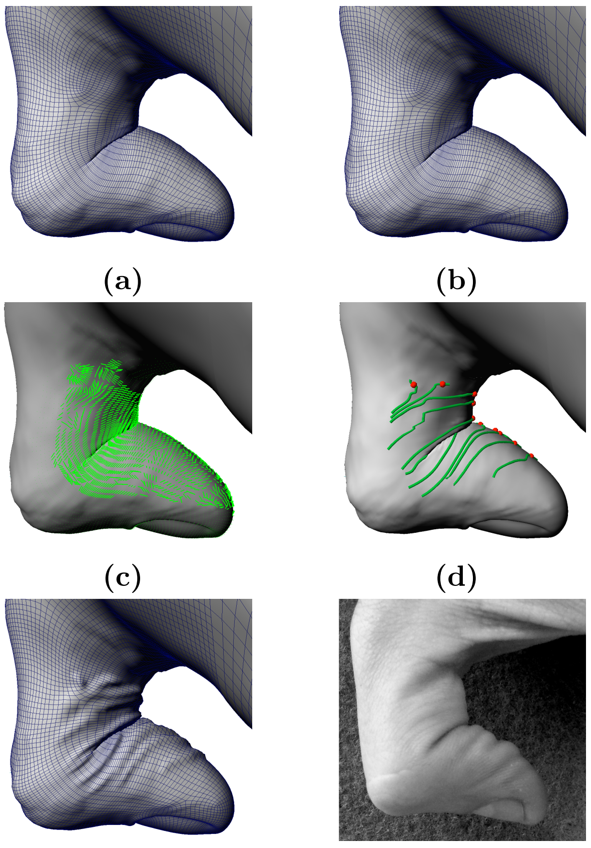
(a) **(b)** **(c)** **(d)** **(e)** **(f)**

Figure 6.6: *(a) Default Dual Quaternion skinning; (b) Implicit Skinning; (c) Angle gradient field (non biased); (d) Seeds and curves; (e) Wrinkles after projection; (f) Picture of a real thumb.*

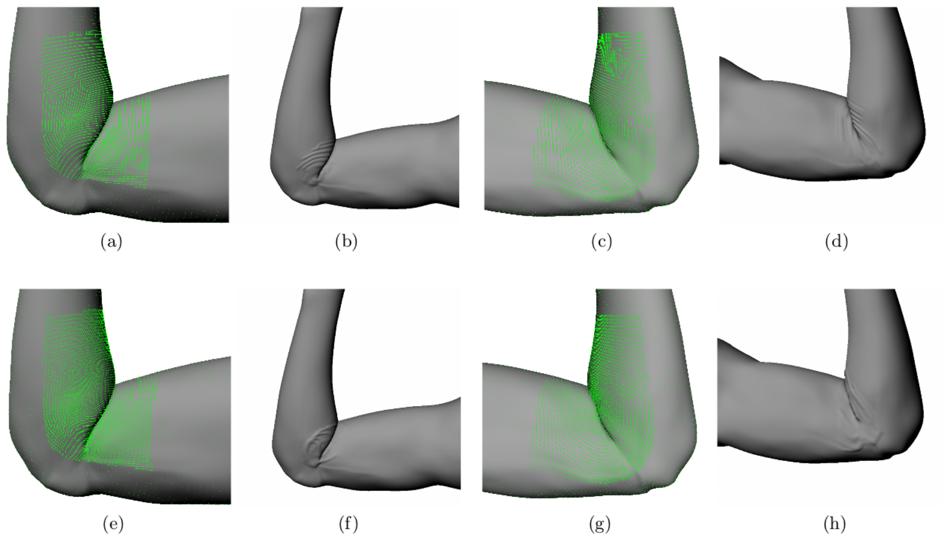

Figure 6.7: *Comparison of the results obtained for an arm. (a)-(d) front and back views using topology biased field; (e)-(h) front and back views using normal, non biased field.*

Chapter 7

Pilot Study on Deep Learning for Deformable Objects

7.1 Introduction

The work presented in this chapter describes how Deep Learning architectures can be applied as powerful regressors to the prediction of physics states for elastic objects, accelerating and potentially substituting traditional physics solvers. In modern physics-based animation elastic objects are simulated using the Finite Elements Method by solving Newton's differential equations of motion in the form of a sparse linear system. Typically Preconditioned Conjugate Gradient is used for this task. Even though state of the art methods that are both fast and stable exist (Bouaziz et al. 2014), a data-driven approach could be a competitive alternative.

The initial purpose of this project was to first understand how to learn a model to express the dynamics of a physics-based cloth animation with constraints in the form of a toy problem. After that first stage the goal was to extend the system to support volumetric (tetrahedral) objects and apply convolutional neural networks to the learning of constrained muscle simulation. The motivation driving the project was that a cloth simulation is in general very detailed and fast changing while muscles deform in a much more stable manner therefore they would be easier to learn by a machine learning algorithm. It will be shown how solving the first stage turned out to be very problematic (due for instance to the novelty of application of the geodesic convolution) and the complexity of the recalculation of one of the inputs of the network hindered the advancement to the second stage for volumetric objects. These challenges paved the way to an understanding of the main limitations of the proposed approach and the solutions that will constitute the future work.

7.1.1 Background

Here a brief introduction to neural networks terminology is given for a much more complete reference please refer to Andrej Karpathy (2017).

A Neural Network (NN) is a set of interconnected units called *neurons*. Each neuron's job is to output a value by multiplying its inputs by a weights matrix (which constitute the learnable parameters) and passing the result through an activation function which is nonlinear (examples are the *sigmoid*, *softMax*, *tanh*, *ReLU* functions). This nonlinearity is what allows the network to learn complex real world functions: a NN can be in fact considered a universal functions approximator which finds patterns in complex unstructured data.

In terms of architecture, a NN is an acyclic graph and neurons can be grouped and organized in layers. In a layer connections are not between the same layer's neurons, but between layers. When all neurons of one layer are pairwise connected to the ones of the next layer, it is called a fully connected layer (FC). Apart from input and output layers, the ones in the middle are called hidden layers and the fact that they can be cascaded and be many in number gave rise to the term *Deep* Learning.

At each layer the network learns to represent internally some features of the input and deeper layers learn a hierarchical representation of high level global features. In the case of images of faces for example, in the early layers simple contrasted edges are detected while in more deep ones these edges are assembled in more meaningful patterns corresponding

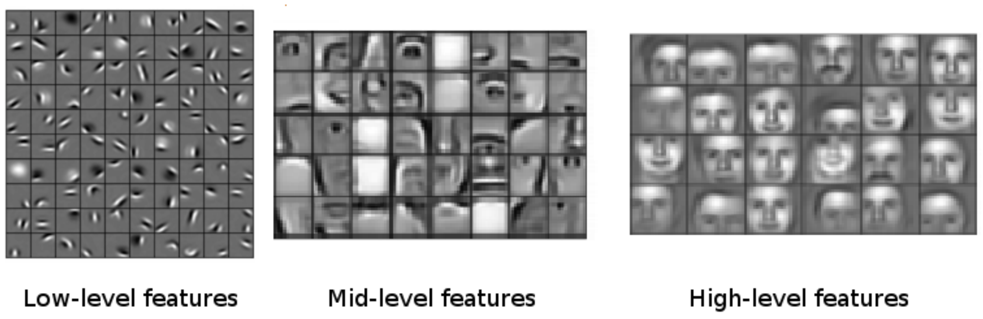

Figure 7.1: *Lee et al. (2011)*

to features such as ear or nose and even further down the full face is considered as a global abstract feature (Figure 7.1).

A particular kind of NNs are the so called Convolutional Neural Networks (CNN) created to make the learning of input images very efficient. They are based on the assumption that an image should be analysed spatially and not interpreted as a linear vector with no relation between neighbouring pixels. To this end the convolution operation takes the input and uses *filters* with kernel weights and extracts the activation of this filters by sliding them as a window across the image. This operation is defined mathematically (Goodfellow et al. 2016) and the filter weights constitute the learnable parameters. The layers of a ConvNet are in 3D (width, height and depth) and each layer transforms 3D input volumes to 3D output volumes of neuron activations.

A CNN learns by performing a sequence of forward and backward passes. The goal of the NN is to minimize a loss function (in literature also called cost, or objective function) which is peculiar to each problem and represents the error that should be minimized. In the forward pass the network takes an input and passes it through its layers; based on the filters that it learned during training some neurons will be excited and activate more than others and their contribution will globally produce an output. For a classifier this could be as simple as telling if an image belongs to Dogs or Cats classes and with which probability. In the backward pass the actual learning happens (called *backpropagation*). The gradient of the loss function with respect to the parameter weights (partial derivatives) is computed given a training input sample and it is used by algorithms such as Stochastic Gradient Descent (SGD) to understand in which direction the function decreases. ADAM is a very popular variation of this algorithm (Kingma & Ba 2014). From the output layer back to the first hidden layer the filter weights are therefore updated in such a way that the loss function is minimized. This constitutes the training process and is repeated a certain number of *epochs* (in an epoch all the training samples are processed by the network).

One of the main problems when doing machine learning is the risk of a behaviour commonly called *overfitting*: this happens when the network learns the training data very well but performs poorly on the new test data. There are many techniques that go under the common class name of regularization which are used to try to avoid this negative effect. *L2 regularization* for example penalizes the squared magnitude of all parameters directly in the loss function. *Dropout* (Srivastava et al. 2014) instead consists in keeping a neuron active during training only with some probability p and setting it to zero otherwise (effectively disabling it). Another technique is called *early stopping* which consists in terminating the training process when the accuracy of the test set starts to diverge. This behaviour is clearer if looking at the curve plots shown in the following sections (for example Figure 7.9): when the accuracy and training cost curves are closest or intersect, the corresponding epoch is the one to stop at. Because in this work's implementation the weights are saved every time there is progress in the minimization of cost, they can be chosen manually by looking at the curves over a longer number of epochs.

Recurrent Neural Networks (RNN) are a version of NN particularly indicated for time-sequences. They contain a feedback loop: the input of the network is not only the one at current time t but also the one of the hidden layer at previous time $t - 1$. This allows the network to have a "memory". The learning process is now time-dependent and it is performed via backpropagation through time (BPTT).

7.2 Related Work

Machine Learning is nowadays ubiquitous. The main tech companies such as Google, Apple, Microsoft and Facebook use machine learning and other methods in artificial intelligence as a core of their technological solutions. A subclass of Artificial Intelligence called Deep Learning has been having an extraordinary growth in recent years thanks to the availability of implementations that run on distributed and affordable parallel Graphics Processing Units (GPUs). This approach makes neural networks algorithms applicable on huge datasets in acceptable computational times, something that was not possible before. Almost every field in the Sciences can benefit from the generalisation power of deep convolutional neural networks (CNNs), including computer graphics.

Existing work that applies Deep Learning to geometrical objects deals mainly with their volumetric representation as voxels (Wu et al. 2014), but the main drawback of this method is its extremely high memory footprint while using models with relatively small details, which is normal for Games and Visual Effects. In particular it will be shown how a convolution can be performed on vector and scalar fields defined on deformable geometries. This is a non-trivial operation which requires a custom technique based on geodesic disk filters (Masci et al. 2015a). After describing how the dataset is generated, an architecture of a regressor implemented as a Deep Neural Network in Theano is presented, inspired by recent work on fluid simulation (Tompson et al. 2016). This network is applied to the prediction of cloth simulations and ideas on how the technique could be extended to volumetric tetrahedral deformable objects are discussed. For an in-depth survey and course on geometric deep learning please refer to Bronstein et al. (2016).

The core of the method is the definition of the loss function to be minimized. Two such functions are considered in this work: the first makes use of supervised learning (ground truth) and calculates the squared error for predicted velocities and positions. The second is an unsupervised approach which is derived directly from the variational Implicit Euler formulation (Martin et al. 2011) for the integration in time and takes

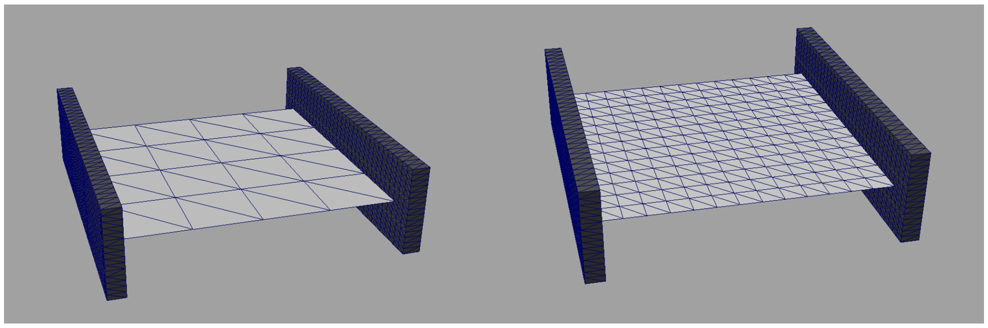

Figure 7.2: *Low and high resolution plane geometries used for the dataset creation, with constraining objects on two of the sides.*

into account both elastic and inertial forces. In addition to the version with geodesic disks, another approach to the problem that makes use of standard convolution on images was used. In this later approach positions and velocities are triplets defined per node which are interpreted as RGB colours and "flow" at each frame over a grid defined by the UV textures coordinates in 2D.

7.3 Dataset

As initial test, a relatively simple example was chosen: a cloth simulation of a square shape mesh. The dataset which was generated for this initial example is prepared accordingly. Two versions of a testing object were prepared: the low-resolution mesh and the high-resolution mesh. The rationale behind these two versions was that the low version is much faster to compute and to prototype the loss functions. On the other hand the high resolution version presents much more interesting details (i.e. wrinkles) but they are also harder to learn. The low resolution version has 25 vertices, 10 constraints and 32 triangles. The high resolution one has 196 vertices, 28 constraints and 338 triangles (Figure 7.2).

The plane is simulated as a cloth with animated pinned vertices (hard constraints) using the solver for triangular element meshes of Chapter 3 without collision objects or self-collisions. Various animations of the left, right or both constraining geometries (handles) are generated in Maya and constitute a scene. Each scene has random translations and

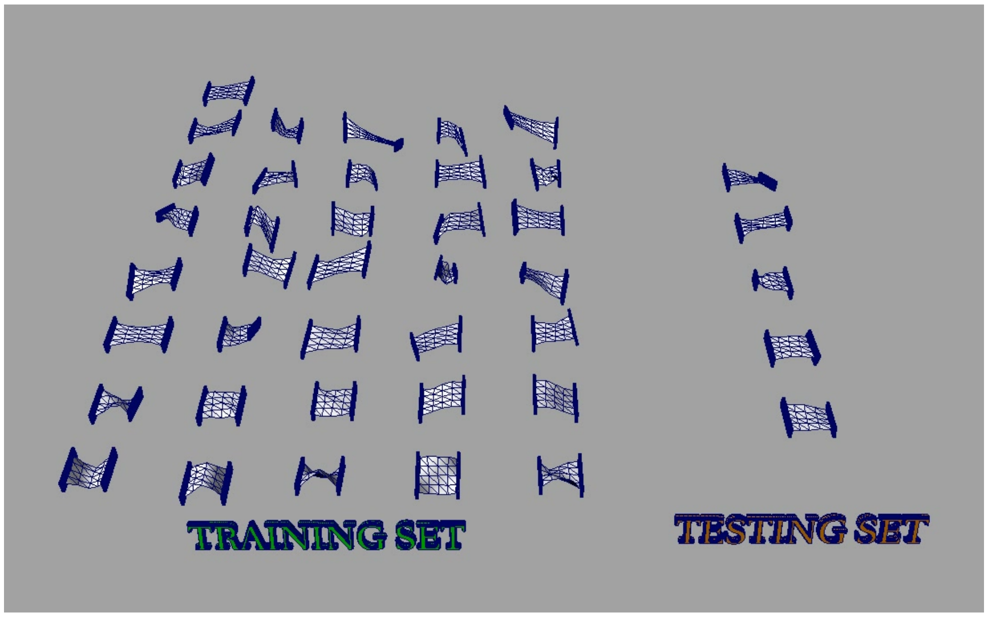

Figure 7.3: *One frame of the animations for the scenes of the dataset.*

rotations of the handles sampled from a defined range (Figure 7.3).

For the low-res version the dataset was split into training and testing sets as follows:

- 36 scenes of 350 frames each
- Training: 12600 frames, sampled every 2 (6300 frames)
- Testing: 350 frames

For the high-res instead:

- 21 scenes of 350 frames each
- Training : 7350 frames, sampled every 2 (3675 frames)
- Testing: 350 frames

The number of frames differs because the high resolution version is much more computationally expensive. In a preprocessing stage, for each scene and for each frame, positions and velocities of the vertices are saved out to file to be used in the training as feature descriptors.

It is common practice in machine learning to preprocess the data in order to facilitate the training task (data normalization). To this purpose the global mean and standard deviation on the six x,y,z coordinates of position and velocity were calculated from all the samples of the training set, then from each sample the mean was subtracted and the result divided by the standard deviation. However for this specific problem the data normalization did not improve the results therefore the dataset was left as it is.

7.4 Architecture

The network architecture consists of 3 Convolutional layers (CL) followed by a Fully Connected layer (FCL) used to reshape the output dimension. The number of filters (output channels) are 64, 128 and 128 for the first, second and third CLs respectively and 3 for the FCL (Figure 7.4).

Each CL uses Rectified Linear Units (ReLU) as activation functions. Max pooling was not implemented because the meshes are not very high resolution and also because it would imply using a decimation algorithm between the layers.

The input of the network is a tensor data structure (multi-dimensional array) of dimension [number of vertices, 6], obtained as the result of the stacking of two matrices of dimension [number of vertices, 3] representing the x,y,z components of positions and velocities. In the case of the Recurrent Neural Network (RNN) implementation, the input includes the time dimension and is a tensor of dimension [sequence length, number of vertices, 6]. The first 3 channels are the positions and the ones from 4 to 6 are the velocities (x,y,z components). Given the input at frame t, the output produced by the network is a tensor of dimension [number of vertices, 3] representing the predicted velocities of the nodes at frame $t + 1$ which are used to compute the new predicted positions.

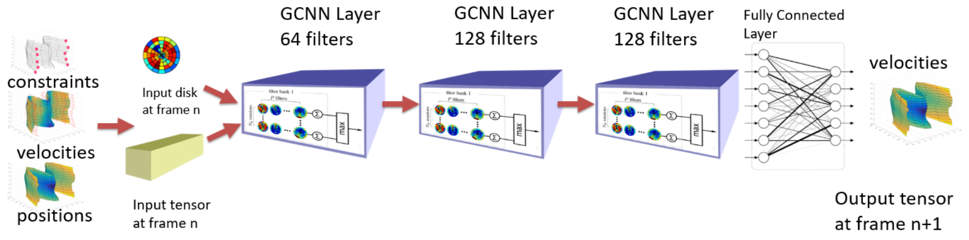

Figure 7.4: *Architecture of the convolutional neural network.*

7.4.1 Method based on images / UV

One way to allow a neural network to perform learning on deformable objects is to consider the deformation happening in the 2D parametric space instead of 3D world space. This solution was considered to remove the dependency on the disks (described in the next subsection) which is a heavy precomputation step and also slows down the training process. Exactly like the dual and equivalent approach used in fluid simulation (Eulerian and Lagrangian views), here the UV (or texture) space is considered as a grid of points on which the deformation "flows" in the form of position and velocity quantities. Therefore every frame of the simulation is equivalent to an image having 6 channels (position and velocity for x,y,z) changing over time on a fixed UV coordinate space. Figure 7.5 shows an example of velocity input image overlaid on the UV mesh. An alternative representation was considered as shown in Figure 7.6: each vertex of the UV grid constitutes a solid cell without colour interpolation in the style of Voronoi graphs. Even though this version is in theory easier for pattern detection and explicitly expresses that the information is associated to the mesh nodes, the efficiency of this version was comparable with the interpolated one while additional effort was required for preparing this representation. Therefore for all the presented examples the interpolated version was used.

This 2D representation makes the system independent of the disk inputs and allows taking advantage of very well established methods existing in Deep Learning for images. The neural network receives images as input and then the UV mapping is used for transferring the vertex dynamics

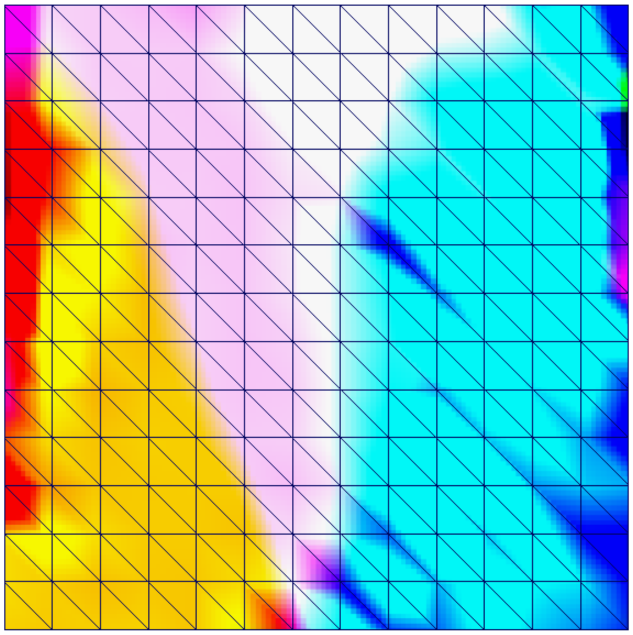

Figure 7.5: *Input velocity field in UV space*

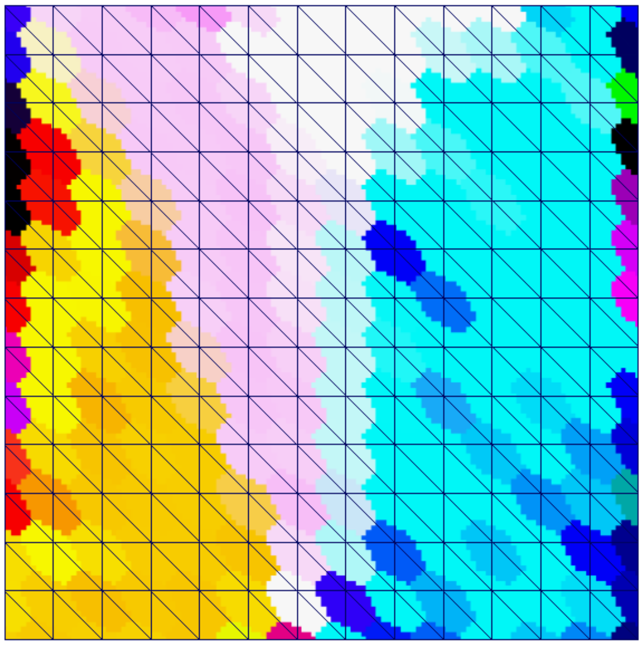

Figure 7.6: *Input velocity field in UV space in Voronoi style*

data from 2D image space to 3D world space coordinates of the vertices of the mesh. UVs can be assumed to be always present for an asset in a Visual Effects production and can be generated semi-automatically by modelling artists. This idea was tested and its results will be discussed in the following sections. The advantages over the version with disks are that it offers rapid prototyping, allows faster training times and resolution is more controllable.

7.4.2 Geodesic Convolution

The method described in the previous subsection makes use of standard convolution layers. In order to operate directly on geometries defined in 3D world space, this work adopts a custom version of convolution layers specialized for meshes, introduced in Masci et al. (2015a). Given a vector or scalar field defined on the vertices of the mesh, a geodesic disk (patch) is defined per-vertex as a set of spatial kernel weights in geodesic polar coordinates, by dividing the local neighbourhood into discrete bins. Geodesic distances are the real distances from point to point on a mesh for curved surfaces, as opposed to Euclidean distances which are just the magnitude of the vector connecting two points. This disk, when applied to the input field, extracts a local descriptor of it at a radius distance (patch operator) in the form of a sparse matrix. A layer that performs this kind of special convolution is called the Geodesic Convolution Neural Network layer (GCNN). The disks, because are defined by construction using geodesic distances, must be recomputed every time the mesh deforms. As will be shown, this is one of the main limitations of the method. In order to take advantage of the temporal coherence of the inputs, the network is equipped with a skip connection from the input to the output velocities: the input is summed to the predicted values so that it already gives a good initial approximation instead of being random, making the network learn de facto a velocity residual.

7.5 Cost Functions

The first basic cost function analysed here is the supervised single frame loss. It tries to minimize the squared difference between a prediction and the ground truth for positions and velocities given as input the pairs of values at frame t and $t+1$.

It is defined as:

$$f_{obj_{single}} = \lambda_p ||\mathbf{p_{t+1}} - \hat{\mathbf{p}}_\mathbf{t}||^2 + \lambda_v ||\mathbf{v_{t+1}} - \hat{\mathbf{v}}_\mathbf{t}||^2 + \lambda_r reg$$

where the "hat" symbol on position $\mathbf{p}$ and velocity $\mathbf{v}$ indicates a predicted value and reg is a regularization term. It represents the mean squared error (MSE) calculated on each vertex for which its contribution is averaged. λ symbols are multiplicative constants used to bias and weight each term. In the tests they take these values: $\lambda_p = \lambda_v = 1.0$ and $\lambda_r = 1e^{-}5$.

This function behaves well during testing only for the task of predicting single 'gap frames' in a sequence, but it is not sufficient to obtain predictions with high future accuracy because the error accumulates. In fact during the testing loop the output of the network becomes an input for the next prediction. This makes it an inherently ill-posed problem, given that an accurate ground truth for these future frames does not exist: the network never "saw" those examples because the input frame was generated by the model itself. If one wanted to use the correct ground truth, at each loop the predicted input should be passed to the real physics solver (used to generate the dataset) and advanced n frames from those new initial conditions. This is definitely not efficient during training time and would constitute a huge bottleneck; moreover it would require significant engineering effort given that the physics solver exists only as a Maya plugin, therefore this approach was avoided.

For the aforementioned reasons the objective function has to be extended to obtain better long-term accuracy. Four supervised approaches (described in the following sections) were developed and tested for this purpose:

- Future frames data augmentation
- Future frames partial derivatives accumulation
- Recurrent Neural Network
- SpatioTemporal convolution (for images version only)

All these objectives share the same limitations, as will be discussed in the following sections.

7.5.1 Constraints

Constraints, intended as imposed boundary conditions by the user on positions and velocities, play a very important role both in the simulation and learning phase. Initially they were modelled as zero-length spring energy potentials (see Chapter 4) so the system would penalize the squared distance between the predicted and ground truth positions if greater than zero. The problem with this approach for positional hard constraints is that because it is an extra energy potential term (defined in Section 4.3.4.1) added to the basic cost function's objective, there is the possibility that it will not be fully minimized. This means that the network could not completely learn that some vertices should follow the constraining objects. Therefore it was decided to not model the constraints and instead pass the positions and velocities of the pinned vertices in the input tensor.

In practice at preprocess stage all constrained vertices at time t are overridden with the values of the ones of the ground truth at $t + 1$. In the same way, at testing time, the predictions for the pinned vertices are overwritten to follow the constraining objects. The ultimate decision was to compute the objective function mask at training time only for the unconstrained vertices. This allowed not only implementing constraints, but also to simplify computations.

7.5.2 Future frames data augmentation

In the future frames approach a form of data augmentation is performed, meaning that the dataset was extended procedurally at training time. For each sample frame, during training the network is stepped forward in the future 5 times and the predicted result is added to the training samples using as ground truth the existing value of the sequence. If n is the length of the sequence (350 in this work), then new samples are added up to the frame n-5 of the sequence because the future frames after that do not exist. In this approach the cost function stays the same as for the single frame, just the dataset is extended on-the-fly at training time.

7.5.3 Future frames partial derivatives accumulation

In Tompson et al. (2016) the accumulation of future frames partial derivatives is used to minimize the long term divergence of the velocity field. A similar technique is used in the approach described in this section. In the same way as described in the previous subsection, at each call of the training function for a sample, the network is stepped forward 5 times, but the difference with the previous approach is that the history in the forms of a computational graph of this future frame is kept. This means that it is possible to do backpropagation through time by first computing the partial derivatives (gradients) of the future frame loss function and then accumulating (summing) them to the ones of the current frame sample (see Tompson et al. (2016)). In practice this is equivalent to minimizing in parallel the error that the network would make in the future if outputting the current single frame prediction. The gradients are necessary for the optimization algorithm to minimize the objective via Stochastic Gradient Descent. In this work the adopted descent algorithm is Adam (Kingma & Ba 2014).

7.5.4 RNN

A Recurrent Neural Network is able to keep a memory of what it has "seen" in a sequence for a specified temporal window size. This allows it to learn better patterns and features that evolve in time, making it particularly suitable for instance in Natural Language Processing and words prediction in a sentence. For this reason, considering that a physics simulation is exactly a temporally coherent sequence of frames governed by a law, it seems very appropriate to try this approach. While in the architectures presented before the input was a single pair of frames $(t, t+1)$, here the input is constituted by sequences of pairs of contiguous frames. For example if the window size is 10 frames, the input is two sequences 10 samples long. An RNN can be thought of as a loop (recurrence) in which at each step a new input of the sequence gets in and the output feeds back into the network itself as a new hidden state (the equivalent of a deep layer), in this way carrying along a memory. In this case the layers are convolutional (GCNN) and the objective function is equivalent to the previous ones.

To combat the long-term error accumulation all these strategies have to use as inputs new samples generated on-the-fly at the previous time step which means that new disks have to be recomputed. The reason is that the new predicted frame geometry could be very different from the existing ground truth of the dataset at that time. Therefore there is an inherent error made when, instead of recomputing the disks, the existing ones of the scene are used. But recomputing these disks n times (in this case 5 steps in the future) for all the samples is computationally very expensive, mainly because of the costly geodesic distances recalculation. An alternative would be to use Euclidean distances, but for heavily deformed meshes this would introduce approximations that are too big and consequently errors. For the exact method used to compute the geodesic disks refer to Masci et al. (2015a).

7.5.5 Unsupervised Loss Function

By observing that a neural network is essentially a structured complex optimizer and that the integration of the equations of motion can be seen as an energy minimization, it seems logic trying to let the network learn in a completely unsupervised manner. The objective function is defined as:

$$f_{obj_{unsup}} = \lambda_d \mathbf{E_{deform}} + \lambda_r reg \tag{7.1}$$

with

$$\mathbf{E_{deform}} = \frac{\mathbf{1}}{\mathbf{2h^2}} \|\mathbf{M^{\frac{1}{2}}(p_{n+1} - p_n - hv_n - h^2M^{-1}f_{ext})}\|_{\mathbf{F}}^{\mathbf{2}} + \sum_{\mathbf{i}} \mathbf{W_i(p_{n+1})}$$

which indicates the compromise that the optimization algorithm should make between two terms. The first term expresses the momentum potential, that is the state the object will reach in a timestep if no internal or external forces were acting on it. The second one is the elastic potential energy (derivation of this formula is given in Bouaziz et al. (2014). This formula, as mentioned in Chapter 2, follows by mathematically proving a problem equivalence which results in what is called Variational Implicit Euler in the literature. The goal is to find through a powerful regressor (such as a deep neural network) the best configuration of vertex positions such that the cost is minimized.

7.5.6 SpatioTemporal Convolution

In case the deformation happens in parametric space and the data is packed into images as discussed in 7.4.1, the time component in the learning process can be introduced by tweaking the input such that multiple frames are sent in order at the same time. This consists in stacking position and velocity frames along the time component so that the convolution becomes spatio-temporal and is performed in three dimensions with a 3D filter instead of just two. Assael et al. (2016) use this data packing for video frames. The input data therefore becomes a tensor of dimensions [width, height, 3 * stack size]. The size of the stack, or temporal window, is a parameter that can be chosen prior to training.

7.6 Training and Testing Process

The training process consists of the adjustment of the network weights (filters) via backpropagation, using the gradients of the cost function for each sample. The network is trained for a specified number of epochs; an epoch consists in a loop in which all the samples are shown once to the network. As is standard practice when dealing with neural network training, the learning rate that is initialized at 0.001 is multiplied by a factor of 0.8 every 10 epochs of no progress (i.e. no decrease of the cost function), otherwise when there is progress the weights are saved out to be used at testing time as the best result. Another regularization technique adopted here is called dropout, which consists in setting to zero the activation functions of some stochastically determined units (neurons) of the network, a randomization that in practice is extremely effective.

To improve generalization, the samples are never sent in the same order during training, but randomly shuffled at each epoch. Moreover training is in general improved by using minibatches, consisting of groups of samples minimized in the same backpropagation step: in this work the batches are intended as groups of disk images on which to perform a standard convolution and therefore are $number of vertices$ in size.
Gradient clipping was also used to prevent the phenomenon of gradients explosion which could arise given the complex dataset.

As far as the testing phase is concerned, the important thing to notice about dropout is that it must be disabled for the output to be deterministic. As mentioned earlier, at testing time disks are recomputed: even if this contradicts with the purpose of creating a fast alternative to a solver, it was the only way to test the validity of the technique.

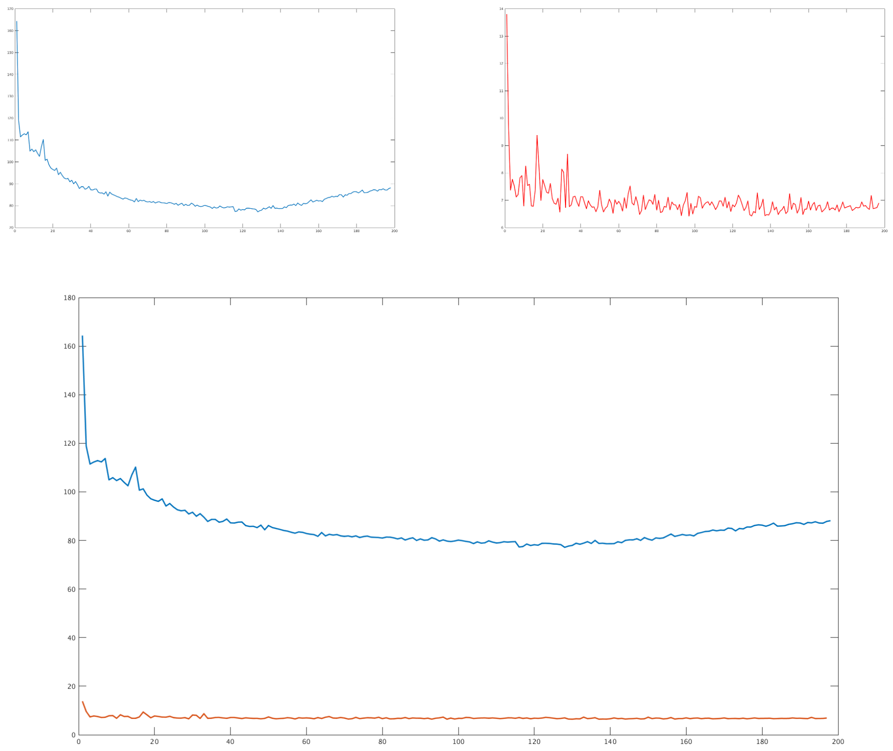

Figure 7.7: *Training (blue) and testing (red) curves for low res loss with future samples.*

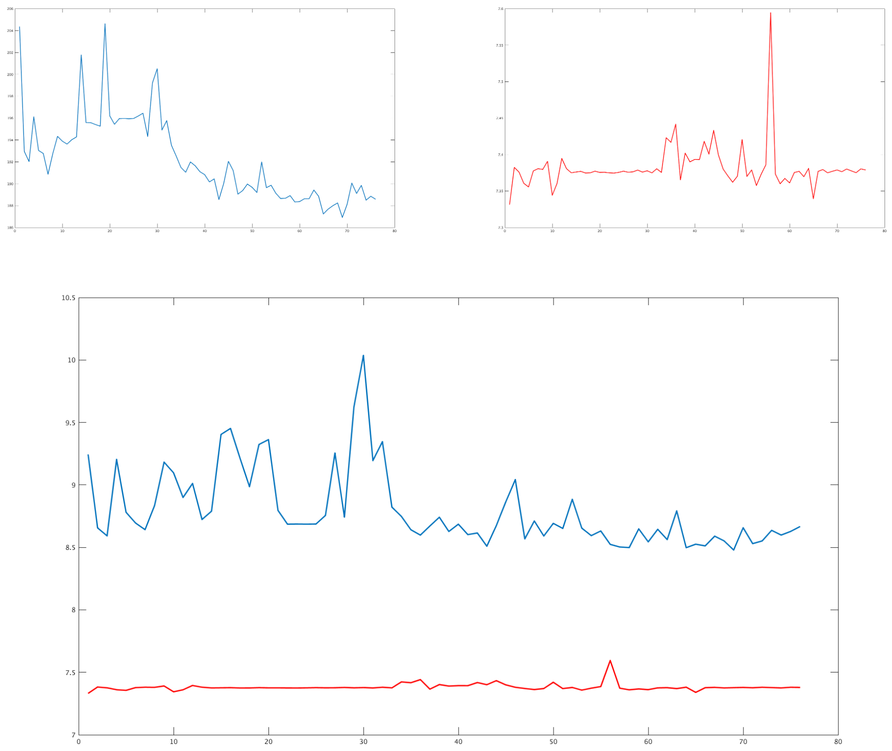

Figure 7.8: *Training (blue) and testing (red) curves for low res loss with future partial derivatives.*

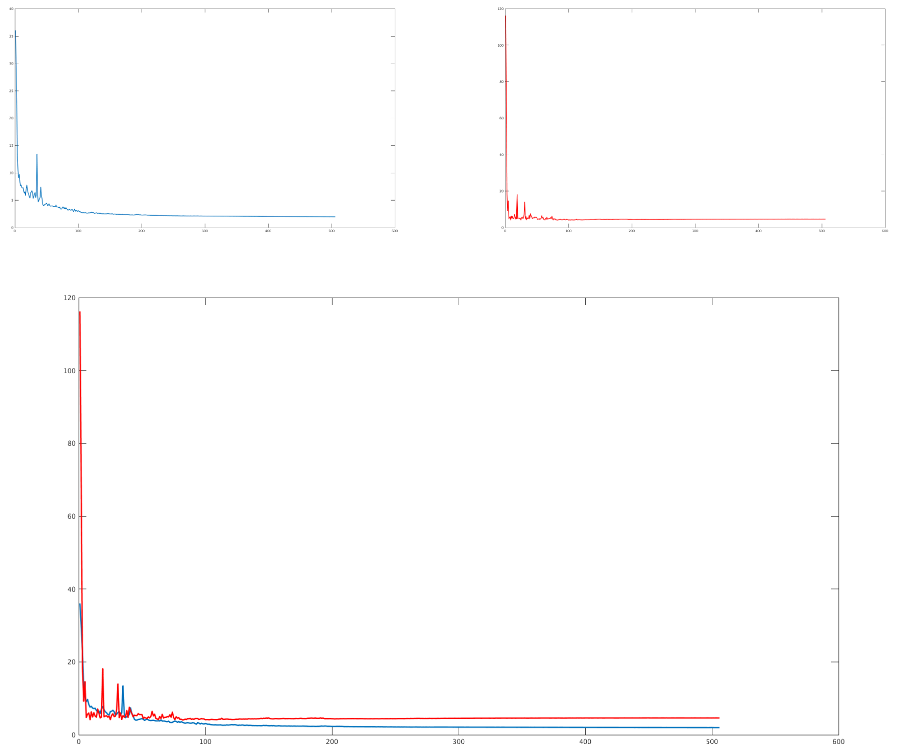

Figure 7.9: *Training (blue) and testing (red) curves for low res loss with RNN.*

Figures 7.7 - 7.18 show the training and testing losses for each of the cost functions discussed above, for both low and high resolution datasets and for the version with images. It should be noted that the graph plots do not represent the accuracy loss of frames in the future, but the one of frames at time t and $t + 1$.

In particular for the low res version, Figure 7.7 shows that the data augmentation of the future samples does not improve the accuracy. In fact the training and loss curves don't even touch, something evident also for Figure 7.8. The graph for the RNN low res instead shows that until epoch 80 the training improves the accuracy and after that point a small amount of overfitting is present but does not increase over time. For the high resolution version, the same analysis can be given for the graphs in Figures 7.10 - 7.12.

As far as the graphs for the image version are concerned, the version without future samples in Figure 7.14, even though is quite noisy shows that accuracy increases but never enough and not in a stable way. The addition of future samples in Figure 7.15 makes the training very unstable and does not improve the accuracy. Figure 7.16 with future partial derivatives as well is just very chaotic and it is clear that the line of accuracy (in red) does not decrease much over time. Better training is obtained instead with the RNN in Figure 7.17 and with the spatio-temporal version in Figure 7.18 in which the accuracy improves over time. Figure 7.13 shows how the training for the unsupervised version gets stuck almost immediately in a local minimum.

7.7 Implementation and Results

The results in this section were produced using the weights obtained in the training process for the different loss function types on the datasets for low, high and images versions. Results represent the predictions of a testing scene that the network never trained on, which was used to test generalization. Iteratively after each frame prediction, the constraints were overridden with the ground truth values and resulting samples saved

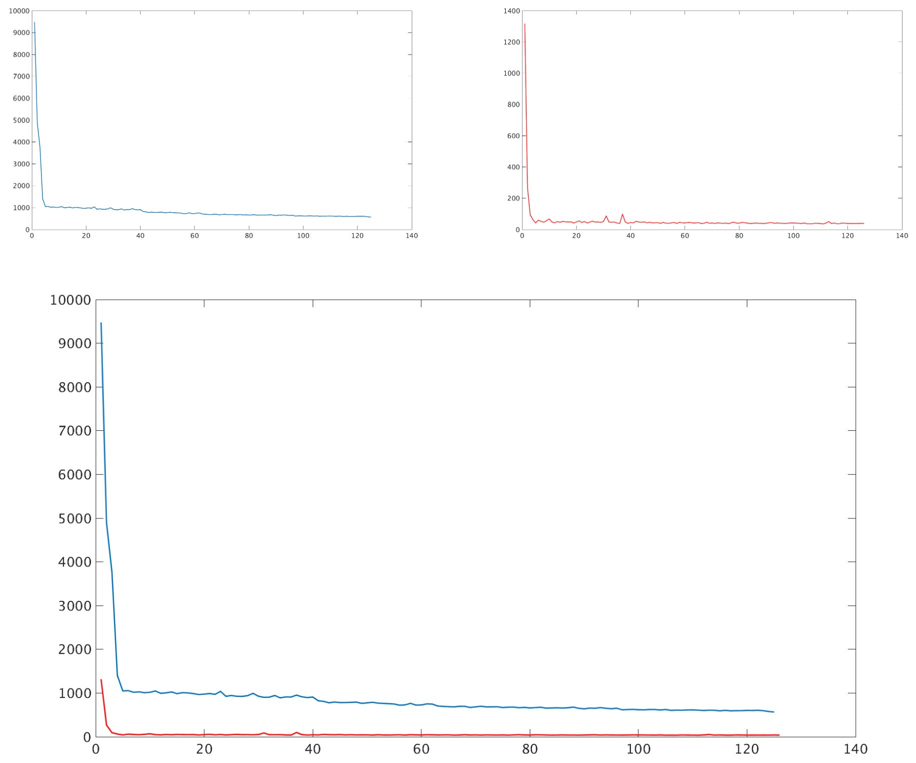

Figure 7.10: *Training (blue) and testing (red) curves for high res loss with future samples.*

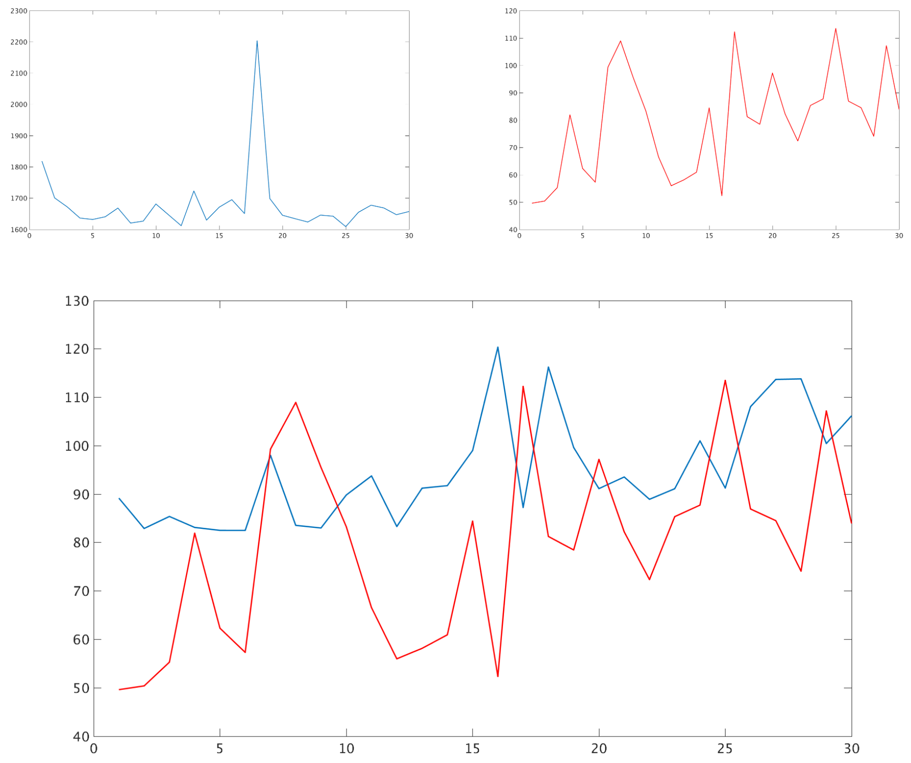

Figure 7.11: *Training (blue) and testing (red) curves for high res loss with future partial derivatives.*

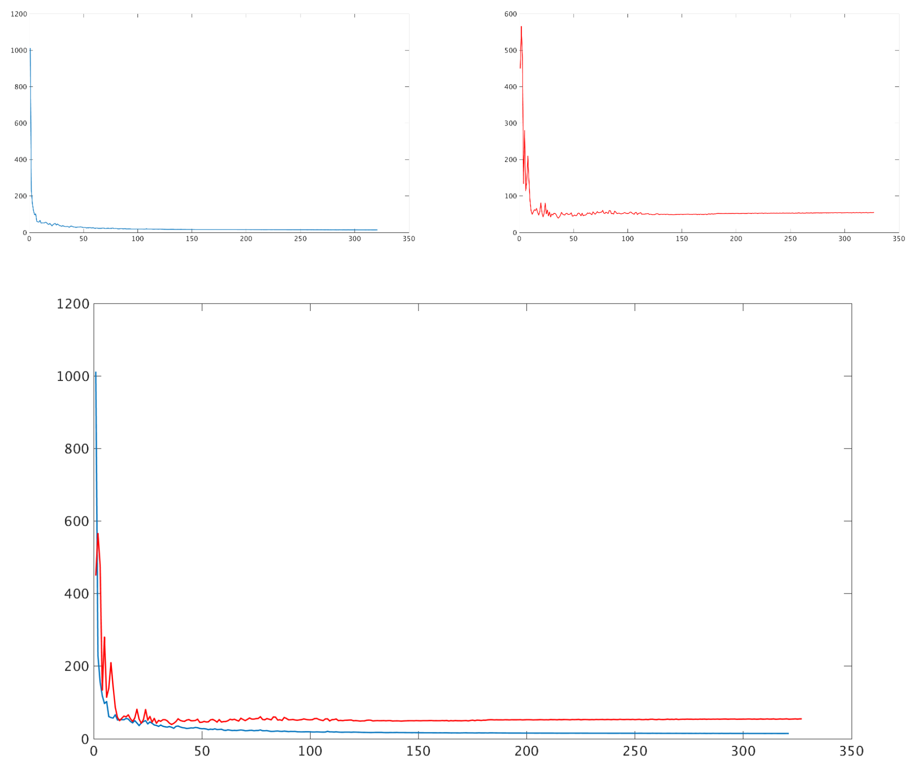

Figure 7.12: *Training (blue) and testing (red) curves for high res loss with RNN.*

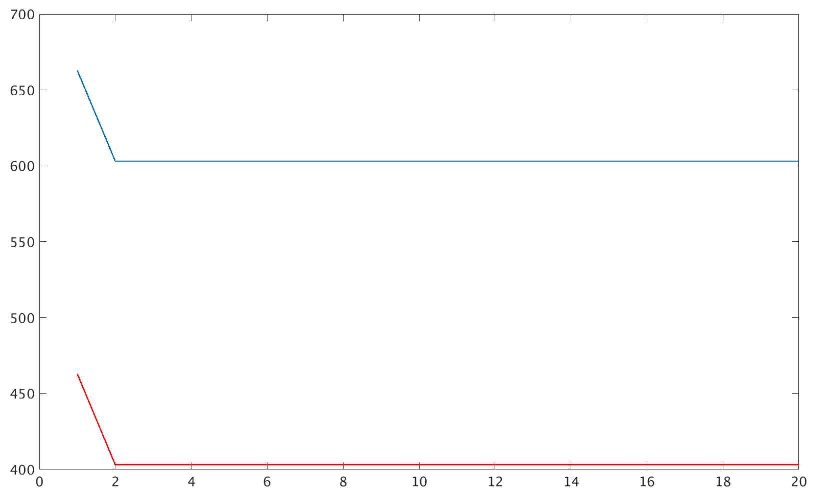

Figure 7.13: *Training (blue) and testing (red) curves for high res loss with unsupervised loss function.*

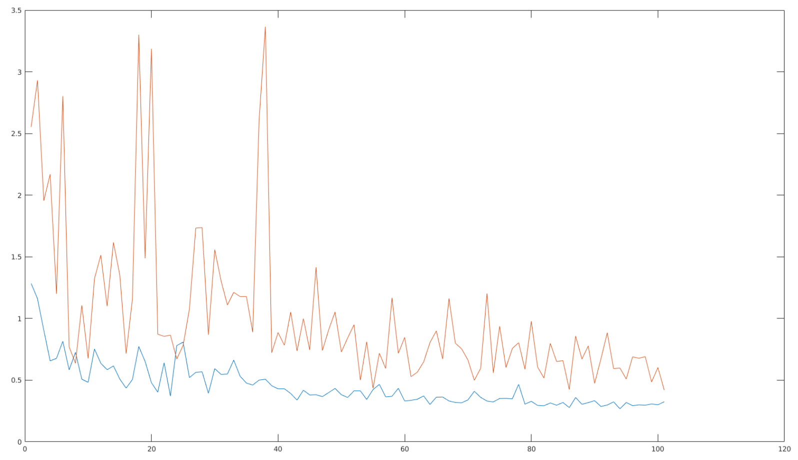

Figure 7.14: *Training (blue) and testing (red) curves for high res loss without future samples for images.*

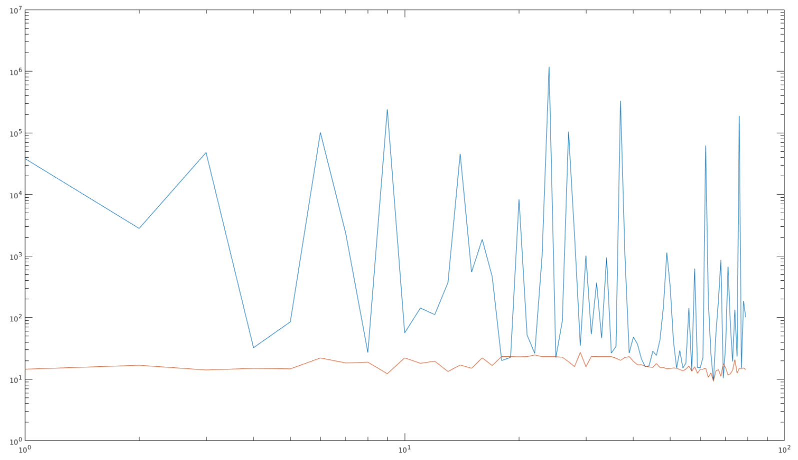

Figure 7.15: *Training (blue) and testing (red) curves for high res loss with future samples for images.*

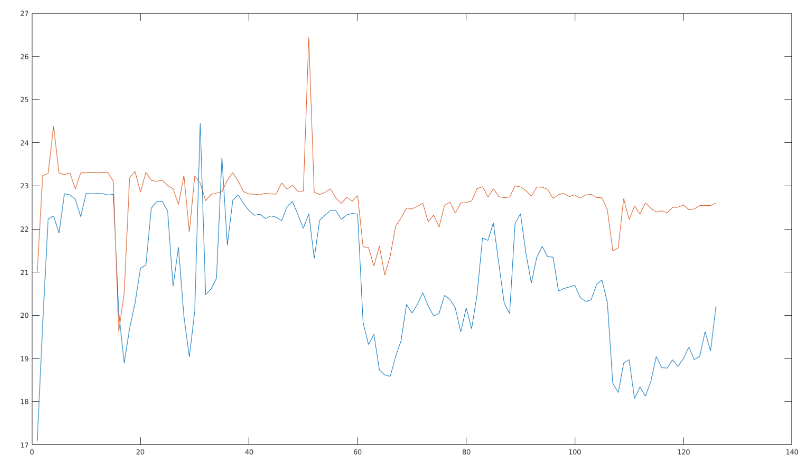

Figure 7.16: *Training (blue) and testing (red) curves for high res loss with future partial derivatives.*

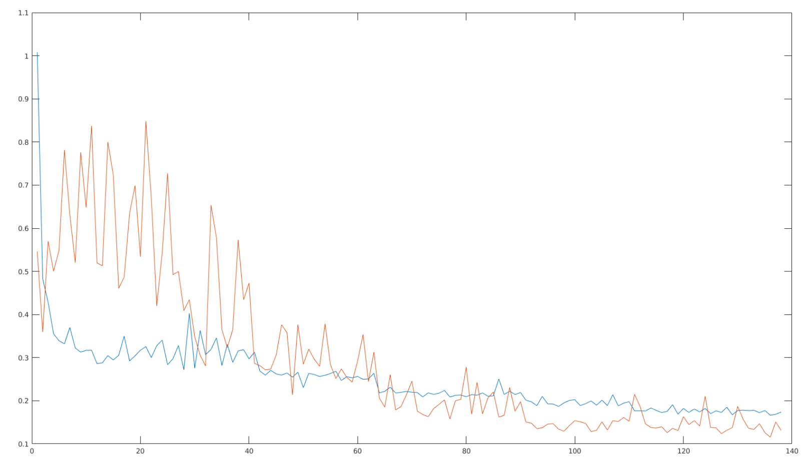

Figure 7.17: *Training (blue) and testing (red) curves for high res loss with RNN for images.*

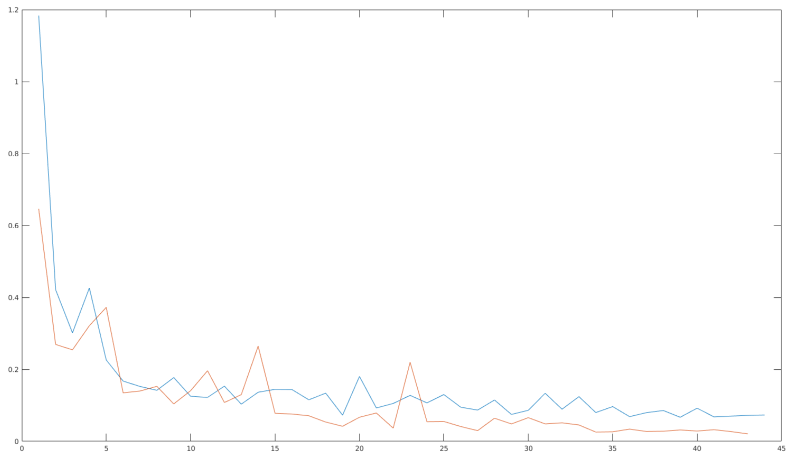

Figure 7.18: *Training (blue) and testing (red) curves for high res loss with spatio-temporal convolution for images.*

to disk to become new input for the subsequent loop.

Figures of the results (see Figures 7.19 - 7.30) seem to indicate that the future frames inclusion in the training is crucial for a good outcome for the predicted simulation. Moreover they suggest that without accurate disks the network is learning a wrong projection, demonstrated by the fact that for all the cases, after about 15 frames the error just keeps accumulating until distorting heavily the mesh. This seems unfortunately the price to pay for the use of the precomputed disks during training, disks that are associated to a mesh that differs from the predicted one. Another reason why the network is not learning a good projection could be that the adopted dataset is still too small and not diverse enough.

In terms of dynamics prediction quality, the RNN gives the most promising results (Figures 7.19 and 7.22) confirming the supposition that a temporal sequence in the input helps the network infer time-varying properties and patterns better. However, because the RNN does not adopt any long-term error reduction strategy, it still produces very distorted meshes.

The unsupervised loss function does not produce the expected results. A test was performed in which the minimization of one frame done by the network is compared with the result obtained by substituting in

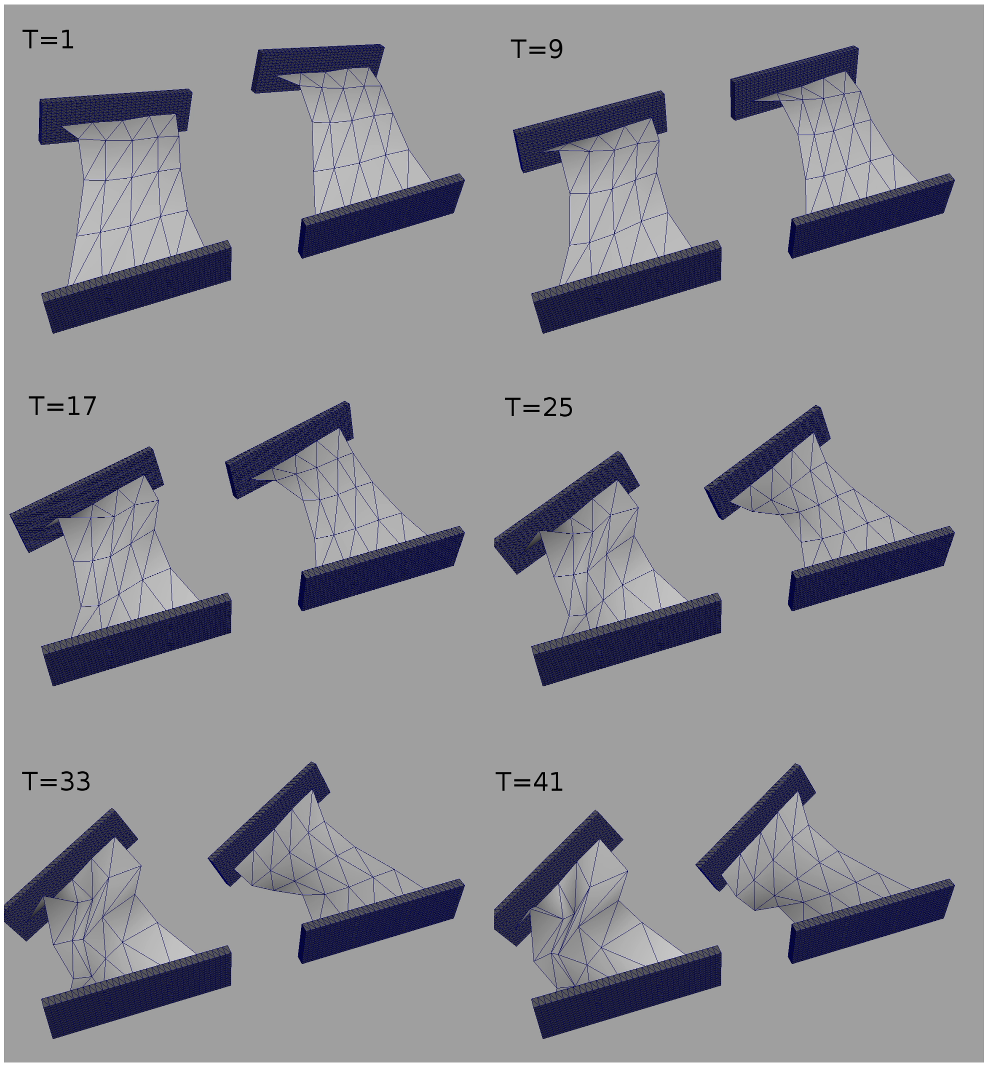

Figure 7.19: *Low res pairs of results (predicted, ground truth) for sampled frames in range 100-160 of the testing scene for RNN.*

Equation 7.1 the ground truth frame $t+1$: the network converges to the same result, but when trying to minimize all the frames of the scenes it simply gets stuck (Figures 7.13 and 7.25). One of the possible reasons is that the minimization should lead to different positive scalar values of the loss function for each frame because the elastic energy depends on the shape and the momentum potential from the inertia at that time frame and is almost never equal to zero.

As far as the version with images is concerned, a qualitative and visual analysis of the results shows that all tests except the RNN do not produce satisfying behaviour: the dynamics are plausible only for the

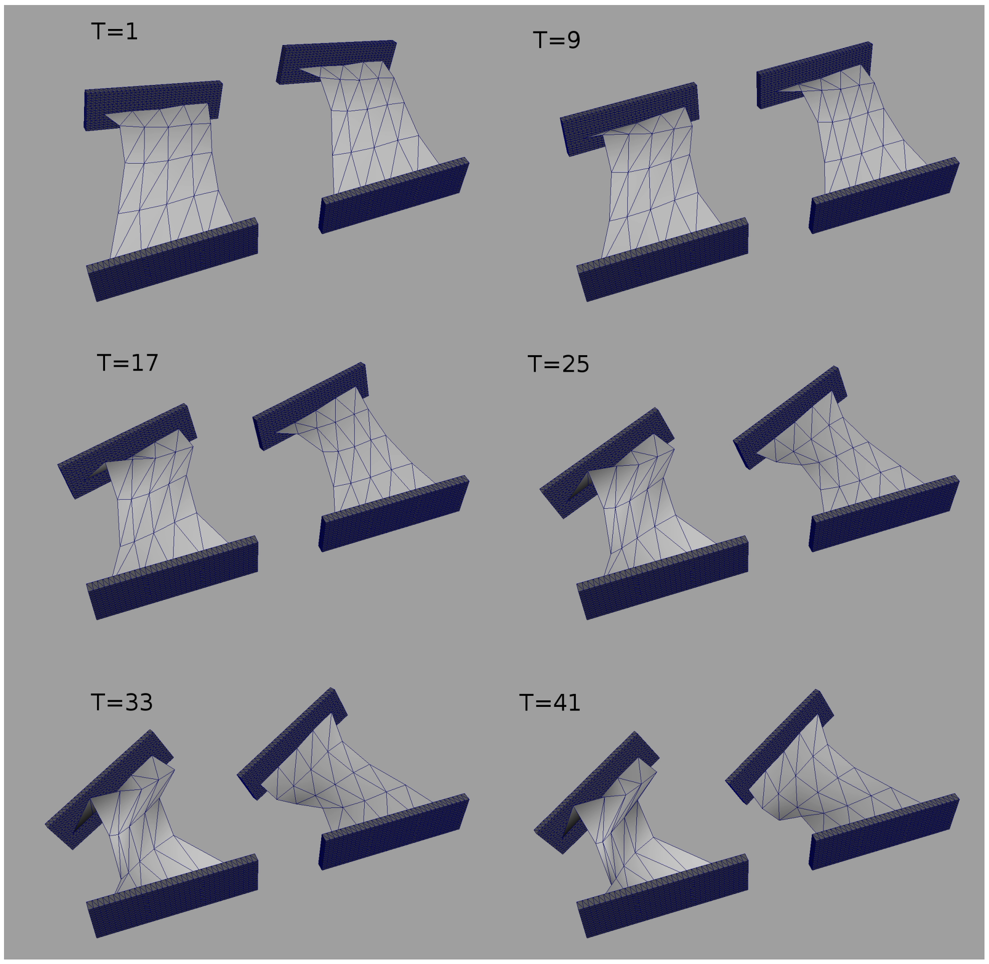

Figure 7.20: *Low res pairs of results (predicted, ground truth) for sampled frames in range 100-160 of the testing scene for partial derivatives.*

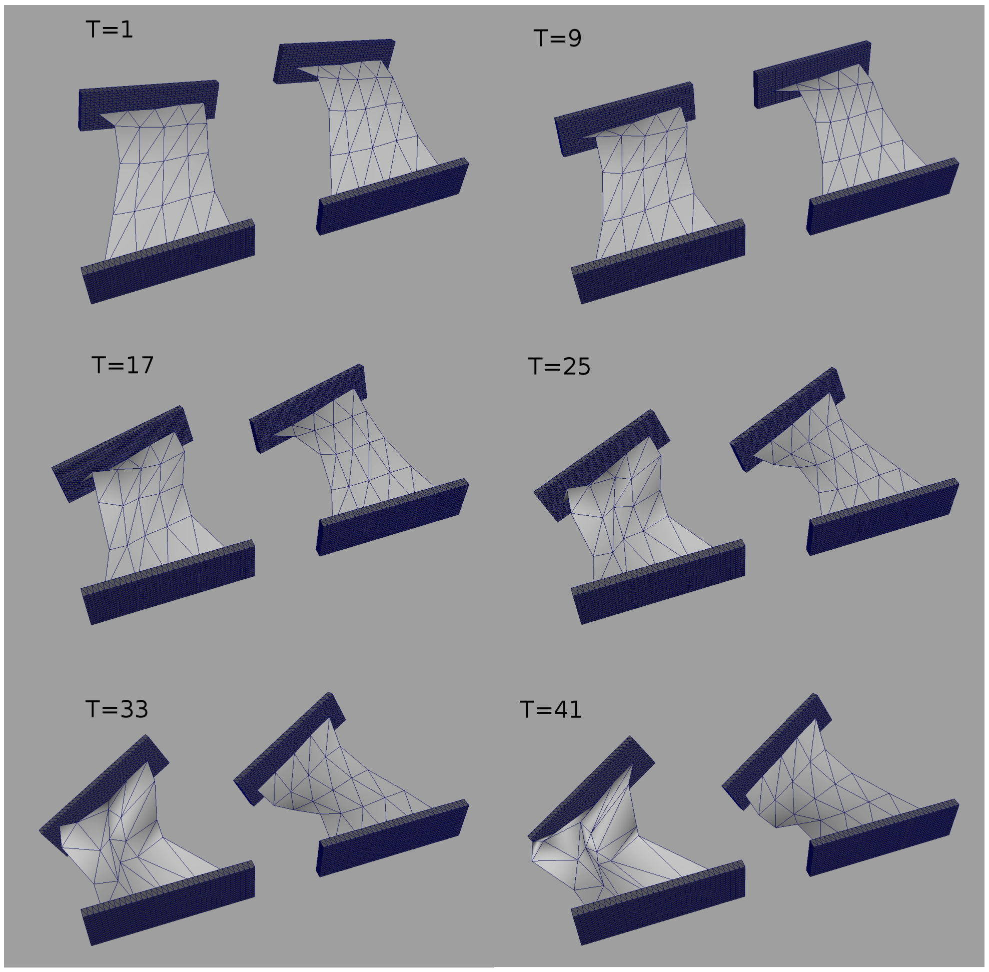

Figure 7.21: *Low res pairs of results (predicted, ground truth) for sampled frames in range 100-160 of the testing scene for future samples.*

recurrent version (Figure 7.29) in which the mesh follows the inertia of the constraints, even if the quality of the mesh deteriorates quickly and creates undesired crumpling effects. One of the possible reasons why at testing time the results are not satisfactory is that it could be possible in theory that the network is mixing up the various dynamics of disconnected scenes so in its hidden space the results are correct but they look visually wrong.

It should be noted that as mentioned in Battaglia et al. (2016), the goal of this work is not to obtain an exact frame-by-frame correspondence with the ground truth, especially because at each frame slight perturbations and variations of the initial conditions at the beginning of the timestep will propagate and lead to very different results (something that happens with a normal solver as well). Therefore plausibility of the behaviour and response to the constraints positions were the metrics used to visually measure the quality of the results. In some of the tests that took the longest times per epoch (up to 2 hours), the training was stopped manually at relatively early epochs (30-50) because there was no sign of improvement (something indicated by the continuous oscillation of the cost function).

The implementation is based on opensource code made available online by the authors of Masci et al. (2015b). Their implementation of GCNN makes use of the Lasagne framework which in turn wraps calls to the Theano deep learning API, written in Python. Their code was customized and extended for example by coding the loss functions and the RNN implementation to support multiple inputs (the position-velocity tensor and the associated disk).
The version using fields in UV space required custom implementation for the preprocessing and generation of the inputs. In order to represent the fields as 6-channels inputs, OpenGL was used to rasterize a mesh obtained from the UVs of the cloth. In the case of the squared shape it was a simple planar projection as shown in Figure 7.31. For each triangle, the velocity and position triplets at its nodes are passed to the renderer in order to be interpolated on the GPU and obtain a smooth image. The images are not rendered to screen but to two separate Frame

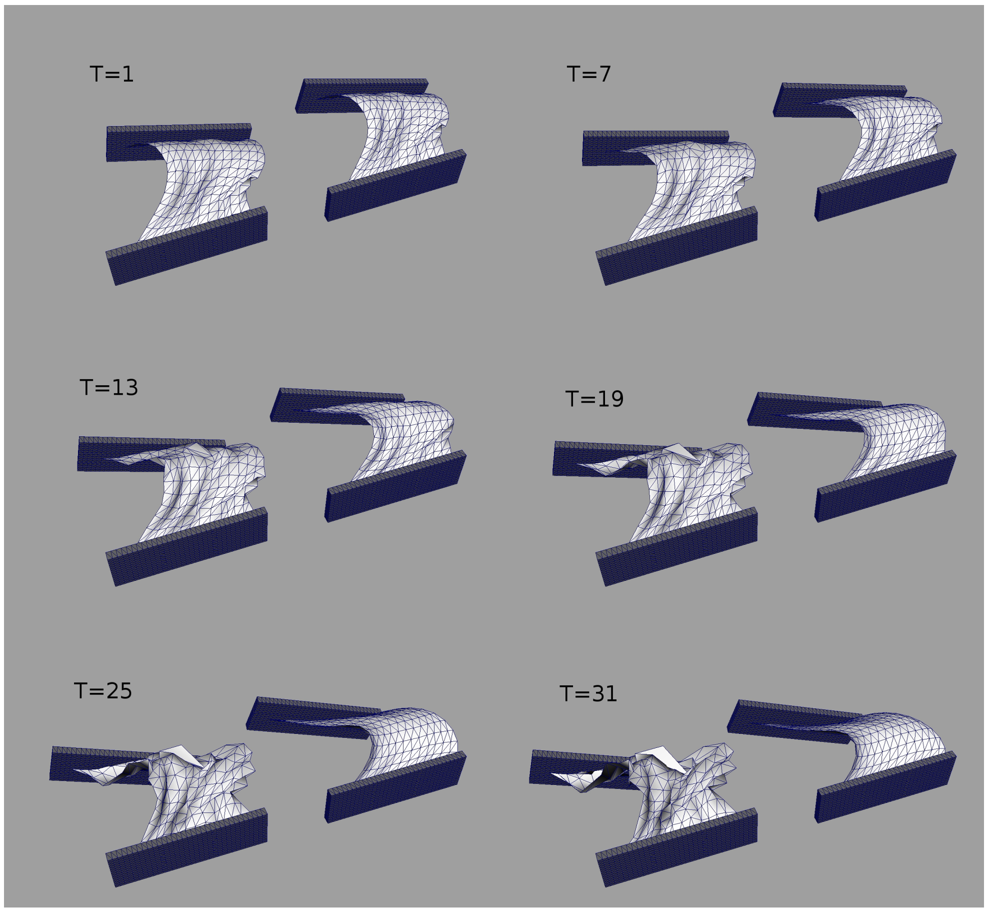

Figure 7.22: *High res pairs of results (predicted, ground truth) for sampled frames in range 100-160 of the testing scene for RNN.*

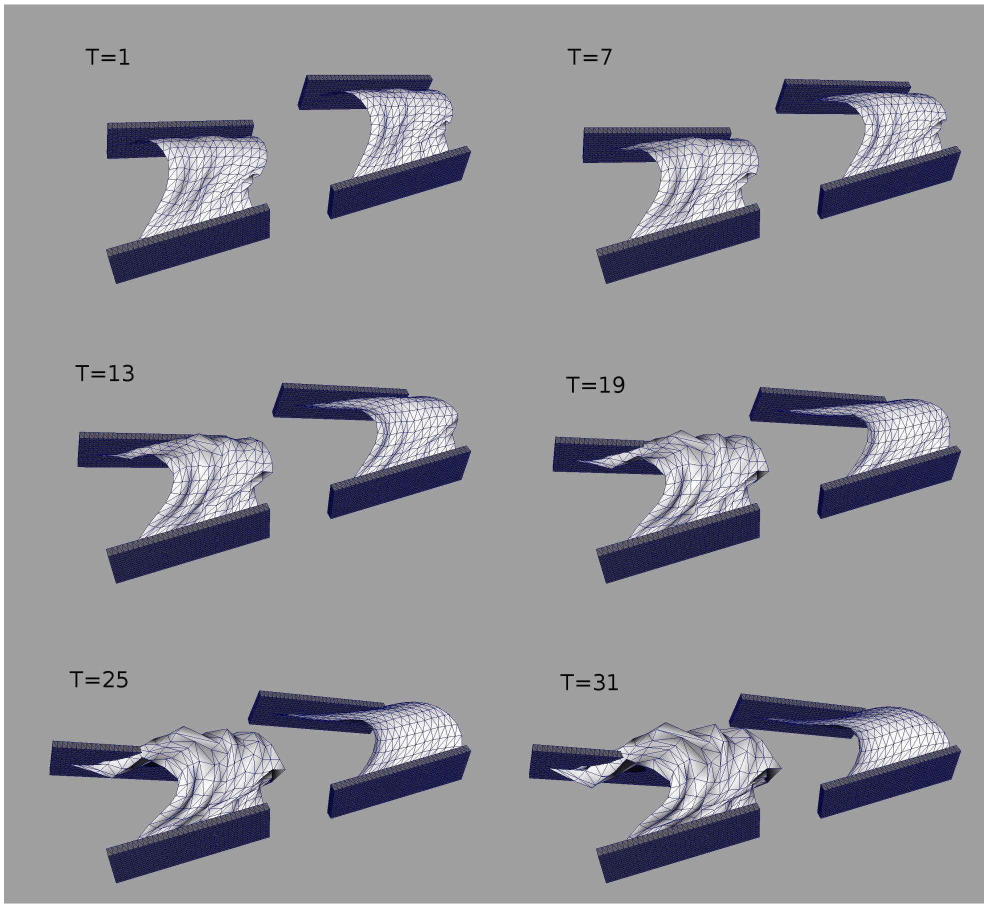

Figure 7.23: *High res pairs of results (predicted, ground truth) for sampled frames in range 100-160 of the testing scene for partial derivatives.*

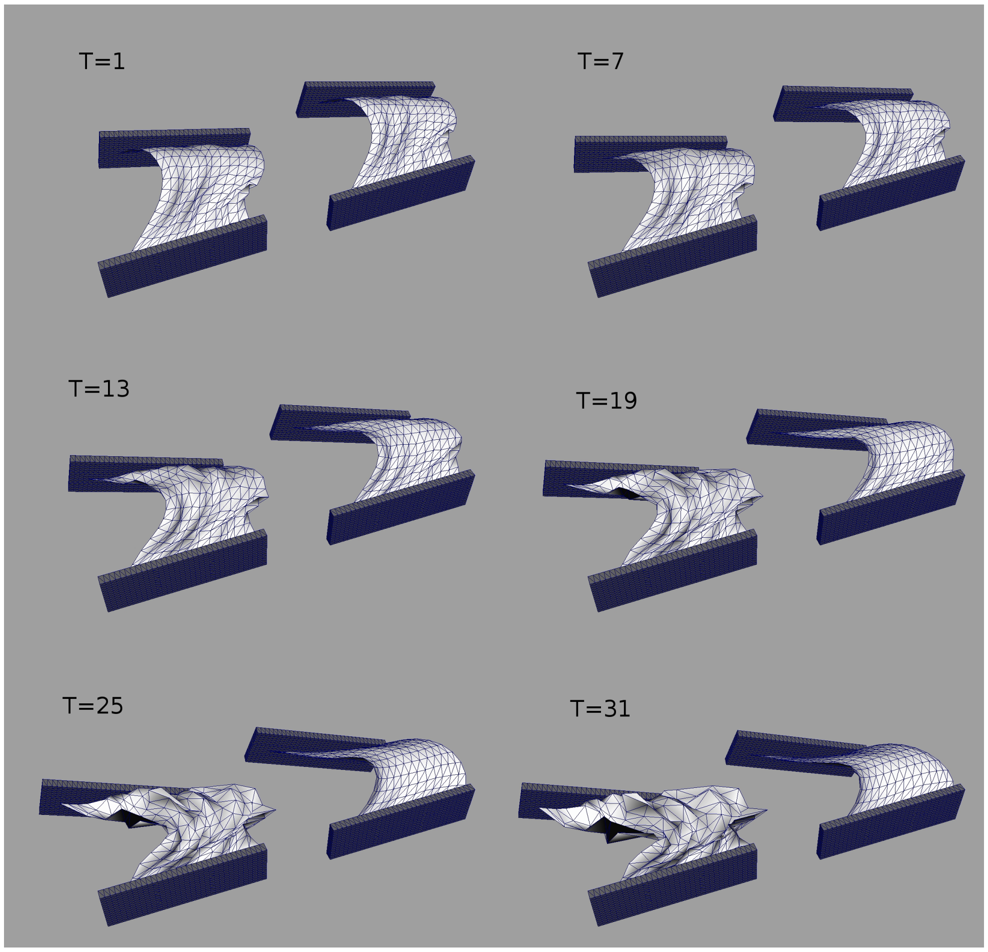

Figure 7.24: *High res pairs of results (predicted, ground truth) for sampled frames in range 100-160 of the testing scene for future samples.*

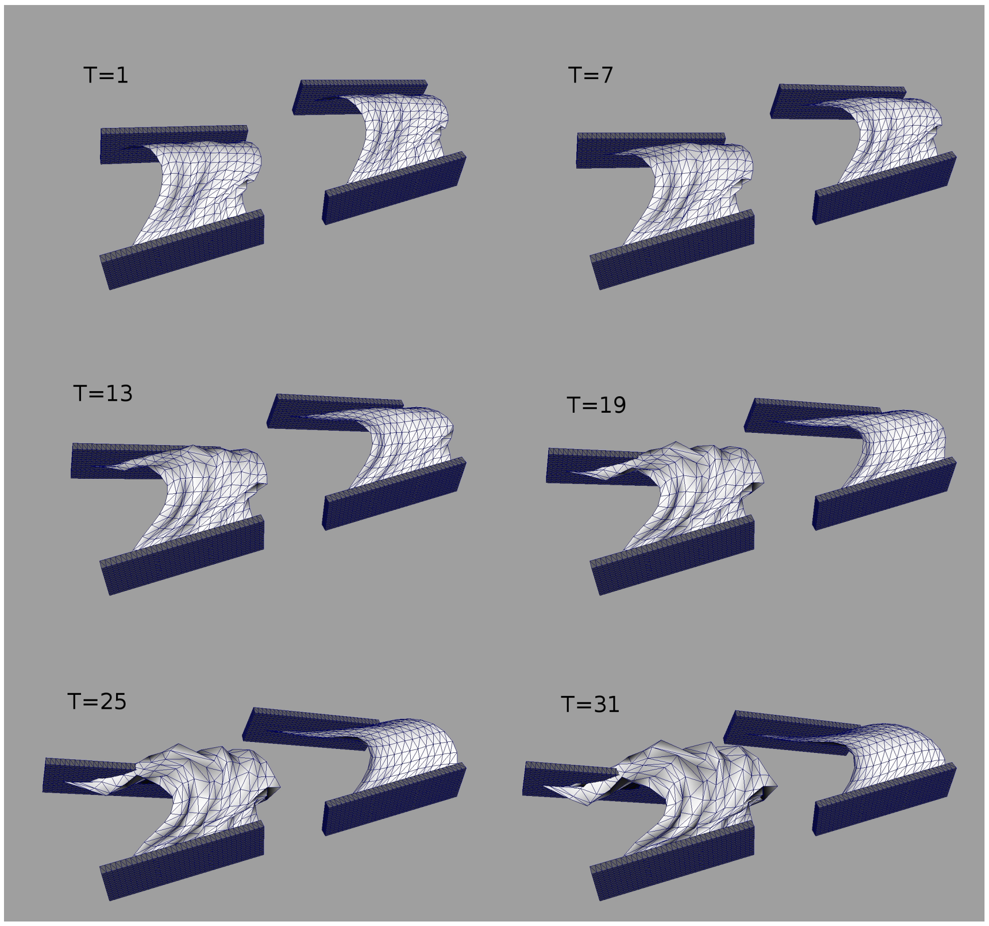

Figure 7.25: *High res pairs of results (predicted, ground truth) for sampled frames in range 100-160 of the testing scene for unsupervised loss.*

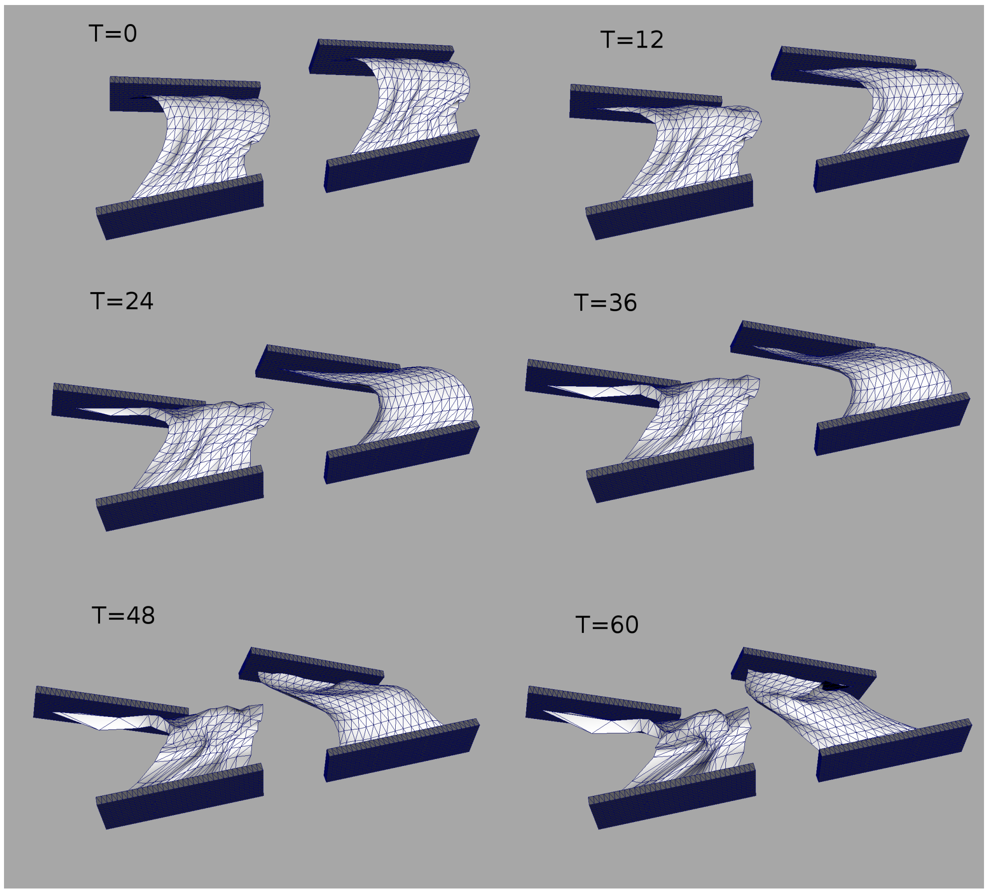

Figure 7.26: *High res pairs of results (predicted, ground truth) for sampled frames in range 100-160 of the testing scene without future samples (images).*

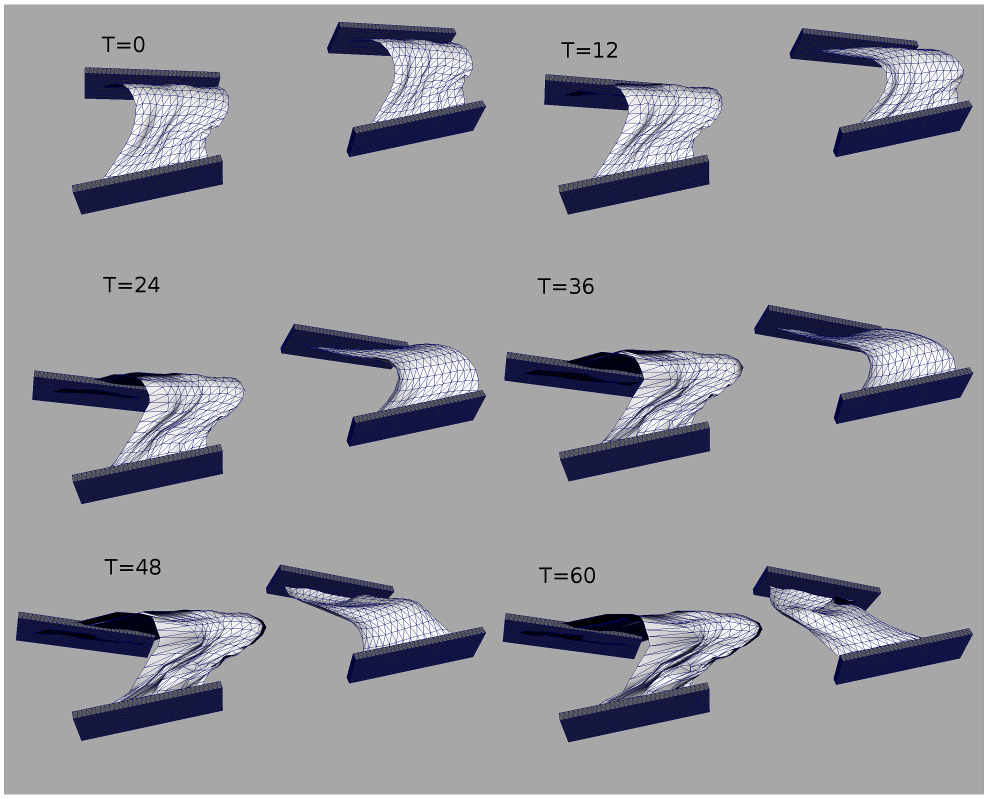

Figure 7.27: *High res pairs of results (predicted, ground truth) for sampled frames in range 100-160 of the testing scene for future samples (images).*

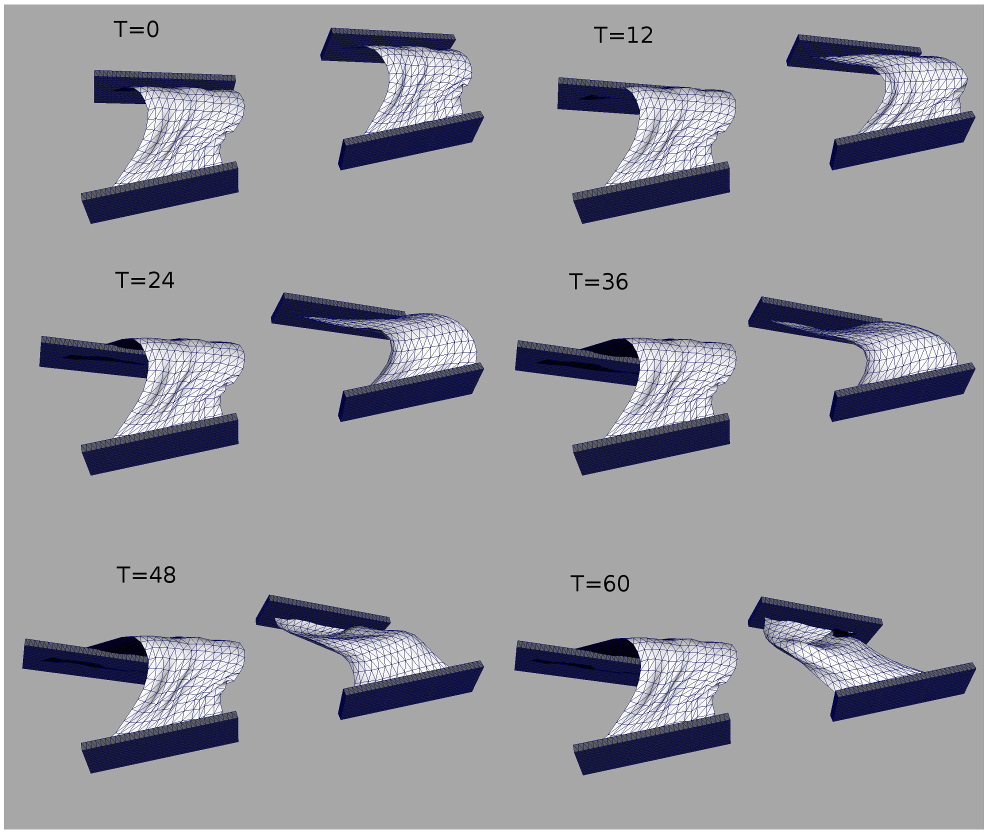

Figure 7.28: *High res pairs of results (predicted, ground truth) for sampled frames in range 100-160 of the testing scene for partial derivatives (images).*

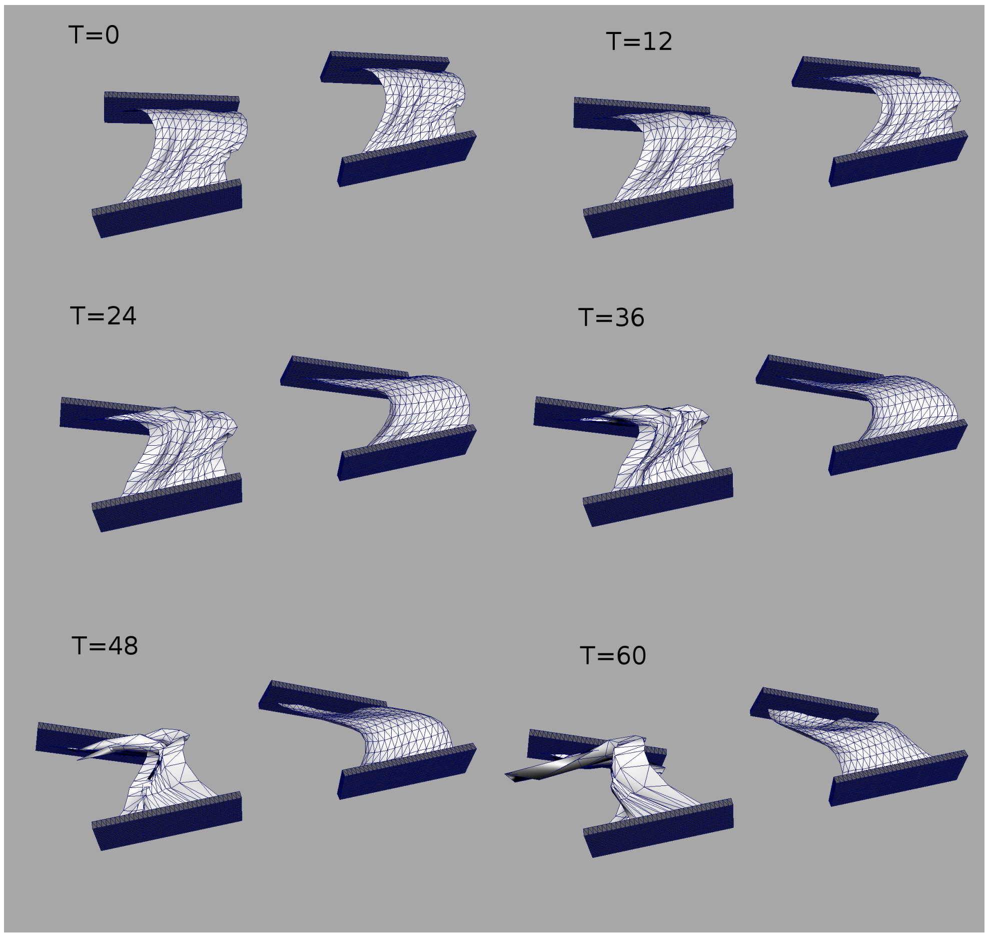

Figure 7.29: *High res pairs of results (predicted, ground truth) for sampled frames in range 100-160 of the testing scene for RNN (images).*

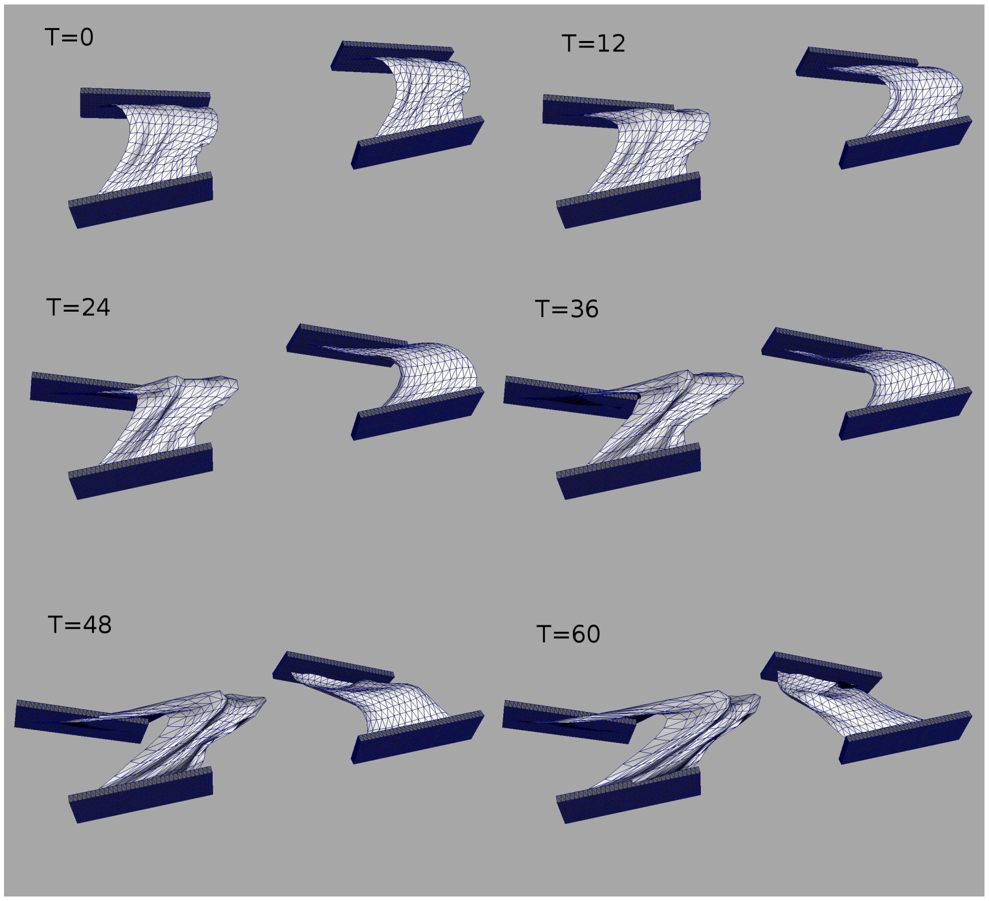

Figure 7.30: *High res pairs of results (predicted, ground truth) for sampled frames in range 100-160 of the testing scene for spatio-temporal (images).*

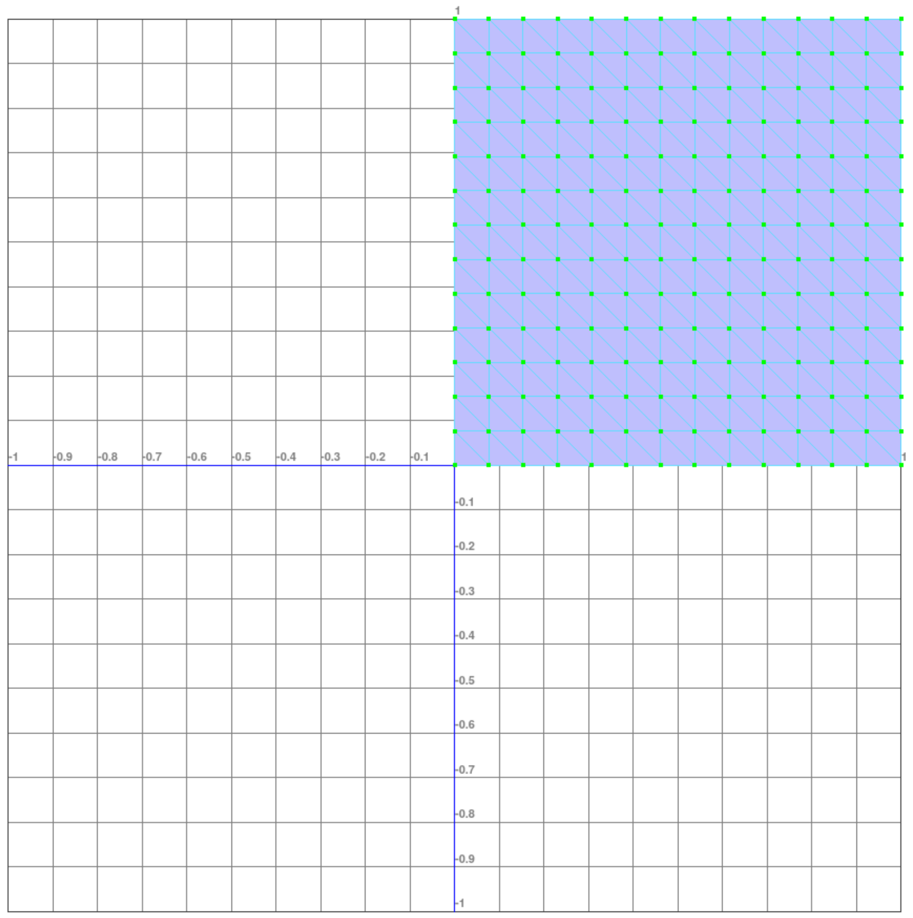

Figure 7.31: *UVs. Nodes corresponding to the rendered 2D mesh for field values interpolation in green.*

Buffer Objects as signed floats, after disabling clamping. During training and prediction, the renderer is called to override the triangles that contain constrained vertices because the predicted and constrained node values need to be re-interpolated. Another possible explanation of the problems appearing in the results is the relatively low resolution of the images. In the implementation it was 128x128 pixels.

Training was done on a NVIDIA Titan Xp and on a laptop NVIDIA GTX 780M.

The work presented in this chapter on machine learning concludes the part on the projects completed during the EngD in the hosting companies. The next and last part of this thesis draws the conclusions, discusses limitations and proposes future work for all the projects previously described.

Part III

Conclusions and Future Work

Chapter 8

Conclusions and Future Work

This thesis has discussed possible new directions and approaches that can be taken towards the production of realistic deformations for digital characters in a modern movie production pipeline. This chapter draws both specific (i.e. by project) and general conclusions based on the work completed, together with avenues for future work.

8.1 Conclusions

Active research on methods for the deformation of musculo-skeletal systems is a vital part of modern VFX. On the one hand the needed plausible and visually realistic results can be obtained with stable, accurate and computationally efficient deformation algorithms. On the other hand these technical improvements must be inserted in an artist-driven pipeline in which many software programs and technologies coexist. Artists often need to abstract from underlying technicalities and need interactive tools in order to express their creative intent in an environment characterized by continuous iterations. This work was therefore motivated by the need to improve both these two aspects related to the problem of obtaining visually convincing animated characters, bringing contributions to a specific part of the movie creation pipeline.

In this work several techniques covering different aspects of muscle deformation and, in general, physically-based animation have been presented:

- The creation of a custom simulation framework using FEM built on top of the VEGA library to help the company to test a new physically-based approach to character deformation. Formulas were derived to implement muscle activations for a constitutive material enriched with fibres. Constraints and collisions were also added to the framework contributing to the creation of a usable prototype.
- The creation of a novel method consisting of the interactive physics-based design of anatomical muscle geometries ready to be simulated. This method responds to the need for faster systems to model volumetric anatomically-plausible shapes.
- The development of a tool and a workflow, based on the simulation framework previously created, focused on the interactive placement of muscle geometries on a skeletal bones rig which takes into consideration collisions.
- A procedural method for skinning that uses implicitly-defined scalar fields to create wrinkle effects.
- The investigation of the application of Deep Learning to the simulation of deformable objects with the aim of improving the speed of a standard solver.

Except for the last pilot study on deep learning, the results obtained in each of the projects were mainly successful and even though they were not directly used in production, the tools and software developed are at the working prototype stage. Considering that most of them are already in the form of a Maya plugin, they can be deployed to the real pipeline without significant difficulties.

The subsections below present conclusions for each of the projects contained in this thesis, in order of appearance.

8.1.1 Muscle primitives modelling

The muscle primitives modelling described in Chapter 3 produced results that matched the initial goals of the project. Instead of sculpting each muscle separately using anatomy references, the goal was to find an alternative semi-automatic way to obtain plausible volumetric muscles by taking advantage of the benefits of a simulated approach. The proposed physics-based approach demonstrated to be a valid way to produce volumetric models and their associated fibre field from a limited input sketched directly on the surface of the character. The system was applied to the production-inspired use case of a muscular human arm and obtained realistic output contractions.

Despite the promising results, the system has some limitations and space for improvement. The areas at the borders of the patch are in fact still quite sharp and could be made smoother by adding custom energy terms, using greater resolution or turning the constrained vertices at the border into soft constraints. Some produced muscles, because of the flatness of the source patch, do not always fill all the available interior space and leave gaps between them and the bones. One could increase the pressure, use a softer material or run the inflation process for a longer time to improve on these issues. In the examples the presence of a fat layer between muscles and skin was discarded, considering the specific 3D model of a lean muscular body type examined. As an effect it was easier to sketch patches on the visible skin and the resulting muscle primitives are bigger than they should be. An offset based on a specified 3D texture could be applied per patch to take the fat into account (Saito et al. (2015)).

An alternative to the manual sketch of the patches, provided that the mesh contains texture mapping with UV coordinates, would be to use a texture template containing a representation of the muscle anatomy; the initial patches could be automatically generated based on segmentation of RGB colour values which could be used to transfer them between characters. This would also be an efficient way to bootstrap the patches because even though for lean and muscular characters the details on the skin are enough to distinguish most of the superficial muscles, the fat layer often present in characters smooths out these details and hides the underlying anatomy.

8.1.2 Muscle simulation framework

The muscle simulation framework described in chapter 4 produces very convincing results which demonstrate that a modern character production pipeline should include simulation to obtain visually plausible deformations with dynamics. The goal of proposing to the hosting company an evolution from the existing the semi-procedural system to one fully based on physics was at least in part achieved, through the development of a working prototype that showed detailed effects such as muscle and bones sliding, active muscle contractions and colliding biological tissues. The use case on which the framework was tested was the animation of a human arm. Their generality means that the same methods are applicable to CG animals or fantasy creatures having the same or a different combination of anatomical layers.

In addition to the complexity needed to have a good anatomical model, which can be mitigated but is still present, the limitations of the proposed framework are represented by the speed of simulation especially in the presence of many collision constraints and by the lack of an intuitive user interface. Moreover, in the presence of very highly constrained and compressed areas in contact (in a real character for example in the armpit region), the stability of the solver could suffer if a very small timestep is not used.

8.1.3 Placement of simulation-ready muscles

Chapter 5 presented a workflow aimed at helping the modelling of simulation-ready muscles in a production environment for the Visual Effects industry. It showed very promising results by proposing an integrated solution to a practical problem that rigging artists face while creating complex muscle systems. An artist in general spends a good amount of time placing complex organic shapes and then fixing their interpenetrations so this system would be beneficial.

One of the limitations is that the system was developed as a proof-of-concept prototype and is therefore yet to be fully tested before going into the production pipeline to test its effective advantage over an already well established workflow. The scalability to a full character was not tested; however because already placed muscles are static and their contact is computed fast, this is not likely to be a real problem. Finally it should be noted that to use the system effectively an artist would need to invest time on initial basic training because a physics-based approach is a new modelling paradigm that needs to be learned and developed like any other skill.

8.1.4 Procedural wrinkles

The technique presented in Chapter 6 to obtain wrinkles creates plausible results even comparable with physically accurate stretch-based methods. The initial goal of extending an existing procedural method by exploiting its constitutive parts was achieved and its generalization properties tested. The results show its potential for applications within a production pipeline.

Despite its potential, the technique for procedural wrinkles has some limitations. For example, being the output of the deformation time-dependent, finding the right parameters could require various iterations, something that makes it close in spirit to a simulation. Nevertheless, the user can always tweak single frames without rerunning the whole animation; in this case wrinkles will form following only the field at the current frame. In addition, it should be noticed that the quality of the fields tends to depend on the input shape, something that might limit the technique to cylindrical limbs and prevent the application to, for instance, face wrinkles generation.

8.1.5 Deep learning for deformable objects

The last project presented in this thesis in Chapter 7 did not fully meet the initial goals and expectations, but nevertheless constituted a great learning opportunity. In fact the objective was to obtain in a relatively short time convincing predictions for a toy problem such as a cloth simulation and at a later stage extend the system to muscle dynamics regression. Inspired by recent research, a variety of neural network architectures and loss functions (supervised and unsupervised) were tested and compared, but produced dynamic predictions with a medium-low level of accuracy; this fact prevented its extension to muscles.

One of the main limitations of the work on Deep Learning for deformable objects is that the system did not learn properly how to compensate for future errors therefore the quality and length of the predictions is limited to 20-30 frames and correct dynamics were not fully accomplished. Moreover, a simulation using a different mesh with different topology whould require in principle a new training of the network. However, as noted in Tompson et al. (2016), because the network is fully-convolutional the size of the input domain could be changed at inference time while training on a single resolution. This property was not verified in this work. Because of the bottleneck constituted by the disks, a comparison of execution times with a GPU physics solver was not done. This would have required a porting of the existing CPU based solver used to generate the dataset.

8.2 Future Work

The techniques proposed in this thesis constitute a small part of the ideal framework that is necessary in a real production, therefore they are not complete or in their final form. Below will be given directions for improvement and future work for each of the projects in order of appearance in this thesis.

For the muscle primitives modelling project, in addition to extending the system to the full body and trying out methods of transferring patches across characters, it would be an interesting future direction to test the application of a plasto-elastic material model and adaptive meshes.

Regarding the actual simulation system of chapter 4, even though the results are realistic and appreciated in the hosting company, a lot can be done to improve the realism, the usability of the framework and the efficiency. For example in the presented examples the coupled action between muscles and skin was mostly ignored: not only the skin should stretch and deform due to the underlying contracting muscles, but in turn it should produce a containing effect back onto the muscles in the form of an elastic forces response. To obtain this, the layers should be simulated all at once and not separately cached. To add even more realism, veins could be modelled from anatomy references as curves and their geometry could be merged with the skin or used as a displacement map. During simulation they could deform together with the skin layer and their thickness could be animated based on the muscle activation level and isometric contraction duration. In terms of artistic control, to direct the physics simulation a technique such as the one described in Martin et al. (2011) could be used, in which custom shapes are inserted in the dynamics of the solver and work as force attractors interpolated in strain space. This method seems to work very well, even though one of the drawbacks is that if the artist creating the shapes is not accurate enough, constraints such as volume preservation could be violated and the system could not be aware of it. Another possibility would be to inject custom shapes as new per-frame rest poses of the solver as in Kozlov et al. (2017). Also, tools to allow artists to groom complex networks of fibres to control the muscle shape would be greatly beneficial. One of the areas of research that would bring huge benefit to the industry is the development of a unified solver with coupling that stably and accurately supports deformable objects, hair, particles, cloth, and rigid bodies simulation. In fact a digital character almost always contains parts or accessories that can be modelled and simulated in one of those ways.

As far as the muscle placement system is concerned, there are many areas of improvement on which to focus. First of all, it would be desirable to adapt a constraint-based dynamics approach to avoid the problems of stability of penalty forces when high stiffness makes the system matrix poorly conditioned. To increase the user experience and make the simulation more closely resemble the desired results, it would be also beneficial to add an external skin mesh representing the superficial fascia as a boundary condition surface on which both the sculpting tool and the simulation can collide against. For the placement stage, it would be useful to add a plastic deformation functionality directly integrated in a fast solver as in Saito et al. (2015) , in which a decomposition of the deformation gradient is used to grow the muscles. A seamless integration of the modelling and placement plugins, now separated, would avoid a context-switch problem that can absorb time from the creative process. Moreover in terms of performance the code could be parallelized much more (for example for the internal force computation) and a simplified GPU version of the solver would boost the speed even more. Finally, because a FEM solver could be an too computationally expensive for this problem, other solvers based on PBD or XPBD may be a better option to consider.

For the Implicit Skinning project, as future work, the intention is to integrate adaptive tessellation technology. Even though in a production pipeline it is not common to have varying topology, the performance would benefit by having more detail only where needed, with the option to export displacement maps for rendering. It would also be useful to investigate ways to make the convolution surfaces look less cylindrical and more organic, not restricted only to circular profiles; for example noise could be added, or segments with different radius could be layered. Moreover, another interesting future direction inspired by Cao et al. (2015) would be to combine the proceduralism of the method with a trained approach in order to learn the space of input parameters for a closer match to the physical appearance of acquired data. Finally, a better falloff of the radius per curve would be desirable as wrinkles should fade away the further they are from the joint.

In terms of the machine learning project in chapter 7, given the understanding of some of the reasons why the system is underperforming, various avenues for future work can be taken. First of all there is clearly a need to research improvements on the speed of disk computation, with the aim of real-time performance. Progress in this direction is being made in the work by Monti et al. (2016). The computation of the disks using Euclidean distances was not tested to measure the actual performance and accuracy, therefore it would be useful for comparison. Alternatively, the on-the-fly recomputation of geodesic distances could be done only for some random samples of the training set. Minibatches of frames should also be used to improve the training, while at the moment the batches have dimension the number of vertices, containing one image per vertex. Max pooling is another technique used to improve generalization and performance during training that would be appropriate to implement. After each convolution the output dimension is halved multiple times so the most significant features remain. However this downsampling would be applied on the mesh topology by a decimation algorithm and it is yet to be demonstrated if it would benefit the learning process. In terms of improvements to the loss functions, extra terms considered for future work would be the volume (area) preservation for the predicted triangles using the determinant-based formulation found for example in Ichim et al. (2017) and a term to preserve an amount of smoothness of the mesh to avoid heavy distortions. Finally, research is needed to extend the convolution to support tetrahedral volumetric objects via spherical coordinates disks so that the learning method can be applied to geometries representing muscles and fat.

As a final closing note, it should be always kept in mind that technologies and consequently workflows evolve fast and this is true especially for Visual Effects, considering the recent and current industry trends. In fact if I could start my EngD again I would focus predominantly on real-time and interactive methods rather than using FEM just because it is accurate. The Visual Effects industry is going through a major revolution in which game engines are more and more a fundamental part of movie production stages such as pre-visualization, camera motion, interactive design of environments, look development and lighting. The coming wave of Virtual and Augmented Reality (VR/AR) also requires that realistic character deformation must happen in real time. The idea of contributing to the creation of illusive but magical, emotional and immersive experiences constitutes the beauty of doing research in this exciting field.

References

D. Ali-Hamadi, et al. (2013). 'Anatomy Transfer'. *ACM Trans. Graph.* **32**(6):188:1–188:8.

Andrej Karpathy (2017). 'CS231n Convolutional Neural Networks for Visual Recognition'. `http://cs231n.github.io/`.

D. Anguelov, et al. (2005). 'SCAPE: Shape Completion and Animation of People'. *ACM Trans. Graph.* **24**(3):408–416.

Y. M. Assael, et al. (2016). 'LipNet: Sentence-level Lipreading'. *CoRR* **abs/1611.01599**.

D. Baraff & A. Witkin (1998). 'Large steps in cloth simulation'. In *Proceedings of the 25th annual conference on Computer graphics and interactive techniques*, pp. 43–54. ACM.

J. Barbič & D. L. James (2005). 'Real-Time Subspace Integration for St. Venant-Kirchhoff Deformable Models'. In *ACM SIGGRAPH 2005 Papers*, SIGGRAPH '05, pp. 982–990, New York, NY, USA. ACM.

J. Barbič, et al. (2012). 'Interactive Editing of Deformable Simulations'. *ACM Trans. on Graphics (SIGGRAPH 2012)* **31**(4).

P. W. Battaglia, et al. (2016). 'Interaction Networks for Learning about Objects, Relations and Physics'. *CoRR* **abs/1612.00222**.

B. Bickel, et al. (2009). 'Capture and Modeling of Non-linear Heterogeneous Soft Tissue'. In *ACM SIGGRAPH 2009 Papers*, SIGGRAPH '09, pp. 89:1–89:9, New York, NY, USA. ACM.

S. Blemker & S. Delp (2005). 'Three-Dimensional Representation of

Complex Muscle Architectures and Geometries'. *Annals of Biomedical Engineering* **33**(5):661–673.

S. S. Blemker, et al. (2005). 'A 3D model of muscle reveals the causes of nonuniform strains in the biceps brachii'. *Journal of Biomechanics* **38**(4):657–665.

J. Bonet & R. D. Wood (1997). *Nonlinear continuum mechanics for finite element analysis*. Cambridge university press.

S. Bouaziz, et al. (2014). 'Projective Dynamics: Fusing Constraint Projections for Fast Simulation'. *ACM Trans. Graph.* **33**(4):154:1–154:11.

R. Bridson, et al. (2003). 'Simulation of clothing with folds and wrinkles'. In *Proceedings of the 2003 ACM SIGGRAPH/Eurographics symposium on Computer animation*, pp. 28–36. Eurographics Association.

M. M. Bronstein, et al. (2016). 'Geometric deep learning: going beyond Euclidean data'. *CoRR* **abs/1611.08097**.

C. Cao, et al. (2015). 'Real-time High-fidelity Facial Performance Capture'. *ACM Trans. Graph.* **34**(4):46:1–46:9.

CGCircuit (2016). 'CGCircuit Tutorial, Skinning with nCloth'. https://www.cgcircuit.com/tutorial/skinning-with-ncloth/.

Chaos Group (2015). 'Introduction to deformable objects models and muscle simulation - Fabio Turchet, MPC London, CG2 Talk Code'. `https://www.youtube.com/watch?v=i2s120TV-F0`.

H. Choi & S. Blemker (2013). 'Skeletal Muscle Fascicle Arrangements Can Be Reconstructed Using a Laplacian Vector Field Simulation'. *PLoS ONE* **8(10)**(e77576).

K.-J. Choi & H.-S. Ko (2002). 'Stable but Responsive Cloth'. *ACM Trans. Graph.* **21**(3):604–611.

S. Clutterbuck & J. Jacobs (2010). 'A physically based approach to virtual character deformation'. In *ACM SIGGRAPH 2010: Talks*.

O. Comas, et al. (2008). 'Efficient Nonlinear FEM for Soft Tissue Modelling and Its GPU Implementation within the Open Source Framework SOFA'. In F. Bello & P. Edwards (eds.), *Biomedical Simulation*, vol. 5104 of *Lecture Notes in Computer Science*, pp. 28–39. Springer Berlin Heidelberg.

S. Comer, et al. (2015). 'Under the Scalpel - ILM's Digital Flesh Workflows'. In *ACM SIGGRAPH 2015 Talks*, SIGGRAPH '15, pp. 10:1–10:1, New York, NY, USA. ACM.

M. Cong, et al. (2015). 'Fully Automatic Generation of Anatomical Face Simulation Models'. In *Proceedings of the 14th ACM SIGGRAPH / Eurographics Symposium on Computer Animation*, SCA '15, pp. 175–183, New York, NY, USA. ACM.

S. Delp, et al. (2007). 'OpenSim: Open-Source Software to Create and Analyze Dynamic Simulations of Movement'. *Biomedical Engineering, IEEE Transactions on* **54**(11):1940–1950.

Fabric Engine (2015). 'Fabric Engine'. `http://fabricengine.com/`.

Y. Fan, et al. (2014). 'Active Volumetric Musculoskeletal Systems'. *ACM Trans. Graph.* **33**(4):152:1–152:9.

C. Flynn & B. Mccormack (2009). 'Simulating the wrinkling and aging of skin with a multi-layer finite element model' **43**:442–8.

S. Fortier (2013). 'Fortier, S.'. http://www.simonefortier.com/fascia-stretching-therapy/.

J. Gain & D. Bechmann (2008). 'A Survey of Spatial Deformation from a User-centered Perspective'. *ACM Trans. Graph.* **27**(4):107:1–107:21.

T. Geijtenbeek, et al. (2013). 'Flexible Muscle-based Locomotion for Bipedal Creatures'. *ACM Trans. Graph.* **32**(6):206:1–206:11.

I. Goodfellow, et al. (2016). *Deep Learning.* MIT Press. `http://www.deeplearningbook.org`.

E. Guérin, et al. (2017). 'Interactive Example-based Terrain Authoring with Conditional Generative Adversarial Networks'. *ACM Trans. Graph.* **36**(6):228:1–228:13.

R. Haapaoja (2016). 'A collision framework for rigid and deformable body simulation (Dissertation)'. *Retrieved from http://urn.kb.se/resolve?urn=urn:nbn:se:liu:diva-133216* .

T. Hädrich, et al. (2017). 'Interactive Modeling and Authoring of Climbing Plants'. In *Computer Graphics Forum*. Wiley Online Library.

A.-E. Ichim, et al. (2017). 'Phace: Physics-based Face Modeling and Animation'. *ACM Trans. Graph.* **36**(4).

G. Irving, et al. (2007). 'Volume Conserving Finite Element Simulations of Deformable Models'. *ACM Trans. Graph.* **26**(3).

G. Irving, et al. (2004). 'Invertible Finite Elements for Robust Simulation of Large Deformation'. In *Proceedings of the 2004 ACM SIGGRAPH/Eurographics Symposium on Computer Animation*, SCA '04, pp. 131–140, Aire-la-Ville, Switzerland, Switzerland. Eurographics Association.

J. Jacobs, et al. (2016). 'How to Build a Human: Practical Physics-based Character Animation'. In *Proceedings of DigiPro*, pp. 7–9. ACM.

A. Jacobson, et al. (2011). 'Bounded Biharmonic Weights for Real-time Deformation'. *ACM Trans. Graph.* **30**(4):78:1–78:8.

J. Jimenez, et al. (2011). *GPU Pro 2*, chap. Practical and Realistic Facial Wrinkles Animation. AK Peters Ltd.

H. Joodaki & M. Panzer (2018). 'Skin mechanical properties and modeling: A review' **232**:095441191875980.

L. Kavan, et al. (2008). 'Geometric Skinning with Approximate Dual Quaternion Blending'. *ACM Trans. Graph.* **27**(4):105:1–105:23.

J. Kim & N. S. Pollard (2011). 'Fast Simulation of Skeleton-driven Deformable Body Characters'. *ACM Trans. Graph.* **30**(5):121:1–121:19.

S. Kimmerle, et al. (2004). 'Multilayered Wrinkle Textures from Strain' pp. 225–232.

D. P. Kingma & J. Ba (2014). 'Adam: A Method for Stochastic Optimization'. *CoRR* **abs/1412.6980**.

Y. Kozlov, et al. (2017). 'Enriching Facial Blendshape Rigs with Physical Simulation'. *Computer Graphics Forum (Proc. Eurographics)* **36**(2).

L. Ladický, et al. (2015). 'Data-driven Fluid Simulations Using Regression Forests'. *ACM Trans. Graph.* **34**(6):199:1–199:9.

D. Lee, et al. (2012). 'Modeling and Simulation of Skeletal Muscle for Computer Graphics: A Survey'. *Found. Trends. Comput. Graph. Vis.* **7**(4):229–276.

H. Lee, et al. (2011). 'Unsupervised learning of hierarchical representations with convolutional deep belief networks'. *Communications of the ACM* **54**(10):95–103.

S.-H. Lee, et al. (2009). 'Comprehensive Biomechanical Modeling and Simulation of the Upper Body'. *ACM Trans. Graph.* **28**(4):99:1–99:17.

E. Lejeune, et al. (2016). 'An algorithmic approach to multi-layer wrinkling'. *Extreme Mechanics Letters* **7**:10–17.

D. I. W. Levin, et al. (2011). 'Eulerian Solid Simulation with Contact'. In *ACM SIGGRAPH 2011 Papers*, SIGGRAPH '11, pp. 36:1–36:10, New York, NY, USA. ACM.

J. P. Lewis, et al. (2000). 'Pose Space Deformation: A Unified Approach to Shape Interpolation and Skeleton-driven Deformation'. In *Proceedings of the 27th Annual Conference on Computer Graphics and Interactive Techniques*, SIGGRAPH '00, pp. 165–172, New York, NY, USA. ACM Press/Addison-Wesley Publishing Co.

D. Li, et al. (2013). 'Thin Skin Elastodynamics'. *ACM Trans. Graph.* **32**(4):49:1–49:10.

P. Li & P. G. Kry (2014). 'Multi-layer Skin Simulation with Adaptive Constraints'. In *Proceedings of the Seventh International Conference on Motion in Games*, MIG '14, pp. 171–176, New York, NY, USA. ACM.

P. Liepa (2003). 'Filling Holes in Meshes'. In *Proceedings of the 2003 Eurographics/ACM SIGGRAPH Symposium on Geometry Processing*, SGP '03, pp. 200–205, Aire-la-Ville, Switzerland, Switzerland. Eurographics Association.

T. Liu, et al. (2013). 'Fast Simulation of Mass-spring Systems'. *ACM Trans. Graph.* **32**(6):214:1–214:7.

T. Liu, et al. (2017). 'Quasi-Newton Methods for Real-Time Simulation of Hyperelastic Materials'. *ACM Trans. Graph.* **36**(3):23:1–23:16.

M. Macklin, et al. (2016). 'XPBD: Position-based Simulation of Compliant Constrained Dynamics'. In *Proceedings of the 9th International Conference on Motion in Games*, MIG '16, pp. 49–54, New York, NY, USA. ACM.

N. Magnenat-Thalmann, et al. (1988). 'Joint-dependent Local Deformations for Hand Animation and Object Grasping'. In *Proceedings on Graphics Interface '88*, pp. 26–33, Toronto, Ont., Canada, Canada. Canadian Information Processing Society.

S. Martin, et al. (2011). 'Example-based Elastic Materials'. *ACM Trans. Graph.* **30**(4):72:1–72:8.

J. Masci, et al. (2015a). 'Geodesic convolutional neural networks on Riemannian manifolds'. In *Proc. of the IEEE International Conference on Computer Vision (ICCV) Workshops*, pp. 37–45.

J. Masci, et al. (2015b). 'ShapeNet: convolutional neural networks on non-Euclidean manifolds'. Tech. Rep. arXiv:1501.06297.

Massage Research (2013). 'Massage Research'. `http://true.massage-research.com/2013/06/fascia-and-reflexology.html`.

A. McAdams, et al. (2011). 'Efficient Elasticity for Character Skinning with Contact and Collisions'. *ACM Trans. Graph.* **30**(4):37:1–37:12.

J. McCormack & A. Sherstyuk (1998). 'Creating and rendering convolution surfaces'. In *Computer Graphics Forum*, vol. 17, pp. 113–120. Wiley Online Library.

A. Milne, et al. (2016). 'Flesh, Flab, and Fascia Simulation on Zootopia'.

In *ACM SIGGRAPH 2016 Talks*, SIGGRAPH '16, pp. 34:1–34:2, New York, NY, USA. ACM.

N. Mitchell, et al. (2015). 'GRIDiron: An Interactive Authoring and Cognitive Training Foundation for Reconstructive Plastic Surgery Procedures'. *ACM Trans. Graph.* **34**(4):43:1–43:12.

W. Mollemans, et al. (2003). 'Tetrahedral Mass Spring Model for Fast Soft Tissue Deformation'. In N. Ayache & H. Delingette (eds.), *Surgery Simulation and Soft Tissue Modeling*, vol. 2673 of *Lecture Notes in Computer Science*, pp. 145–154. Springer Berlin Heidelberg.

F. Monti, et al. (2016). 'Geometric deep learning on graphs and manifolds using mixture model CNNs (Tech Report)'. *CoRR* **abs/1611.08402**.

M. Müller & M. Gross (2004). 'Interactive Virtual Materials'. In *Proceedings of Graphics Interface 2004*, GI '04, pp. 239–246, School of Computer Science, University of Waterloo, Waterloo, Ontario, Canada. Canadian Human-Computer Communications Society.

M. Müller, et al. (2007). 'Position Based Dynamics'. *J. Vis. Comun. Image Represent.* **18**(2):109–118.

M. Müller, et al. (2005). 'Meshless Deformations Based on Shape Matching'. In *ACM SIGGRAPH 2005 Papers*, SIGGRAPH '05, pp. 471–478, New York, NY, USA. ACM.

Myers,T. (2013). 'Myers,T.'. `https://www.youtube.com/watch?v=xzX-PeU_MTo`.

Myotherapies (2013). 'Myotherapies'. `http://www.myotherapies.co.uk/about-mfr-therapy/what-is-fascia/`.

A. Nealen, et al. (2006). 'Physically Based Deformable Models in Computer Graphics' **25**:809–836.

T. Neumann, et al. (2013). 'Capture and Statistical Modeling of Arm-Muscle Deformations'. *Computer Graphics Forum* **32**(2pt3):285–294.

J. F. O'Brien (2002). 'Graphical Modeling and Animation of Ductile Fracture'. In *Proceedings of the 29th International Conference on*

Computer Graphics and Interactive Techniques. Electronic Art and Animation Catalog., SIGGRAPH '02, pp. 161–161, New York, NY, USA. ACM.

J. F. O'Brien & J. K. Hodgins (1999). 'Graphical Modeling and Animation of Brittle Fracture'. In *Proceedings of the 26th Annual Conference on Computer Graphics and Interactive Techniques*, SIGGRAPH '99, pp. 137–146, New York, NY, USA. ACM Press/Addison-Wesley Publishing Co.

M. A. Otaduy, et al. (2009). 'Implicit Contact Handling for Deformable Objects'. *Computer Graphics Forum (Proc. of Eurographics)* **28**(2).

E. C. Paes, et al. (2009). 'Perioral Wrinkles: Histologic Differences Between Men and Women'. *Aesthetic Surgery Journal* **29**(6):467–472.

D. K. Pai, et al. (2014). 'Eulerian Solids for Soft Tissue and More'. In *ACM SIGGRAPH 2014 Courses*, SIGGRAPH '14, pp. 22:1–22:151, New York, NY, USA. ACM.

E. G. Parker & J. F. O'Brien (2009). 'Real-time Deformation and Fracture in a Game Environment'. In *Proceedings of the 2009 ACM SIGGRAPH/Eurographics Symposium on Computer Animation*, SCA '09, pp. 165–175, New York, NY, USA. ACM.

T. Patterson, et al. (2012). 'Simulation of Complex Nonlinear Elastic Bodies Using Lattice Deformers'. *ACM Trans. Graph.* **31**(6):197:1–197:10.

S. Pirk, et al. (2017). 'Interactive Wood Combustion for Botanical Tree Models'. *ACM Trans. Graph.* **36**(6):197:1–197:12.

G. Pons-Moll, et al. (2015). 'Dyna: A Model of Dynamic Human Shape in Motion'. *ACM Trans. Graph.* **34**(4):120:1–120:14.

O. Rémillard & P. G. Kry (2013). 'Embedded Thin Shells for Wrinkle Simulation'. *ACM Trans. Graph.* **32**(4):50:1–50:8.

C. W. Reynolds (1987). 'Flocks, Herds and Schools: A Distributed Behavioral Model'. *SIGGRAPH Comput. Graph.* **21**(4):25–34.

D. Rohmer, et al. (2010). 'Animation Wrinkling: Augmenting Coarse Cloth Simulations with Realistic-looking Wrinkles'. *ACM Trans. Graph.* **29**(6):157:1–157:8.

P. Sachdeva, et al. (2015). 'Biomechanical Simulation and Control of Hands and Tendinous Systems'. *ACM Trans. Graph.* **34**(4):42:1–42:10.

J. Saito & S. Yuen (2017). 'Efficient and Robust Skin Slide Simulation'. In *Proceedings of the ACM SIGGRAPH Digital Production Symposium*, DigiPro '17, pp. 10:1–10:6, New York, NY, USA. ACM.

S. Saito, et al. (2015). 'Computational Bodybuilding: Anatomically-based Modeling of Human Bodies'. *ACM Trans. Graph.* **34**(4):41:1–41:12.

M. Sanchez, et al. (2012). 'Efficient Evaluation of Continuous Signed Distance to a Polygonal Mesh'. In *Proceedings of the 28th Spring Conference on Computer Graphics*, SCCG '12, pp. 101–108, New York, NY, USA. ACM.

C. Schumacher, et al. (2012). 'Efficient Simulation of Example-based Materials'. In *Proceedings of the ACM SIGGRAPH/Eurographics Symposium on Computer Animation*, SCA '12, pp. 1–8, Aire-la-Ville, Switzerland, Switzerland. Eurographics Association.

T. Sederberg & S. Parry (1986). 'Free-form deformation of solid geometric models' pp. 151–159.

W. Si, et al. (2014). 'Realistic Biomechanical Simulation and Control of Human Swimming'. *ACM Trans. Graph.* **34**(1):10:1–10:15.

Siegel, Jeffrey (2015). 'What makes muscles grow?'. `https://www.youtube.com/watch?v=2tM1LFFxeKg`.

E. Sifakis & J. Barbic (2012). 'FEM Simulation of 3D Deformable Solids: A Practitioner's Guide to Theory, Discretization and Model Reduction'. In *ACM SIGGRAPH 2012 Courses*, SIGGRAPH '12, pp. 20:1–20:50, New York, NY, USA. ACM.

E. Sifakis, et al. (2005). 'Automatic Determination of Facial Muscle Activations from Sparse Motion Capture Marker Data'. In *ACM SIG-*

GRAPH 2005 Papers, SIGGRAPH '05, pp. 417–425, New York, NY, USA. ACM.

F. Sin, et al. (2013a). 'Vega: Non-Linear FEM Deformable Object Simulator.'. *Comput. Graph. Forum* **32**(1):36–48.

F. Sin, et al. (2011). 'Invertible isotropic hyperelasticity using SVD gradients'. In *In ACM SIGGRAPH / Eurographics Symposium on Computer Animation (Posters)*.

F. S. Sin, et al. (2013b). 'Vega: Non-Linear FEM Deformable Object Simulator'. *Computer Graphics Forum* **32**(1):36–48.

M. Skouras, et al. (2012). 'Computational Design of Rubber Balloons'. *Comput. Graph. Forum* **31**(2):835–844.

M. Skouras, et al. (2014). 'Designing Inflatable Structures'. *ACM Trans. Graph.* **33**(4):63:1–63:10.

P.-P. J. Sloan, et al. (2001). 'Shape by Example'. In *Proceedings of the 2001 Symposium on Interactive 3D Graphics*, I3D '01, pp. 135–143, New York, NY, USA. ACM.

O. Sorkine, et al. (2004). 'Laplacian surface editing'. In *Proceedings of the 2004 Eurographics/ACM SIGGRAPH symposium on Geometry processing*, pp. 175–184. ACM.

N. Srivastava, et al. (2014). 'Dropout: A Simple Way to Prevent Neural Networks from Overfitting'. *Journal of Machine Learning Research* **15**:1929–1958.

L. Stecco (2012). *Fascial manipulation for muscoloskeletal pain.* Piccin-Nuova Libraria.

S. Sueda, et al. (2008). 'Musculotendon Simulation for Hand Animation'. *ACM Trans. Graph.* **27**(3):83:1–83:8.

R. W. Sumner & J. Popović (2004). 'Deformation transfer for triangle meshes'. In *ACM Transactions on Graphics (TOG)*, vol. 23, pp. 399–405. ACM.

Y. Talpaert (2010). *Tensor Analysis and Continuum Mechanics.* Springer Netherlands.

J. Tan, et al. (2012). 'Soft Body Locomotion'. *ACM Trans. Graph.* **31**(4):26:1–26:11.

J. Teran, et al. (2003). 'Finite Volume Methods for the Simulation of Skeletal Muscle'. In *Proceedings of the 2003 ACM SIGGRAPH/Eurographics Symposium on Computer Animation*, SCA '03, pp. 68–74, Aire-la-Ville, Switzerland, Switzerland. Eurographics Association.

J. Teran, et al. (2005a). 'Creating and Simulating Skeletal Muscle from the Visible Human Data Set'. *IEEE Transactions on Visualization and Computer Graphics* **11**(3):317–328.

J. Teran, et al. (2005b). 'Robust Quasistatic Finite Elements and Flesh Simulation'. In *Proceedings of the 2005 ACM SIGGRAPH/Eurographics Symposium on Computer Animation*, SCA '05, pp. 181–190, New York, NY, USA. ACM.

D. Terzopoulos & K. Fleischer (1988). 'Modeling Inelastic Deformation: Viscolelasticity, Plasticity, Fracture'. *SIGGRAPH Comput. Graph.* **22**(4):269–278.

D. Terzopoulos, et al. (1987). 'Elastically Deformable Models'. In *Proceedings of the 14th Annual Conference on Computer Graphics and Interactive Techniques*, SIGGRAPH '87, pp. 205–214, New York, NY, USA. ACM.

J. Tompson, et al. (2016). 'Accelerating Eulerian Fluid Simulation With Convolutional Networks'. *ArXiv e-prints* .

M. Tournier, et al. (2015). 'Stable Constrained Dynamics'. *ACM Trans. Graph.* **34**(4):132:1–132:10.

R. Vaillant, et al. (2013). 'Implicit Skinning: Real-time Skin Deformation with Contact Modeling'. *ACM Trans. Graph.* **32**(4):125:1–125:12.

R. Vaillant, et al. (2014). 'Robust Iso-surface Tracking for Interactive Character Skinning'. *ACM Trans. Graph.* **33**(6):189:1–189:11.

J. Vince (2006). *Barycentric Coordinates*, pp. 193–221. Springer London, London.

H. Wang, et al. (2011). 'Data-driven Elastic Models for Cloth: Modeling and Measurement'. *ACM Trans. Graph.* **30**(4):71:1–71:12.

M. Warburton (2014). 'Physically Based Forehead Modelling and Animation including Wrinkles'. *PhD thesis* .

WETA Digital (2013). 'Tissue system'. `http://www.fxguide.com/fxguidetv/fxguidetv-166-weta-digitals-tissue-system/`.

Z. Wu, et al. (2014). '3D ShapeNets for 2.5D Object Recognition and Next-Best-View Prediction'. *CoRR* **abs/1406.5670**.

H. Xu & J. Barbič (2017). 'Example-Based Damping Design'. *ACM Trans. on Graphics (SIGGRAPH 2017)* **36**(4).

H. Xu, et al. (2015a). 'Interactive Material Design using Model Reduction'. *ACM Trans. on Graphics* **34**(2).

H. Xu, et al. (2015b). 'Nonlinear Material Design Using Principal Stretches'. *ACM Trans. on Graphics (SIGGRAPH 2015)* **34**(4).

J. Yin, et al. (2010). 'Mechanical modeling of a wrinkled fingertip immersed in water'. *Acta biomaterialia* **6**(4):1487–1496.

F. Zajac (1989a). 'Muscle and tendon: properties, models, scaling, and application to biomechanics and motor control'. *Critical reviews in biomedical engineering* **17**(4):359411.

F. Zajac (1989b). 'Muscle and tendon: properties, models, scaling, and application to biomechanics and motor control'. *Critical reviews in biomedical engineering* **17**(4):359411.

Y. Zhao & J. Barbič (2013). 'Interactive Authoring of Simulation-Ready Plants'. *ACM Trans. on Graphics (SIGGRAPH 2013)* **32**(4):84:1–84:12.

L. Zhu, et al. (2015). 'Adaptable Anatomical Models for Realistic Bone Motion Reconstruction'. *Comput. Graph. Forum* **34**(2):459–471.

Zygote (2016). ‘Zygote’. https://www.zygote.com/.

Zygote Body (2016). ‘Zygote’. https://www.zygotebody.com/.

Appendix A

List of publications

Fabio Turchet, Oleg Fryazinov, Sara Schvartzman, 2017, Physically-based Muscles and Fibers modelling from Superficial Patches , Eurographics 2017 - Short Papers.DOI: http://dx.doi.org/10.2312/egsh.20171008

Fabio Turchet, Marco Romeo, and Oleg Fryazinov. 2016. Physics-aided editing of simulation-ready muscles for visual effects. In ACM SIGGRAPH 2016 Posters (SIGGRAPH '16). ACM, New York, NY, USA, , Article 80 , 2 pages. DOI: https://doi.org/10.1145/2945078.2945158

Fabio Turchet, Oleg Fryazinov, and Marco Romeo. 2015. Extending implicit skinning with wrinkles. In Proceedings of the 12th European Conference on Visual Media Production (CVMP '15). ACM, New York, NY, USA, Article 11, 6 pages.DOI: https://doi.org/10.1145/2824840.2824849

Fabio Turchet, Oleg Fryazinov, and Marco Romeo. 2015. Procedural wrinkles generation in the implicit skinning framework. In SIGGRAPH Asia 2015 Posters (SA '15). ACM, New York, NY, USA, , Article 16 , 1 pages. DOI: https://doi.org/10.1145/2820926.2820937

Appendix B

Material Derivation

B.1 Muscle material. Energy formula

We need to derivate this energy:

$$\Psi(I_1, I_2, \lambda, \mathbf{a_0}, \alpha) = F_1(I_1, I_2) + U(J) + F_2(\lambda, \alpha)$$

with respect to $\mathbf{F}$,

where $\mathbf{a_0}$ is a direction vector that doesn't depend on F and α is the muscle activation level,

$\lambda = \sqrt{\mathbf{a_0} \cdot \mathbf{C}\mathbf{a_0}}$,

$\mathbf{C} = \mathbf{J}^{-\frac{2}{3}}\mathbf{F}^{\mathbf{T}}\mathbf{F}$,

$I_1 = tr(\mathbf{C})$,

$I_2 = \frac{1}{2}((tr(\mathbf{C}))^2 - tr((\mathbf{C}^{\mathbf{2}})))$,

$\mathbf{J} = det(\mathbf{F})$.

Note: I assume vectors to be **column** vectors.

Because we are using the inverted elements framework (Irving 2004), $\mathbf{F}$ (the deformation gradient) should be $\hat{\mathbf{F}}$, that is its diagonalized version (via a modified SVD). Using $\hat{F}$ should also allow more simplifications. The result should be something similar to the terms in Teran 2003, page 5 bottom (stress formula).

Applying the chain rule as in the Sifakis notes and considering the λ variable as another variable to derive, we consider only the anisotropic part $F_2(\lambda, \alpha)$:

$$\frac{\partial F_2(\lambda, \alpha)}{\partial F} = \frac{\partial F_2(\lambda, \alpha)}{\partial \lambda} \frac{\partial \lambda}{\partial F} \tag{B.1}$$

developing only the rightmost term for now:

$$\frac{\partial \lambda}{\partial F} = \frac{\partial \sqrt{\mathbf{a_0 \cdot C a_0}}}{\partial F} = \frac{\partial \sqrt{\mathbf{a_0 \cdot J^{\frac{-2}{3}} F^T F a_0}}}{\partial F} = \tag{B.2}$$

applying chain rule because composition of functions and the derivative of the dot product

$$= \frac{1}{2}(a_0 \cdot J^{\frac{-2}{3}} F^T F a_0)^{\frac{-1}{2}} [a_0 \cdot (\frac{\partial (det(F)^{\frac{-2}{3}} F^T F a_0)}{\partial F}) + 0] = \tag{B.3}$$

Passing everything to components representation:

$$= \frac{1}{2}(a_0 \cdot J^{\frac{-2}{3}} F^T F a_0)_{lm}^{\frac{-1}{2}} (a_0 \cdot (\frac{\partial (det(F)^{\frac{-2}{3}} F^T F a_0)}{\partial F_{ij}}))_{lm} = \tag{B.4}$$

$$= \frac{1}{2}(a_l (J^{\frac{-2}{3}} F^T F a_0)_m)^{\frac{-1}{2}} (a_l (\frac{\partial (det(F)^{\frac{-2}{3}} F^T F a_0)}{\partial F_{ij}})_m) = \tag{B.5}$$

$$= \frac{1}{2}((a_l J^{\frac{-2}{3}} F^T F)_{lm} a_m)^{\frac{-1}{2}} (a_l (\frac{\partial (det(F)^{\frac{-2}{3}} F^T F)}{\partial F_{ij}})_{lm} a_m) = \tag{B.6}$$

$$= \frac{1}{2}((J^{\frac{-2}{3}} F^T F)_{lm} a_l a_m)^{\frac{-1}{2}} ((\frac{\partial (det(F)^{\frac{-2}{3}} F^T F)}{\partial F_{ij}})_{lm} a_l a_m) = \tag{B.7}$$

$$= \frac{1}{2\lambda}((\frac{\partial (det(F)^{\frac{-2}{3}} F^T F)}{\partial F_{ij}})_{lm}) a_l a_m = \tag{B.8}$$

$$= \frac{1}{2\lambda}[(\frac{\partial (det(F)^{\frac{-2}{3}})}{\partial F_{ij}} (F^T F)_{lm} + det(F)^{\frac{-2}{3}} \frac{\partial (F^T F)_{lm}}{\partial F_{ij}}] a_l a_m = \tag{B.9}$$

$$= \frac{1}{2\lambda}[\frac{-2}{3} det(F)^{\frac{-5}{3}} (\frac{\partial (det(F))}{\partial F_{ij}} (F^T F)_{lm} + det(F)^{\frac{-2}{3}} (F_{il}\delta_{mj} + F_{im}\delta_{lj})] a_l a_m = \tag{B.10}$$

Now using the known equality $\frac{\partial det(A)}{\partial A} = det(A)[A^{-1}]^T$:

$$= \frac{1}{2\lambda}[\frac{-2}{3} det(F)^{\frac{-5}{3}} det(F)(F^{-T})_{ij} (F^T F)_{lm} + det(F)^{\frac{-2}{3}} F_{il}\delta_{mj} + det(F)^{\frac{-2}{3}} F_{im}\delta_{lj})] a_l a_m = \tag{B.11}$$

$$= \frac{1}{2\lambda}[\frac{-2}{3} det(F)^{\frac{-2}{3}} (F^{-T})_{ij} F_{kl} F_{km} + det(F)^{\frac{-2}{3}} F_{il}\delta_{mj} + det(F)^{\frac{-2}{3}} F_{im}\delta_{lj})] a_l a_m = \tag{B.12}$$

$$= \frac{1}{2\lambda}[\frac{-2}{3} det(F)^{\frac{-2}{3}} (F^{-T})_{ij} F_{kl} F_{km} a_l a_m + det(F)^{\frac{-2}{3}} F_{il} a_l a_j + det(F)^{\frac{-2}{3}} F_{im} a_j a_m)] = \tag{B.13}$$

$$= \frac{1}{2\lambda}[\frac{-2}{3}det(F)^{\frac{-2}{3}}(F^{-T})_{ij}F_{kl}F_{km}a_l a_m + det(F)^{\frac{-2}{3}}(Fa)_i a_j + det(F)^{\frac{-2}{3}}(Fa)_i a_j)] = \tag{B.14}$$

$$= \frac{1}{2\lambda}[\frac{-2}{3}det(F)^{\frac{-2}{3}}(F^{-T})_{ij}(Fa)_k(Fa)_k + det(F)^{\frac{-2}{3}}(Fa)_i a_j + det(F)^{\frac{-2}{3}}(Fa)_i a_j)] = \tag{B.15}$$

$$= \frac{1}{2\lambda}[\frac{-2}{3}det(F)^{\frac{-2}{3}}(F^{-T})_{ij}(Fa)_k(Fa)_k + 2det(F)^{\frac{-2}{3}}(Fa)_i a_j)] = \tag{B.16}$$

Now passing back to no-components representation:

$$= \frac{1}{2\lambda}[\frac{-2}{3}det(F)^{\frac{-2}{3}}(F^{-T})tr((Fa)(Fa)^T) + 2det(F)^{\frac{-2}{3}}F(aa^T)] = \tag{B.17}$$

$$= \frac{J^{\frac{-2}{3}}}{2\lambda}[\frac{-2}{3}(F^{-T})tr((Fa)(Fa)^T) + 2F(aa^T)] \tag{B.18}$$

$$= \frac{J^{\frac{-2}{3}}}{\lambda}[\frac{-1}{3}(F^{-T})tr((Fa)(Fa)^T) + F(aa^T)] \tag{B.19}$$

which is a matrix (one part of the stress P)

Now, let's derive the first term.
Note that $F_2(\lambda, \alpha) = \alpha F_{active}(\lambda) + F_{passive}(\lambda)$ and are defined piecewise in Blemker 2005 paper (see table below and refer to paper for parameter values). So it's enough to take simple derivatives of the formulas in the table.

Now in order to use the paper Irving 2004 for invertible elements, let's use the diagonalized version of F that is $F = \hat{F}$ which implies that $\hat{F}^T = \hat{F}$

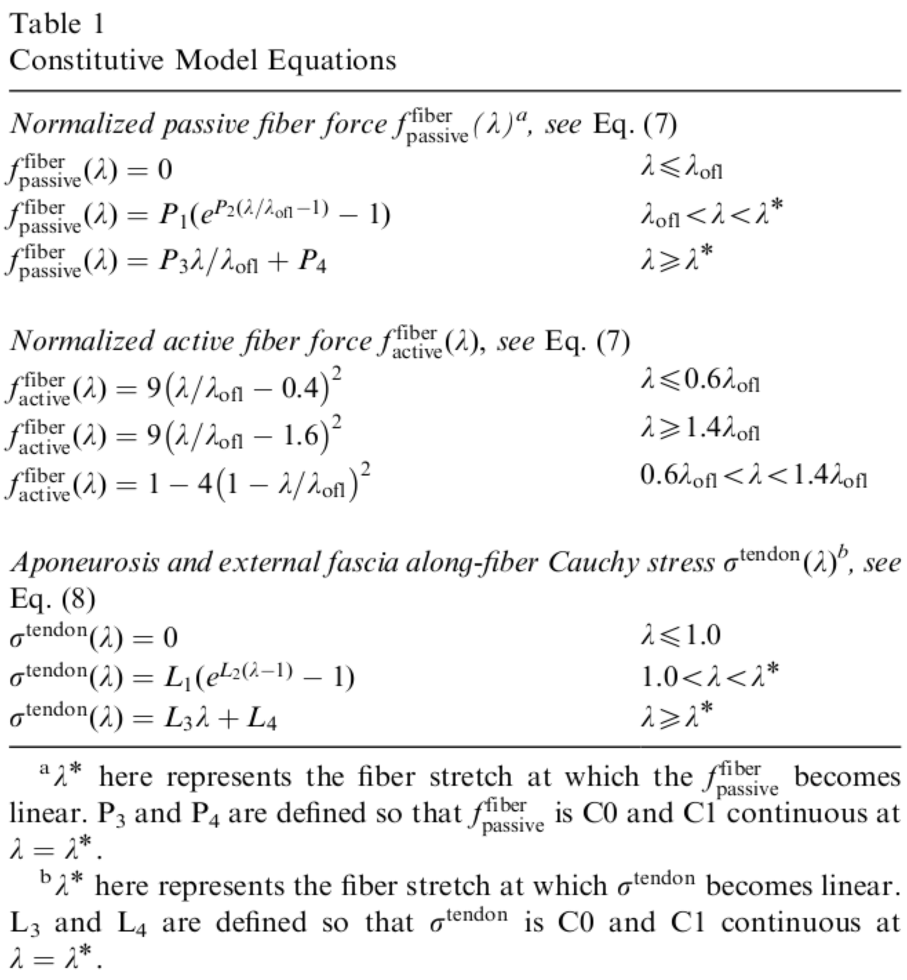

Table 1
Constitutive Model Equations

Normalized passive fiber force $f^{\text{fiber}}_{\text{passive}}(\lambda)^{a}$, *see* Eq. (7)	
$f^{\text{fiber}}_{\text{passive}}(\lambda) = 0$	$\lambda \leqslant \lambda_{\text{ofl}}$
$f^{\text{fiber}}_{\text{passive}}(\lambda) = P_1(e^{P_2(\lambda/\lambda_{\text{ofl}}-1)} - 1)$	$\lambda_{\text{ofl}} < \lambda < \lambda^*$
$f^{\text{fiber}}_{\text{passive}}(\lambda) = P_3\lambda/\lambda_{\text{ofl}} + P_4$	$\lambda \geqslant \lambda^*$
Normalized active fiber force $f^{\text{fiber}}_{\text{active}}(\lambda)$, *see* Eq. (7)	
$f^{\text{fiber}}_{\text{active}}(\lambda) = 9(\lambda/\lambda_{\text{ofl}} - 0.4)^2$	$\lambda \leqslant 0.6\lambda_{\text{ofl}}$
$f^{\text{fiber}}_{\text{active}}(\lambda) = 9(\lambda/\lambda_{\text{ofl}} - 1.6)^2$	$\lambda \geqslant 1.4\lambda_{\text{ofl}}$
$f^{\text{fiber}}_{\text{active}}(\lambda) = 1 - 4(1 - \lambda/\lambda_{\text{ofl}})^2$	$0.6\lambda_{\text{ofl}} < \lambda < 1.4\lambda_{\text{ofl}}$
Aponeurosis and external fascia along-fiber Cauchy stress $\sigma^{\text{tendon}}(\lambda)^{b}$, *see* Eq. (8)	
$\sigma^{\text{tendon}}(\lambda) = 0$	$\lambda \leqslant 1.0$
$\sigma^{\text{tendon}}(\lambda) = L_1(e^{L_2(\lambda-1)} - 1)$	$1.0 < \lambda < \lambda^*$
$\sigma^{\text{tendon}}(\lambda) = L_3\lambda + L_4$	$\lambda \geqslant \lambda^*$

[a] λ^* here represents the fiber stretch at which the $f^{\text{fiber}}_{\text{passive}}$ becomes linear. P_3 and P_4 are defined so that $f^{\text{fiber}}_{\text{passive}}$ is C0 and C1 continuous at $\lambda = \lambda^*$.

[b] λ^* here represents the fiber stretch at which σ^{tendon} becomes linear. L_3 and L_4 are defined so that σ^{tendon} is C0 and C1 continuous at $\lambda = \lambda^*$.

Figure B.1: *Formulas reproduced from Blemker 2005 paper.*

Given the diagonalization $F = U\hat{F}V^T$, we set $a_0 = V^T a_0$ as described in Irving 2004 paper (section 6.1) to rotate the anisotropic terms using V.

$$\frac{\partial F_2(\lambda,\alpha)}{\partial\lambda}\left(\frac{1}{2\lambda}V^T a_0 \cdot 2[(-\frac{1}{3}J^2\hat{F} + J^{-\frac{2}{3}}\hat{F}Ones]V^T a_0\right)$$

with $\lambda = \sqrt{\mathbf{V^T a_0 \cdot J^{\frac{-2}{3}}\hat{F}^2 V^T a_0}}$, $J = det(\hat{F})$ and $Ones$ a matrix with only 1's.

Another term of the energy as defined in Teran 2003 paper is

$$U(J) = K\ln(J)^2$$

$$\frac{\partial U(J)}{\partial F} = \frac{\partial U(J)}{\partial J}\frac{\partial J}{\partial F} = \frac{2K\ln(J)}{J}det(F)F^{-T} = 2K\ln(J)F^{-T}$$

then using $\hat{F}$:

$$= 2K\ln(det(\hat{F}))\hat{F}^{-1}$$

regarding the $F1$ term of the energy, in Teran 2003 is an incompressible Mooney-Rivlin like material:

$$F_1(I_1, I_2) = AI_1 + BI_2$$

but in this work a StVk isotropic material is used, as already implemented in VEGA.

Second derivative

Deriving a second time the result of $\frac{\partial F_2(\lambda,\alpha)}{\partial F}$ using the same rules, the 4th order tensor is obtained:

$$
\begin{aligned}
&\frac{\partial^2 F_2(\lambda,\alpha)}{\partial F^2} = \\
&= -\frac{2}{9} J^{\frac{-2}{3}} (F^{-T})_{ij} (a_0 \cdot J^{\frac{-2}{3}} F^T F a_0)_{lm}^{\frac{-1}{2}} (F^{-T})_{ij} (Fa)_k (Fa)_k \\
&- \frac{2}{3} J^{\frac{-2}{3}} (F^{-T})_{ij} (a_0 \cdot J^{\frac{-2}{3}} F^T F a_0)_{lm}^{\frac{-1}{2}} (Fa)_i a_j
\end{aligned}
$$

Appendix C

Material Derivation (cont.)

C.1 Derivation of dPdF for StVk material

Derivation of the Piola stress for StVk stress P(F):

$$\mathbf{P}(\mathbf{F}) = \mathbf{F}[2\mu\mathbf{E} + \lambda tr(\mathbf{E})\mathbf{I}] \tag{C.1}$$

Some known identities used:

$$\frac{\partial \mathbf{F}_{ij}}{\partial \mathbf{F}_{pq}} = \delta_{ip}\delta_{jq}$$

where δ_{mn} is the Dirac's delta that evaluates to 1 IFF $m = n$, 0 otherwise.

Trace in index notation:

$$tr(\mathbf{F^T F}) = tr((\mathbf{F^T F})_{\mathbf{lm}}) = tr(\mathbf{F^T}_{lk}\mathbf{F}_{km}) = \mathbf{F^T}_{lk}\mathbf{F}_{kl} = \mathbf{F}_{kl}\mathbf{F}_{kl}$$

Derivative of the trace:

$$\frac{\partial tr(\mathbf{F^T F})}{\partial \mathbf{F}} = \frac{\partial \mathbf{F}_{kl}\mathbf{F}_{kl}}{\partial \mathbf{F}_{pq}} = \frac{\partial \mathbf{F}_{kl}}{\partial \mathbf{F}_{pq}}\mathbf{F}_{kl} + \frac{\partial \mathbf{F}_{kl}}{\partial \mathbf{F}_{pq}}\mathbf{F}_{kl} = 2\delta_{kp}\delta_{lq}\mathbf{F}_{kl} = 2\mathbf{F}_{pq}$$

Which is correct considering that in Sifakis notes it results $2F$.

Derivative of FTF

$$\frac{\partial(\mathbf{F^T F})}{\partial \mathbf{F}} = \frac{\partial(\mathbf{F^T F})_{lm}}{\partial \mathbf{F}_{pq}} = \frac{\partial(\mathbf{F^T}_{lk}\mathbf{F}_{km})}{\partial \mathbf{F}_{pq}} = \frac{\partial(\mathbf{F^T}_{lk})}{\partial \mathbf{F}_{pq}}\mathbf{F}_{km} + \frac{\partial(\mathbf{F}_{km})}{\partial \mathbf{F}_{pq}}\mathbf{F^T}_{lk} =$$

$$= \delta_{kp}\delta lq\mathbf{F}_{km} + \delta_{kp}\delta mq\mathbf{F}_{kl} = \delta lq\mathbf{F}_{pm} + \delta mq\mathbf{F}_{pl}$$

Full derivation :

$$\frac{\partial \mathbf{P}(\mathbf{F})}{\partial \mathbf{F}} = \frac{\partial(\mathbf{F}[2\mu\mathbf{E} + \lambda tr(\mathbf{E})\mathbf{I}])}{\partial \mathbf{F}} = \tag{C.2}$$

$$\frac{\partial(2\mu\mathbf{FE} + \lambda tr(\mathbf{E})\mathbf{F})}{\partial \mathbf{F}} = \tag{C.3}$$

$$\frac{\partial(2\mu\mathbf{F}\frac{1}{2}(\mathbf{F^T F} - \mathbf{I}) + \lambda\frac{1}{2}tr(\mathbf{F^T F} - \mathbf{I})\mathbf{F})}{\partial \mathbf{F}} = \tag{C.4}$$

$$\frac{\partial(\mu\mathbf{F}(\mathbf{F^T F} - \mathbf{I}) + \lambda\frac{1}{2}tr(\mathbf{F^T F} - \mathbf{I})\mathbf{F})}{\partial \mathbf{F}} = \tag{C.5}$$

$$\mu\frac{\partial(\mathbf{F}(\mathbf{F^T F} - \mathbf{I}))}{\partial \mathbf{F}} + \frac{1}{2}\lambda\frac{\partial(tr(\mathbf{F^T F} - \mathbf{I})\mathbf{F})}{\partial \mathbf{F}} = \tag{C.6}$$

At this point let's call **A** the first term and **B** the second and solve them separately.

A:

$$\mu\frac{\partial(\mathbf{F}(\mathbf{F^T F} - \mathbf{I}))}{\partial \mathbf{F}} = \tag{C.7}$$

$$\mu\frac{\partial(\mathbf{FF^T F} - \mathbf{F})}{\partial \mathbf{F}} = \tag{C.8}$$

Now passing to component notation, using Einstein summation convention

$$\mu\frac{\partial((\mathbf{F}\mathbf{F}^{\mathbf{T}}\mathbf{F})_{ij}-\mathbf{F}_{ij})}{\partial\mathbf{F}_{pq}}= \tag{C.9}$$

$$\mu\frac{\partial(\mathbf{F}_{il}(\mathbf{F}^{\mathbf{T}}\mathbf{F})_{lj}-\mathbf{F}_{ij})}{\partial\mathbf{F}_{pq}}= \tag{C.10}$$

$$\mu\frac{\partial\mathbf{F}_{il}(\mathbf{F}^{\mathbf{T}}\mathbf{F})_{lj}}{\partial\mathbf{F}_{pq}}-\frac{\partial\mathbf{F}_{ij}}{\partial\mathbf{F}_{pq}}= \tag{C.11}$$

Now applying the product rule to the first term:

$$\mu\frac{\partial\mathbf{F}_{il}}{\partial\mathbf{F}_{pq}}(\mathbf{F}^{\mathbf{T}}\mathbf{F})_{lj}+\frac{\partial\mathbf{F}^{\mathbf{T}}\mathbf{F})_{lj}}{\partial\mathbf{F}_{pq}}\mathbf{F}_{il}-\frac{\partial\mathbf{F}_{ij}}{\partial\mathbf{F}_{pq}}= \tag{C.12}$$

$$\mu(\delta_{ip}\delta_{lq}\mathbf{F}^{\mathbf{T}}\mathbf{F})_{lj}+(\mathbf{F}_{pl}\delta_{jq}+\mathbf{F}_{pj}\delta_{lq})\mathbf{F}_{il}-\delta_{ip}\delta_{jq}) \tag{C.13}$$

$$\mu(\delta_{ip}\mathbf{F}^{\mathbf{T}}\mathbf{F})_{qj}+(\mathbf{F}_{pl}\delta_{jq}\mathbf{F}_{il}+\mathbf{F}_{pj}\delta_{lq}\mathbf{F}_{il})-\delta_{ip}\delta_{jq}) \tag{C.14}$$

$$\mu(\delta_{ip}\mathbf{F}^{\mathbf{T}}\mathbf{F})_{qj}+(\mathbf{F}_{pl}\mathbf{F}^{\mathbf{T}}{}_{li}\delta_{jq}+\mathbf{F}^{\mathbf{T}}{}_{li}\mathbf{F}_{pj}\delta_{lq})-\delta_{ip}\delta_{jq}) \tag{C.15}$$

$$\mu(\delta_{ip}\mathbf{F}^{\mathbf{T}}\mathbf{F})_{qj}+(\mathbf{F}^{\mathbf{T}}\mathbf{F})_{pi}\delta_{jq}+\mathbf{F}^{\mathbf{T}}{}_{qi}\mathbf{F}_{pj}-\delta_{ip}\delta_{jq}) \tag{C.16}$$

which is a 4th order tensor with indices (i,j,p,q). Now for the $\mathbf{B}$ term.

B:

$$\frac{1}{2}\lambda\frac{\partial(tr(\mathbf{F}^{\mathbf{T}}\mathbf{F}-\mathbf{I})\mathbf{F})}{\partial\mathbf{F}}= \tag{C.17}$$

$$\frac{1}{2}\lambda\frac{\partial((tr(\mathbf{F}^{\mathbf{T}}\mathbf{F})-tr(\mathbf{I}))\mathbf{F})}{\partial\mathbf{F}}= \tag{C.18}$$

$$\frac{1}{2}\lambda(\frac{\partial tr(\mathbf{F^T F})\mathbf{F}}{\partial \mathbf{F}} - \frac{\partial tr(\mathbf{I})\mathbf{F}}{\partial \mathbf{F}}) = \tag{C.19}$$

Apply product rule on first term

$$\frac{1}{2}\lambda(\frac{\partial tr(\mathbf{F^T F})}{\partial \mathbf{F}}\mathbf{F} + \frac{\partial \mathbf{F}}{\partial \mathbf{F}} tr(\mathbf{F^T F}) - \frac{\partial \mathbf{3F}}{\partial \mathbf{F}}) = \tag{C.20}$$

Passing to component notation

$$\frac{1}{2}\lambda(\frac{\partial tr(\mathbf{F^T F})}{\partial \mathbf{F}_{pq}}\mathbf{F}_{ij} + \frac{\partial \mathbf{F}_{ij}}{\partial \mathbf{F}_{pq}} tr(\mathbf{F^T F}) - 3\frac{\partial \mathbf{F}_{ij}}{\partial \mathbf{F}_{pq}}) = \tag{C.21}$$

$$\frac{1}{2}\lambda(2\mathbf{F}_{pq}\mathbf{F}_{ij} + \delta_{ip}\delta_{jq} tr(\mathbf{F^T F}) - 3\delta_{ip}\delta_{jq}) \tag{C.22}$$

which is again a 4th order tensor with indices (i, j, p, q).

Appendix D

EngD Experience Conclusions

As a general conclusion, overall the experience of doing an engineering doctorate (EngD) was extremely valuable, mostly for the fact of being immersed in a production environment which was the right ecosystem to develop research ideas that could have a real life impact. Below are summarized some of the lessons learned in my journey, together with recommendations for future students who intend to take the research path of an EngD.

Unless strictly necessary, it is advisable to not start coding from scratch neither basic nor complex libraries that have already an efficient open source implementation, especially for research papers: an EngD is not a programming exercise. The reason is that writing really efficient APIs not only requires extremely solid software engineering expertise, but also takes significant time which would be subtracted from the real occupation of any researcher: doing research. Luckily there are numerous open source projects in the computer graphics community which are freely available under different kinds of licenses.

At the same time though, it is of capital importance to start implementing prototypes as soon as possible and win the temptation of first reading and studying every single paper on the topic. A good initial literature review is essential to put order and hierarchy of importance in the vast amount of knowledge available on a research topic, but thinking that a good innovative idea will come only after an exhaustive analysis of all the papers is just an illusion. The most productive and original ideas come generally either after long term focus on a very narrow area or through the influence of research developed in other fields, often totally different from computer graphics (i.e. biology, chemistry, artificial intelligence).

When doing Research and Development (RnD) it is easy to isolate oneself from the rest of the team because complex problems require persistent mental effort spread often across several months. It is fundamental though to keep maintaining the feedback loop between supervisors and especially people involved in production bouncing off ideas regularly. This can be obtained through daily or weekly *scrums* and regular video calls. It is common to arrive at dead ends in research: it was often the case in my experience to get new fresh perspectives and valuable suggestions from people working in other departments of the company, not biased about the problem I was trying to solve.

When choosing a research project and during the inevitable iterations and adjustments that will follow, it is important to always try and see the implications of the work on the long term in the future and its place in the global pipeline. The output of the character deformation stage for example affects deeply the grooming department stage so keeping the big picture in mind helped taking some technical decisions over others. For this reason I recommend creating flexible plans and revise them with supervisors regularly, making sure that every week brings some form of progress towards either a new goal or the resolution of existing problems. In general, the persistent awareness that it is necessary to fail early and often while being at the same time "micro-ambitious", constituted the main mindset I adopted in the many and inevitable periods of setbacks.